

EUROPEAN ORGANIZATION FOR NUCLEAR RESEARCH

CERN-EP/2003-053
25th August 2003

Tests of the Standard Model and Constraints on New Physics from Measurements of Fermion-Pair Production at 189–209 GeV at LEP

The OPAL Collaboration

Abstract

Cross-sections and angular distributions for hadronic and lepton-pair final states in e^+e^- collisions at centre-of-mass energies between 189 GeV and 209 GeV, measured with the OPAL detector at LEP, are presented and compared with the predictions of the Standard Model. The measurements are used to determine the electromagnetic coupling constant α_{em} at LEP 2 energies. In addition, the results are used together with OPAL measurements at 91–183 GeV within the S-matrix formalism to determine the γ -Z interference term and to make an almost model-independent measurement of the Z mass. Limits on extensions to the Standard Model described by effective four-fermion contact interactions or the addition of a heavy Z' boson are also presented.

Submitted to European Journal of Physics C

The OPAL Collaboration

G. Abbiendi², C. Ainsley⁵, P.F. Åkesson^{3,y}, G. Alexander²², J. Allison¹⁶, P. Amaral⁹,
G. Anagnostou¹, K.J. Anderson⁹, S. Arcelli², S. Asai²³, D. Axen²⁷, G. Azuelos^{18,a}, I. Bailey²⁶,
E. Barberio^{8,p}, T. Barillari³², R.J. Barlow¹⁶, R.J. Batley⁵, P. Bechtle²⁵, T. Behnke²⁵,
K.W. Bell²⁰, P.J. Bell¹, G. Bella²², A. Bellerive⁶, G. Benelli⁴, S. Bethke³², O. Biebel³¹,
O. Boeriu¹⁰, P. Bock¹¹, M. Boutemeur³¹, S. Braibant⁸, L. Brigliadori², R.M. Brown²⁰,
K. Buesser²⁵, H.J. Burckhart⁸, S. Campana⁴, R.K. Carnegie⁶, B. Caron²⁸, A.A. Carter¹³,
J.R. Carter⁵, C.Y. Chang¹⁷, D.G. Charlton¹, C. Ciocca², A. Csilling²⁹, M. Cuffiani², S. Dado²¹,
A. De Roeck⁸, E.A. De Wolf^{8,s}, K. Desch²⁵, B. Dienes³⁰, M. Donkers⁶, J. Dubbert³¹,
E. Duchovni²⁴, G. Duckeck³¹, I.P. Duerdorff¹⁶, E. Etzion²², F. Fabbri², L. Feld¹⁰, P. Ferrari⁸,
F. Fiedler³¹, I. Fleck¹⁰, M. Ford⁵, A. Frey⁸, A. Fürtjes⁸, P. Gagnon¹², J.W. Gary⁴, G. Gaycken²⁵,
C. Geich-Gimbel³, G. Giacomelli², P. Giacomelli², M. Giunta⁴, J. Goldberg²¹, E. Gross²⁴,
J. Grunhaus²², M. Gruwe⁸, P.O. Günther³, A. Gupta⁹, C. Hajdu²⁹, M. Hamann²⁵,
G.G. Hanson⁴, A. Harel²¹, M. Hauschild⁸, C.M. Hawkes¹, R. Hawkings⁸, R.J. Hemingway⁶,
C. Hensel²⁵, G. Herten¹⁰, R.D. Heuer²⁵, J.C. Hill⁵, K. Hoffman⁹, D. Horváth^{29,c},
P. Igo-Kemenes¹¹, K. Ishii²³, H. Jeremie¹⁸, P. Jovanovic¹, T.R. Junk⁶, N. Kanaya²⁶,
J. Kanzaki^{23,u}, D. Karlen²⁶, K. Kawagoe²³, T. Kawamoto²³, R.K. Keeler²⁶, R.G. Kellogg¹⁷,
B.W. Kennedy²⁰, K. Klein^{11,t}, A. Klier²⁴, S. Kluth³², T. Kobayashi²³, M. Kobel³,
S. Komamiya²³, L. Kormos²⁶, T. Krämer²⁵, P. Krieger^{6,l}, J. von Krogh¹¹, K. Kruger⁸, T. Kuhl²⁵,
M. Kupper²⁴, G.D. Lafferty¹⁶, H. Landsman²¹, D. Lanske¹⁴, J.G. Layter⁴, D. Lellouch²⁴,
J. Letts^o, L. Levinson²⁴, J. Lillich¹⁰, S.L. Lloyd¹³, F.K. Loebinger¹⁶, J. Lu^{27,w}, A. Ludwig³,
J. Ludwig¹⁰, A. Macpherson^{28,i}, W. Mader³, S. Marcellini², A.J. Martin¹³, G. Masetti²,
T. Mashimo²³, P. Mättig^m, W.J. McDonald²⁸, J. McKenna²⁷, T.J. McMahon¹,
R.A. McPherson²⁶, F. Meijers⁸, W. Menges²⁵, F.S. Merritt⁹, H. Mes^{6,a}, A. Michelini²,
S. Mihara²³, G. Mikenberg²⁴, D.J. Miller¹⁵, S. Moed²¹, W. Mohr¹⁰, T. Mori²³, A. Mutter¹⁰,
K. Nagai¹³, I. Nakamura^{23,v}, H. Nanjo²³, H.A. Neal³³, R. Nisius³², S.W. O'Neale¹, A. Oh⁸,
A. Okpara¹¹, M.J. Oreglia⁹, S. Orito^{23,*}, C. Pahl³², G. Pásztor^{4,g}, J.R. Pater¹⁶, J.E. Pilcher⁹,
J. Pinfold²⁸, D.E. Plane⁸, B. Poli², J. Polok⁸, O. Pooth¹⁴, M. Przybycien^{8,n}, A. Quadrat³,
K. Rabbertz^{8,r}, C. Rembser⁸, P. Renkel²⁴, J.M. Roney²⁶, S. Rosati^{3,y}, Y. Rozen²¹, K. Runge¹⁰,
K. Sachs⁶, T. Saeki²³, E.K.G. Sarkisyan^{8,j}, A.D. Schaile³¹, O. Schaile³¹, P. Scharff-Hansen⁸,
J. Schieck³², T. Schörner-Sadenius⁸, M. Schröder⁸, M. Schumacher³, C. Schwick⁸, W.G. Scott²⁰,
R. Seuster^{14,f}, T.G. Shears^{8,h}, B.C. Shen⁴, P. Sherwood¹⁵, A. Skuja¹⁷, A.M. Smith⁸, R. Sobie²⁶,
S. Söldner-Rembold^{16,d}, F. Spano⁹, A. Stahl^{3,x}, K. Stephens¹⁶, D. Strom¹⁹, R. Ströhmer³¹,
S. Tarem²¹, M. Tasevsky^{8,z}, R. Teuscher⁹, M.A. Thomson⁵, E. Torrence¹⁹, D. Toya²³, P. Tran⁴,
I. Trigger⁸, Z. Trócsányi^{30,e}, E. Tsur²², M.F. Turner-Watson¹, I. Ueda²³, B. Ujvári^{30,e},
C.F. Vollmer³¹, P. Vannerem¹⁰, R. Vértesi^{30,e}, M. Verzocchi¹⁷, H. Voss^{8,q}, J. Vossebeld^{8,h},
D. Waller⁶, C.P. Ward⁵, D.R. Ward⁵, P.M. Watkins¹, A.T. Watson¹, N.K. Watson¹, P.S. Wells⁸,
T. Wengler⁸, N. Wermes³, D. Wetterling¹¹, G.W. Wilson^{16,k}, J.A. Wilson¹, G. Wolf²⁴,
T.R. Wyatt¹⁶, S. Yamashita²³, D. Zer-Zion⁴, L. Zivkovic²⁴

¹School of Physics and Astronomy, University of Birmingham, Birmingham B15 2TT, UK

²Dipartimento di Fisica dell' Università di Bologna and INFN, I-40126 Bologna, Italy

³Physikalisches Institut, Universität Bonn, D-53115 Bonn, Germany

⁴Department of Physics, University of California, Riverside CA 92521, USA

⁵Cavendish Laboratory, Cambridge CB3 0HE, UK

⁶Ottawa-Carleton Institute for Physics, Department of Physics, Carleton University, Ottawa, Ontario K1S 5B6, Canada

⁸CERN, European Organisation for Nuclear Research, CH-1211 Geneva 23, Switzerland

⁹Enrico Fermi Institute and Department of Physics, University of Chicago, Chicago IL 60637, USA

¹⁰Fakultät für Physik, Albert-Ludwigs-Universität Freiburg, D-79104 Freiburg, Germany

¹¹Physikalisches Institut, Universität Heidelberg, D-69120 Heidelberg, Germany

¹²Indiana University, Department of Physics, Bloomington IN 47405, USA

¹³Queen Mary and Westfield College, University of London, London E1 4NS, UK

¹⁴Technische Hochschule Aachen, III Physikalisches Institut, Sommerfeldstrasse 26-28, D-52056 Aachen, Germany

¹⁵University College London, London WC1E 6BT, UK

¹⁶Department of Physics, Schuster Laboratory, The University, Manchester M13 9PL, UK

¹⁷Department of Physics, University of Maryland, College Park, MD 20742, USA

¹⁸Laboratoire de Physique Nucléaire, Université de Montréal, Montréal, Québec H3C 3J7, Canada

¹⁹University of Oregon, Department of Physics, Eugene OR 97403, USA

²⁰CCLRC Rutherford Appleton Laboratory, Chilton, Didcot, Oxfordshire OX11 0QX, UK

²¹Department of Physics, Technion-Israel Institute of Technology, Haifa 32000, Israel

²²Department of Physics and Astronomy, Tel Aviv University, Tel Aviv 69978, Israel

²³International Centre for Elementary Particle Physics and Department of Physics, University of Tokyo, Tokyo 113-0033, and Kobe University, Kobe 657-8501, Japan

²⁴Particle Physics Department, Weizmann Institute of Science, Rehovot 76100, Israel

²⁵Universität Hamburg/DESY, Institut für Experimentalphysik, Notkestrasse 85, D-22607 Hamburg, Germany

²⁶University of Victoria, Department of Physics, P O Box 3055, Victoria BC V8W 3P6, Canada

²⁷University of British Columbia, Department of Physics, Vancouver BC V6T 1Z1, Canada

²⁸University of Alberta, Department of Physics, Edmonton AB T6G 2J1, Canada

²⁹Research Institute for Particle and Nuclear Physics, H-1525 Budapest, P O Box 49, Hungary

³⁰Institute of Nuclear Research, H-4001 Debrecen, P O Box 51, Hungary

³¹Ludwig-Maximilians-Universität München, Sektion Physik, Am Coulombwall 1, D-85748 Garching, Germany

³²Max-Planck-Institute für Physik, Föhringer Ring 6, D-80805 München, Germany

³³Yale University, Department of Physics, New Haven, CT 06520, USA

^a and at TRIUMF, Vancouver, Canada V6T 2A3

^c and Institute of Nuclear Research, Debrecen, Hungary

^d and Heisenberg Fellow

^e and Department of Experimental Physics, University of Debrecen, Hungary

^f and MPI München

^g and Research Institute for Particle and Nuclear Physics, Budapest, Hungary

^h now at University of Liverpool, Dept of Physics, Liverpool L69 3BX, U.K.

ⁱ and CERN, EP Div, 1211 Geneva 23

^j and Manchester University

^k now at University of Kansas, Dept of Physics and Astronomy, Lawrence, KS 66045, U.S.A.

^l now at University of Toronto, Dept of Physics, Toronto, Canada

^m current address Bergische Universität, Wuppertal, Germany

ⁿ now at University of Mining and Metallurgy, Cracow, Poland

^o now at University of California, San Diego, U.S.A.

^p now at Physics Dept Southern Methodist University, Dallas, TX 75275, U.S.A.

^q now at IPHE Université de Lausanne, CH-1015 Lausanne, Switzerland

^r now at IEKP Universität Karlsruhe, Germany

^s now at Universitaire Instelling Antwerpen, Physics Department, B-2610 Antwerpen, Belgium

^t now at RWTH Aachen, Germany

^u and High Energy Accelerator Research Organisation (KEK), Tsukuba, Ibaraki, Japan

^v now at University of Pennsylvania, Philadelphia, Pennsylvania, USA

^w now at TRIUMF, Vancouver, Canada

^x now at DESY Zeuthen

^y now at CERN

^z now with University of Antwerp

* Deceased

1 Introduction

Measurements of fermion-pair production in e^+e^- collisions at high energies provide a sensitive test of Standard Model predictions, and allow limits to be set on many possible new physics processes [1–4]. In this paper we present measurements of cross-sections and angular distributions for hadronic and lepton-pair final states at centre-of-mass energies \sqrt{s} between 189 GeV and 209 GeV; forward-backward asymmetries for the leptonic states are also given. The data were collected by the OPAL detector at LEP in 1998, 1999 and 2000.

In the Standard Model, fermion-pair production proceeds via s -channel photon and Z diagrams, except for the e^+e^- final state where t -channel diagrams dominate. A general feature of e^+e^- collision data at these energies is radiative return to the Z. If one or more initial-state radiation photons are emitted which reduce the effective centre-of-mass energy of the subsequent e^+e^- collision, $\sqrt{s'}$, to the region of the Z resonance, the cross-section is greatly enhanced. A separation can be made between these radiative events and non-radiative events for which $\sqrt{s'} \simeq \sqrt{s}$. While the properties of radiative events are similar to those measured in Z decays at LEP 1, modified only by the boost due to recoil against hard initial-state radiation, non-radiative events have different properties, reflecting the increased relative importance of photon-exchange processes above the Z resonance. At the centre-of-mass energies considered here, the contribution of the photon-exchange diagram to the cross-section is about four times greater than that of the Z-exchange diagram for $\mu^+\mu^-$ and $\tau^+\tau^-$ final states with $\sqrt{s'} \simeq \sqrt{s}$.

The analyses presented here are similar to those already presented at lower energies [1–3]. We use identical techniques to measure s' and to separate non-radiative events, which have little initial-state radiation, from radiative return to the Z peak. We define non-radiative events as those having $s'/s > 0.7225$, while inclusive measurements correspond to $s'/s > 0.01$. We correct our measurements of hadronic, $\mu^+\mu^-$ and $\tau^+\tau^-$, but not e^+e^- , events to remove the effect of interference between initial- and final-state radiation, as in our previous publications. The treatment of the four-fermion contribution to the two-fermion final states is similar to that at lower energies. The precise signal definition is discussed in Section 2.

While the event selection for hadronic and e^+e^- final states is essentially unchanged from previous analyses, an improvement in the rejection of cosmic ray events in the $\mu^+\mu^-$ final state has led to a significant reduction in the uncertainty in the residual background. The event selection for $\tau^+\tau^-$ events has been tightened to reduce the background in this channel, also reducing one of the larger systematic uncertainties. In all channels, the higher luminosity and hence higher statistics now available have enabled a more thorough study of systematic effects. Combining data from three years has led to a significant reduction of the experimental systematic uncertainties compared with previous analyses; for example, the systematic error on the non-radiative hadronic cross-section has been reduced by $\sim 40\%$. To take advantage of these reduced systematic errors in fits to the Standard Model and searches for new physics we present updated results for the high statistics data at 189 GeV, together with new results at higher energies; the 189 GeV results supersede those presented in [1].

Measurements of fermion-pair production up to 189 GeV have shown very good agreement with Standard Model expectations [1–4]. Here we repeat our measurement of the electromagnetic coupling constant $\alpha_{\text{em}}(\sqrt{s})$ including the higher energy data. In addition, we combine results at energies above the Z peak (LEP 2) with those from data taken around the Z peak (LEP 1) to determine the mass of the Z boson and the size of the γ -Z interference contribution within the framework of the S-matrix formalism [5]. Including data at higher energies also allows us to extend the searches for new physics presented in [1]. In particular we obtain improved limits on the energy scale of a possible four-fermion contact interaction, and also present limits on the mass of a possible heavy Z' boson.

The paper is organized as follows. In Section 2 we discuss the signal definition, theoretical considerations and the corrections made to the data to obtain measurements corresponding to this definition. The data and Monte Carlo samples used in the analysis are described in Section 3, while Section 4 describes the data analysis and the cross-section and asymmetry measurements. In Section 5 we compare our measurements to the predictions of the Standard Model and use them to measure the energy dependence of α_{em} . The S-matrix analysis is presented in Section 6 and the results of searches for new physics in Section 7.

2 Signal Definition

To make precise tests of the Standard Model, the measurements of two-fermion processes must be compared with theoretical predictions calculated by, for example, the semi-analytical program **ZFITTER** [6]. We therefore need a signal definition for which the theoretical predictions can be made, and also which corresponds closely to the experimental measurements. The definition of the two-fermion signal used in this paper is the same as in previous publications [1–3]. For the e^+e^- final state it is described in Section 2.3 below. For hadronic, $\mu^+\mu^-$ and $\tau^+\tau^-$ final states it is as follows:

- s' is defined as the square of the mass of the Z/ γ propagator. A ‘non-radiative’ sample of events is defined by $s'/s > 0.7225$, while inclusive measurements correspond to $s'/s > 0.01$.
- Interference between initial- and final-state radiation makes the definition of s' ambiguous. To remove this ambiguity, the predicted contribution of interference is subtracted from the measured cross-sections, as described in Section 2.1.

- Four-fermion final states with a secondary pair arising from an initial-state photon in an s -channel diagram (i.e. initial state non-singlet photon diagrams, ISNS $_{\gamma}$ [7]) are considered to be signal if the primary pair passes the s' cut. Four-fermion final states arising from final-state photon diagrams (FS $_{\gamma}$) are included in the signal. This corresponds to definition 1 from [7] page 346. The procedure is discussed in detail in Section 2.2.
- Cross-section and asymmetry measurements are corrected to full 4π acceptance.

2.1 Interference between Initial- and Final-state Photons

The data include the effects of interference between initial- and final-state radiation, which needs to be subtracted from the measurements to form an unambiguous signal definition for comparison with theoretical predictions. We have investigated two methods of performing this subtraction. The first method is identical to that used in previous analyses, described fully in [3]. We define a differential ‘interference cross-section’, $d^2\sigma_{\text{IFSR}}/dm_{f\bar{f}} d\cos\theta$, as the difference between the differential cross-section including interference between initial- and final-state radiation and that excluding interference, as calculated by ZFITTER¹. The differential interference cross-section may be either positive or negative, depending on the values of the cosine of the angle θ between the fermion and the electron beam direction, and the invariant mass of the fermion pair $m_{f\bar{f}}$. We then estimate the fraction of this cross-section accepted by our selection cuts by assuming that, as a function of $\cos\theta$ and $m_{f\bar{f}}$, its selection efficiency $\epsilon_{\text{IFSR}}(\cos\theta, m_{f\bar{f}})$ is equal to $\epsilon_{\text{noint}}(\cos\theta, m_{f\bar{f}})$, where ϵ_{noint} has been determined from Monte Carlo events which do not include interference. The selected interference cross-section is then subtracted from the measured cross-section before efficiency correction, as for other backgrounds. As the accepted cross-section is estimated as a function of $\cos\theta$, the correction is easily applied to total cross-sections, angular distributions or asymmetry measurements.

The second method investigated uses special samples of Monte Carlo events generated with the KK2f program [8]. These samples were generated including initial-final-state photon interference with event weights allowing them to be reweighted to exclude the effects of interference. Applying selection cuts to these samples allowed the accepted ‘interference cross-section’ to be determined. The accepted cross-sections were in good agreement with those derived from the first method. In the case of hadronic events, the average of the two methods was used to correct the data and half the difference between them taken as the associated systematic error. For $\mu^+\mu^-$ and $\tau^+\tau^-$ final states the first method was used. As at lower energies, the systematic error was assessed by repeating the estimate assuming that the efficiency in each bin of $\cos\theta$ and $m_{f\bar{f}}$ was increased by half its difference with respect to the efficiency at $m_{f\bar{f}} = \sqrt{s}$ at the same $\cos\theta$.

The corrections to the final measured cross-sections and asymmetry measurements are given in Table 1.

2.2 Four-fermion Effects

The treatment of the four-fermion contribution to the two-fermion final states is similar to that at lower energies. Secondary pairs arising from initial-state photons in s -channel diagrams

¹Cross-sections including interference were calculated by setting the flag INTF=2, those excluding interference by setting INTF=0.

(ISNS _{γ}) are considered to be signal if the primary pair satisfies the s' cut. Pairs arising from final-state photons (FS _{γ}) are always considered to be signal. The overall efficiency of event selection cuts ϵ is calculated as

$$\epsilon = \left(1 - \frac{\sigma_{\bar{f}\bar{f}'\bar{f}'}}{\sigma_{\text{tot}}}\right) \epsilon_{\bar{f}\bar{f}} + \frac{\sigma_{\bar{f}\bar{f}'\bar{f}'}}{\sigma_{\text{tot}}} \epsilon_{\bar{f}\bar{f}'\bar{f}'} \quad (1)$$

where $\epsilon_{\bar{f}\bar{f}}$ and $\epsilon_{\bar{f}\bar{f}'\bar{f}'}$ are the efficiencies derived from two-fermion and four-fermion signal Monte Carlo events respectively, $\sigma_{\bar{f}\bar{f}'\bar{f}'}$ is the generated four-fermion signal cross-section, and σ_{tot} is the total cross-section from ZFITTER including pair emission. Using this definition of efficiency, effects of cuts on soft pair emission in the four-fermion generator are correctly summed with vertex corrections involving virtual pairs. For these analyses, a change has been made to the method used to separate the signal contribution from the background contribution in the four-fermion Monte Carlo events. At lower energies, separate samples of s -channel and t -channel four-fermion Monte Carlo events were generated, and the signal contribution was defined by kinematic cuts on the s -channel events, designed to include pair production via an initial-state photon but to exclude pair production via a Z boson. In this analysis, Monte Carlo samples including all four-fermion diagrams, generated with either the grc4f [9] program or with KORALW [10] with grc4f matrix elements, were used. Each event was given a weight to be signal (or background) calculated using the matrix elements of the appropriate diagrams. This method gives a definition of signal which is closer to that employed in the semi-analytic calculations with which we compare our results, and also avoids the necessity of generating special Monte Carlo samples.

The inclusion of the four-fermion part of the signal reduces efficiencies by about 0.3% for inclusive hadrons, 0.8% for inclusive muons and 1% for inclusive taus. For non-radiative events the effects are much smaller, less than 0.02% for hadrons and around 0.2% for muons and taus.

2.3 e⁺e⁻ Final States

The discussion above applies to hadronic, $\mu^+\mu^-$ and $\tau^+\tau^-$ final states. Because of ambiguities arising from the t -channel contribution, the acceptance for the e⁺e⁻ final state is defined in terms of the angle θ of the electron or positron with respect to the electron beam direction and the acollinearity angle θ_{acol} between the electron and positron; a cut on s' is not used. It is thus unnecessary to subtract interference between initial- and final-state radiation to make an unambiguous signal definition. Cross-sections and asymmetries for e⁺e⁻ are not corrected for interference between initial- and final-state radiation; they are compared to theoretical predictions which include interference. In principle the t -channel process with a second fermion pair arising from the conversion of a virtual photon emitted from an initial- or final-state electron should be included as signal, as well as the s -channel diagrams. Diagrams with real pairs are included in four-fermion Monte Carlo generators, but diagrams with virtual pairs are not included, and neither real nor virtual pairs are included in the program we use for comparison with the data. It would be improper to treat real pairs alone either as signal or background. We choose the best alternative, and simply ignore such events in both efficiency and background calculations. If the efficiency for four-fermion events is similar to that for two-fermion events, as is expected to be the case here, we are effectively comparing data including the four-fermion contribution to theory without. This does not introduce a large error because real and virtual pair contributions have opposite sign, and thus their effects tend to cancel in any total cross-section.

3 Data and Monte Carlo Simulations

3.1 Data

The OPAL detector², trigger and data acquisition system are fully described elsewhere [11–15]. The high redundancy of the trigger system leads to negligible trigger inefficiency for all channels discussed here.

The analyses presented in this paper use data recorded during 1998, 1999 and 2000. The 1998 data were recorded at a centre-of-mass energy near 189 GeV. In 1999, data were taken at four different centre-of-mass energy points, close to 192 GeV, 196 GeV, 200 GeV and 202 GeV. In 2000, a small amount of data was taken at centre-of-mass energies near 200 GeV and 202 GeV; these data have been included with the 200 GeV and 202 GeV data sets taken in 1999. The bulk of the 2000 data was taken at a range of centre-of-mass energies between 203 GeV and 209 GeV, as shown in Fig.1. Also, in 2000, the beam energy was changed within a run by a series of ‘miniramps’, resulting in a broad distribution of centre-of-mass energies rather than a series of discrete values as in previous years. Data taken while the beam energy was changing and other data with a poor beam energy measurement have been removed from these analyses. These data amount to about 1.1% of the total 2000 data set. For analysis the good data have been divided into two centre-of-mass energy ranges: 202.5 GeV – 205.5 GeV and > 205.5 GeV (henceforth referred to as 205 GeV and 207 GeV respectively); these are the energy ranges used for the combination of data from all LEP experiments. The mean centre-of-mass energy and approximate total integrated luminosity collected at each energy point are shown in Table 2; the actual amount of data varies slightly from channel to channel because of differing requirements on data quality.

3.2 Monte Carlo Simulations

The estimation of efficiencies and background processes makes extensive use of Monte Carlo simulations of many different final states. For studies of $e^+e^- \rightarrow q\bar{q}$ we used the KK2f [8] program, version 4.13. In KK2f photon radiation is modelled using Coherent Exclusive Exponentiation (CEEX) and complete $\mathcal{O}(\alpha^2)$ matrix elements for initial-state radiation are included. Hadronization was performed according to the PYTHIA6.150 [17] string model. Samples hadronized with the HERWIG6.2 [18] cluster model or ARIADNE4.11 [19] colour dipole model were used for systematic studies. In all cases input parameters have been optimized by a study of global event shape variables and particle production rates in Z decay data [20]. Final-state radiation from quarks was simulated as part of the hadronization process, and not by the KK2f program. For $e^+e^- \rightarrow e^+e^-$ we used the BHWIDE1.04 [21] Monte Carlo program, and for $e^+e^- \rightarrow \mu^+\mu^-$ and $e^+e^- \rightarrow \tau^+\tau^-$ KK2f was used with KORALZ4.0 [22] for comparison.

Four-fermion events were modelled with the grc4f [9] generator or with the KORALW [10] program with grc4f matrix elements. The latter has superior modelling of initial-state radiation in channels without electrons. Final states containing quarks were hadronized using PYTHIA, with HERWIG and ARIADNE used for systematic studies, as for the $e^+e^- \rightarrow q\bar{q}$ events. Two-photon background processes with hadronic final states were simulated using PYTHIA and

²OPAL uses a right-handed coordinate system in which the z axis is along the electron beam direction and the x axis is horizontal. The polar angle θ is measured with respect to the z axis and the azimuthal angle ϕ with respect to the x axis.

PHOJET [23] at low Q^2 . At high Q^2 the TWOGEN [24] program (with the ‘permiss’ option [25]), HERWIG and PHOJET were used. In the following, the terms ‘tagged’ and ‘untagged’ are used to denote the high- and low- Q^2 samples respectively. The BDK generator [26] was used to simulate two-photon processes resulting in $e^+e^-\mu^+\mu^-$ and $e^+e^-\tau^+\tau^-$ final states, while the Vermaseren generator [27] was used for the $e^+e^-e^+e^-$ final state. The $e^+e^- \rightarrow \gamma\gamma$ background in the e^+e^- final state was modelled with the RADCOR [28] program, while the contribution from $e^+e^-\gamma$ where the photon and one of the charged particles are inside the detector acceptance was modelled with TEEGG [29].

Monte Carlo samples were generated at 189 GeV, at the four nominal energy values of the data collected in 1999, and at several energies spanning the range 204 GeV to 208 GeV for simulation of the data taken in 2000. All samples were processed through the OPAL detector simulation program [30] and reconstructed in the same way as for real data. Efficiencies and backgrounds at the centre-of-mass energy values corresponding to the data were determined by fitting the energy dependence of these quantities.

For the measurement of the luminosity, the cross-section for small-angle Bhabha scattering was calculated using the Monte Carlo program BHLUMI [31], using generated events processed through a program which parameterizes the response of the luminometer [15].

4 Cross-section and Asymmetry Measurements

4.1 Luminosity

The integrated luminosity was measured using small-angle Bhabha scattering events, $e^+e^- \rightarrow e^+e^-$, recorded in the silicon-tungsten luminometer [15]. The luminometer consisted of two finely segmented silicon-tungsten calorimeters placed around the beam pipe, symmetrically on the left and right sides of the OPAL detector, 2.5 m from the interaction point. Each calorimeter covered angles from the beam between 25 mrad and 59 mrad. The luminosity determination closely followed the procedure used for the precise determination at LEP 1 [15]. However, before LEP 2 data-taking, tungsten shields designed to protect the tracking detectors from synchrotron radiation were installed. These introduced about 50 radiation lengths of material in front of the calorimeter between 26 mrad and 33 mrad from the beam axis, thus reducing the useful acceptance of the detector.

Bhabha scattering events were selected by requiring a high energy cluster in each side of the detector, using asymmetric acceptance cuts. The energy in each calorimeter had to be at least half the beam energy, and the total energy in the fiducial region of both calorimeters had to be at least three quarters of the centre-of-mass energy. The two highest energy clusters were required to be back-to-back in ϕ , $||\phi_R - \phi_L| - \pi| < 200$ mrad, where ϕ_R and ϕ_L are the azimuthal angles of the cluster in the right- and left-hand calorimeter respectively. They were also required to be collinear, by placing a cut on the difference between the radial positions, $\Delta R \equiv R_R - R_L$, at $|\Delta R| < 2.5$ cm, where R_R and R_L are the radial coordinates of the clusters on a plane approximately 7 radiation lengths into the calorimeter at $z = \pm 246.0225$ cm. This cut, corresponding to an acollinearity angle of about 10.4 mrad, effectively defines the acceptance for single-photon radiative events, thus reducing the sensitivity of the measurement to the detailed energy response of the calorimeter. The distribution of ΔR for the data taken in the year 2000 is shown in Fig. 2(a).

Inner and outer radial acceptance cuts delimited a region between 38 mrad and 52 mrad on one side of the calorimeter, while for the opposite calorimeter a wider zone between 34 mrad and 56 mrad was used. Two luminosity measurements were formed with the narrower acceptance on one side or the other side. The final measurement was the average of the two and has no first order dependence on beam offsets or tilts. The distributions of the radial coordinates of the clusters for the data taken in the year 2000 are shown in Fig. 2(b,c).

The acceptance A of the luminosity measurement is affected by any change in the inner and outer edges of the acceptance as follows:

$$\frac{\Delta A}{A} \approx -\frac{\Delta R_{\text{in}}}{21 \mu\text{m}} \times 10^{-3} \quad (2)$$

and

$$\frac{\Delta A}{A} \approx +\frac{\Delta R_{\text{out}}}{51 \mu\text{m}} \times 10^{-3}, \quad (3)$$

where R_{in} and R_{out} denote the radial coordinates of the inner and outer cuts. The coefficients in the expressions given above are determined by simple analytic calculations, using the $1/\theta^3$ Bhabha spectrum, the nominal half distance between the reference planes of the two calorimeters and the inner and outer acceptance radii (9.45 cm and 12.7 cm). The residual bias on the inner and outer cut positions was estimated as at LEP 1, by a procedure called *anchoring*, which is fully explained in [15]. In this approach the fundamental tool is the radial position of the silicon pad with maximum signal in a given longitudinal layer. As the radial position of the incoming particles crosses a radial pad boundary in a single layer, the average pad-maximum moves rapidly from one pad to the next, giving an image of the pad boundary, as shown in Fig. 3. The coordinate offset at the inner cut position was determined to be about 30 μm in both the right and the left calorimeter; this offset can be seen in Fig. 3. By applying Equation (2) this is equivalent to an acceptance variation of +0.14 %. At LEP 1 the absolute value of the coordinate offset at the inner cut was less than 10 μm . The larger value in LEP 2 data is attributed to the effects of about 2 radiation lengths of preshowering material, consisting of cables and beam pipe support structures, in front of the central angular region of the calorimeter including the position of the inner radial cut. The estimated systematic correction was applied to the measurement, but the full size of the effect was conservatively kept as a systematic error.

The errors on the luminosity measurement at each energy are summarized in Table 3. The experimental systematic error is dominated by the uncertainty of the inner radial cut. Among the other errors are trigger efficiency (0.06%), energy response particularly in the low energy tail (0.03%), beam parameters (0.02%), backgrounds (0.02%) and Monte Carlo statistics (0.08%), where all the numbers refer to year 2000 data but are fairly similar in the other data samples. The error on the theoretical prediction of the Bhabha cross-section of 0.12% is taken from [32].

The errors on luminosity are included in the systematic errors on cross-section measurements presented in this paper. Correlations between cross-section measurements arising from common errors in the luminosity have been taken into account in the interpretation of the results.

4.2 Hadronic Events

4.2.1 Event Selection

The selection of hadronic events is identical to previous analyses [1–3]. For both inclusive and non-radiative samples, the selection efficiency is typically $\sim 85\%$ and the purity is $\sim 92\%$.

- To reject leptonic final states, events were required to have high multiplicity: at least 7 electromagnetic clusters and at least 5 tracks satisfying standard quality criteria [3].
- Background from two-photon events was reduced by requiring a total energy deposited in the electromagnetic calorimeter of at least 14% of the centre-of-mass energy: $R_{\text{vis}} \equiv \sum E_{\text{clus}} / \sqrt{s} > 0.14$, where E_{clus} is the energy of each cluster.
- Any remaining background from beam-gas and beam-wall interactions was removed, and two-photon events further reduced, by requiring an energy balance along the beam direction which satisfied $R_{\text{bal}} \equiv |\sum (E_{\text{clus}} \cdot \cos \theta_{\text{clus}})| / \sum E_{\text{clus}} < 0.75$, where θ_{clus} is the polar angle of the cluster.
- At these centre-of-mass energies, the cross-section for production of W^+W^- events is comparable to that for non-radiative $q\bar{q}$ events, and the above selection cuts have high efficiency for those W^+W^- events with hadrons in the final state. Events selected as W^+W^- candidates using the criteria described in [33] (with reference histograms updated for the higher energy data) were therefore rejected. This cut also removes some of the (much smaller) contribution from ZZ final states. As a cross-check, an analysis was also performed in which W^+W^- candidates were not rejected, but their expected contribution subtracted.
- The effective centre-of-mass energy, $\sqrt{s'}$, of the e^+e^- collision, determined as described below, was required to satisfy $s'/s > 0.01$ for the inclusive sample and $s'/s > 0.7225$ for the non-radiative sample.

Distributions of selection variables, before applying the W^+W^- rejection and s' cuts, are shown in Fig. 4. The Monte Carlo modelling of these variables is generally very good, except at very low multiplicities.

The effective centre-of-mass energy $\sqrt{s'}$ of the e^+e^- collision was estimated as follows. The method is the same as that used in previous analyses [1–3]. Isolated photons in the electromagnetic calorimeter, with a minimum energy of 10 GeV, were identified, and the remaining tracks, electromagnetic and hadron calorimeter clusters formed into jets using the Durham (k_T) scheme [34] with a jet resolution parameter $y_{\text{cut}} = 0.02$. If more than four jets were found the number was forced to be four by adjusting the jet resolution parameter. The jet energies and angles were corrected for double counting of energy using the algorithm described in [35]. The jets and observed photons were then subjected to a series of kinematic fits imposing the constraints of energy and momentum conservation, in which zero, one, or two additional photons emitted close to the beam direction were allowed. The fit with the lowest number of extra photons which gave an acceptable χ^2 was chosen. The value of $\sqrt{s'}$ was then computed from the fitted four-momenta of the jets, i.e. excluding photons identified in the detector or those close to the beam direction resulting from the fit, which were assumed to arise from initial-state

radiation. If none of the kinematic fits gave an acceptable χ^2 , $\sqrt{s'}$ was estimated directly from the angles of the jets as in [36]. The distribution of $\sqrt{s'}$ for all energies combined is shown in Fig. 9(a).

The efficiency of the selection cuts was determined from Monte Carlo events generated with the KK2f program, without inclusion of interference between initial- and final-state photon radiation, and corrected for the effect of the four-fermion signal component as described in Section 2.2. The feedthrough of events with lower s' into the non-radiative sample and expected backgrounds were also determined from Monte Carlo. For both efficiencies and backgrounds a linear fit to values at centre-of-mass energies between 189 GeV and 208 GeV was used to determine the value at the mean centre-of-mass energy of the data. The KORALW Monte Carlo events used to estimate the four-fermion background do not include complete electroweak $\mathcal{O}(\alpha)$ corrections to the $e^+e^- \rightarrow W^+W^-$ process which are now available in the program KANDY [37]. The backgrounds calculated using KORALW were corrected using samples of events generated with KANDY. These corrections are small for the standard analysis, where W^+W^- candidates are rejected, but significant for the cross-check analysis in which W^+W^- events are not rejected. In this case they increase the measured inclusive and non-radiative cross-sections by 0.5% and 1.2% respectively. Efficiencies and backgrounds are summarized in Table 4.

To measure the angular distribution of the primary quark in the hadronic events, we have used as an estimator the thrust axis for each event determined from the observed tracks and clusters. The angular distribution of the thrust axis was then corrected to the primary quark level using bin-by-bin corrections determined from Monte Carlo events. For the bin size chosen, the bin-to-bin migration of events is $\sim 10\%$ to either side. No attempt was made to identify the charge in hadronic events, and thus we measured the folded angular distribution.

4.2.2 Systematic Uncertainties

The systematic errors on the hadronic cross-sections are summarized in Table 11, with a detailed breakdown at 200 GeV given in Table 12. Where no dependence on energy or year was expected or seen, the values were determined by combining data at all energies. The resulting high statistics have resulted in a reduction of many contributions compared with previous analyses.

Initial-state radiation modelling. Efficiencies were calculated using the KK2f generator with $\mathcal{O}(\alpha^2)$ Coherent Exclusive Exponentiation (CEEX) of radiation. To assess the effect of initial-state radiation on the selection efficiencies and s' determination, the events were reweighted to $\mathcal{O}(\alpha)$ CEEX. In accordance with the recommendations of [8], half the difference between $\mathcal{O}(\alpha)$ and $\mathcal{O}(\alpha^2)$ was assigned as the systematic error, reflecting the effects of missing higher order terms in the perturbative expansion.

Fragmentation modelling. The effect of the hadronization model on the selection efficiencies has been investigated by comparing the string model implemented in PYTHIA with the cluster model of HERWIG [18] and the colour-dipole model of ARIADNE [19]. To reduce the statistical errors on this comparison, the same primary quarks generated with KK2f were fragmented according to each model in turn, and the selection efficiencies compared. The deviations of the two predictions from the PYTHIA value were evaluated. Statistically significant differences were seen, and the larger of these was assigned as the systematic error. In addition, the effects on the efficiencies of changing the cuts on the number of tracks and clusters by one unit were also taken into account, to cover imperfections in the modelling of low multiplicity jets.

Detector effects. The selection of inclusive events is mainly based on the electromagnetic calorimeter, and is thus sensitive to the energy scale of the calorimeter, and any angular dependence of the energy scale. For non-radiative events, the selection is sensitive to jet and photon energies, angles, and their errors, and jet masses, which are used as input to the kinematic fits used to determine s' . Studies of calibration data taken at the Z peak have been used to determine small year-dependent corrections to these parameters in the Monte Carlo simulations. Variations of these corrections by their errors were used to assign corresponding systematic errors on the cross-sections. The uncertainty in the energy scale of the electromagnetic calorimeter leads to an error on the inclusive cross-sections of about 0.2%. The largest effect on the non-radiative cross-sections (0.12%) arises from the jet energy scale.

s' determination. Possible systematic effects in the determination of s' not already covered by the studies of initial-state radiation modelling, fragmentation modelling and detector effects were studied using two alternative methods of calculating s' . Firstly the default algorithm was modified to allow only a single radiated photon, either in the electromagnetic calorimeter or along the beam axis. Alternatively the cuts defining photon candidates in the detector were varied. The differences, averaged over all centre-of-mass energies, were not statistically significant, and the statistical precision of this test was included as a systematic error associated with the s' determination.

W^+W^- rejection cuts. The effect of the W^+W^- rejection cuts on the signal efficiency was studied using distributions of variables which distinguish W^+W^- events from $q\bar{q}$ events. In the case of $W^+W^- \rightarrow q\bar{q}q\bar{q}$ events the QCD matrix element for four-jet production, W_{420} [38] was used. This is an event weight formed from the $\mathcal{O}(\alpha_s^2)$ matrix elements for the four-jet production processes $e^+e^- \rightarrow q\bar{q} \rightarrow q\bar{q}q\bar{q}, q\bar{q}gg$. The distribution of W_{420} after all event selection cuts except the W^+W^- veto is shown in Fig. 5(a) for non-radiative events from the combined data sample. A clear separation between signal events and background events is seen. Figures 5(b) and (c) show the distributions for those events rejected by and passing the W^+W^- veto respectively. The distribution obtained from the data, before applying the W^+W^- rejection, was fitted with the sum of expected signal and background contributions, allowing the absolute normalization of both to vary. The fit region was chosen to include the majority of signal events rejected by the W^+W^- veto and a majority of background events which pass the veto, as illustrated in Fig. 5. The resulting scale factor for the signal, or its statistical error, was applied to the rejected signal cross-section to estimate the corresponding uncertainty in efficiency. In the case of $W^+W^- \rightarrow q\bar{q}\ell\nu$ events, a similar procedure was applied to the distribution of the magnitude of the vector sum of transverse momenta for all visible particles. In all cases, the scale factors were found to be consistent with unity.

Backgrounds. The uncertainty in the W^+W^- background was estimated from the fits to W_{420} and transverse momentum distributions (for $W^+W^- \rightarrow q\bar{q}q\bar{q}$ and $W^+W^- \rightarrow q\bar{q}\ell\nu$ respectively) described above for the W^+W^- rejection cuts. In addition, the effects of initial-state radiation modelling and fragmentation modelling on the four-fermion background were investigated by varying these models. In the inclusive sample, the largest background uncertainty arises from tagged two-photon events. This was investigated by comparing the predictions of different Monte Carlo generators: either a combination of HERWIG for single-tagged events plus PHOJET for double-tagged events, or TWOGEN for both. An average of the two prescriptions was found to give the best representation of the data at low s' , and was used in the cross-section determination, with half the difference between the two predictions taken as the systematic error. The (small) differences between the PYTHIA and PHOJET programs were used to assess

the systematic uncertainty in the untagged two-photon background. Similarly, the small uncertainties in the $\tau^+\tau^-$ background were estimated by comparing the predictions of KK2f and KORALZ.

Interference. The error arising from the subtraction of interference between initial- and final-state photon radiation was estimated from the difference between the two methods of determination as described in Section 2.1.

The results of the cross-check analysis, in which events identified as W^+W^- were not removed, but the expected contribution subtracted, are in excellent agreement with those of the primary analysis, with slightly larger total errors.

4.3 Muon Pairs

4.3.1 Event Selection

The selection of $\mu^+\mu^-$ events is essentially the same as in previous analyses [1], except that a small improvement has been made in the rejection of cosmic ray events leading to a reduction in the uncertainty associated with this background. The efficiency of the selection cuts is typically $\sim 74\%$ for inclusive events and $\sim 88\%$ for non-radiative events. The corresponding purities of the selected samples are $\sim 90\%$ and $\sim 97\%$ respectively.

- Muon pair events were required to have at least two tracks with momentum greater than 6 GeV, $|\cos\theta| < 0.95$, separated in azimuthal angle by more than 320 mrad, and identified as muons. These tracks must have at least 20 hits in the central tracking chambers and the point of closest approach to the nominal beam axis must lie less than 1 cm in the $r-\phi$ plane and less than 50 cm along the beam axis from the nominal interaction point. To be identified as a muon, a track had to satisfy any of the following conditions:
 - At least 2 muon chamber hits associated with the track within an azimuthal angular range $\Delta\phi = (100 + 100/p)$ mrad, with the momentum p in GeV;
 - At least 4 hadron calorimeter strips associated with the track within an azimuthal angular range $\Delta\phi = (20 + 100/p)$ mrad, with p in GeV. The average number of strips per layer, taken over all layers with at least one hit, had to be less than 2 to discriminate against hadrons. For $|\cos\theta| < 0.65$, where tracks traverse all 9 layers of strips in the barrel calorimeter, a hit in one of the last 3 layers of strips was required;
 - Momentum $p > 15$ GeV and less than 3 GeV electromagnetic energy associated to the track within a cone of half-angle 200 mrad.

If more than one pair of tracks satisfied the above conditions, the pair with the largest scalar sum of momenta was chosen. No requirement was made that the tracks have opposite charge.

- Background from high multiplicity events was rejected by requiring that there be no other track in the event with a transverse momentum (relative to the beam axis) greater than 1.65% of the beam energy.

- Background from cosmic ray events was removed using the time-of-flight (TOF) counters and vertex cuts. Figure 6(a) shows the distribution of the time difference, Δt , between pairs of back-to-back TOF counters for $\mu^+\mu^-$ candidates, clearly showing one peak at the origin from muon pairs and a second peak at about 15 ns from cosmic rays. Events were accepted if they had $-20 \text{ ns} < \Delta t < 8 \text{ ns}$ and at least one of the time measurements was within 10 ns of that expected for a particle coming from the interaction point. If only one TOF hit was recorded, it had to be within 10 ns of the expected time. In addition, events were required to pass loose cuts on the matching of the central detector tracks to the interaction vertex. Events without a good TOF hit were required to pass tight vertex criteria.
- Background from two-photon events was rejected by placing a cut on the total visible energy, E_{vis} , defined as the scalar sum of the momenta of the two muons plus the energy of the highest energy cluster in the electromagnetic calorimeter:

$$R_{\text{vis}} \equiv E_{\text{vis}}/\sqrt{s} > 0.5(m_Z^2/s) + 0.35.$$

The value of this cut is 0.15 below the expected value of R_{vis} for muon pairs in radiative return events where the photon escapes detection, visible as a secondary peak in Fig. 6(b). Furthermore, for inclusive events, if the ratio of the visible energy to the centre-of-mass energy was less than $0.5(m_Z^2/s) + 0.75$ the muon pair invariant mass was required to be greater than 70 GeV. For all non-radiative events the muon pair invariant mass was required to be greater than $\sqrt{(m_Z^2 + 0.1s)}$.

- The effective centre-of-mass energy $\sqrt{s'}$ of the e^+e^- collision, determined as described below, was required to satisfy $s'/s > 0.01$ for the inclusive sample and $s'/s > 0.7225$ for the non-radiative sample.

Roughly 10% of selected events have a photon detected in the electromagnetic calorimeter with an energy above 30 GeV, separated from the nearest muon by at least 20° . If such an event was planar, i.e. the sum of the angles between the three particles (two muons plus photon) was greater than 358° , the photon was assumed to be initial-state radiation and s' was calculated from the angles of the two muons and the photon using three-body kinematics. For all other events the value of s' was estimated from the polar angles θ_1 and θ_2 of the two muons, assuming massless three-body kinematics to calculate the energy of a possible undetected initial-state photon along the beam direction as

$$E_\gamma = \sqrt{s} \cdot |\sin(\theta_1 + \theta_2)| / (|\sin(\theta_1 + \theta_2)| + \sin \theta_1 + \sin \theta_2). \quad (4)$$

The observed distribution of $\sqrt{s'}$ for all data combined is shown in Fig. 9(b).

The selection efficiencies and feedthrough of events from lower s' into the non-radiative samples were determined from Monte Carlo events generated with KK2f without interference between initial- and final-state radiation, corrected for the four-fermion contribution as discussed in Section 2.2. Backgrounds were also determined from Monte Carlo simulations. Efficiencies and backgrounds at each energy are summarized in Table 4.

In approximately 2% of $\mu^+\mu^-$ events the two muon tracks have the same charge; for the asymmetry and angular distribution measurements this charge ambiguity was resolved using the acoplanarity of track segments reconstructed in the muon chambers. Acoplanarity is defined as

$|\phi_1 - \phi_2| - 180^\circ$ where ϕ_1 and ϕ_2 are the azimuthal angles of the muon segments. Bending of the charged particle trajectories in the magnetic field results in positive or negative acoplanarity depending on the charge of the particle with the lower value of ϕ . In the measurement of both the angular distributions and asymmetries, the final values were obtained by averaging the distribution measured using the negative muon with that using the positive muon; although this averaging does not reduce the statistical errors on the measurements, it is expected to reduce most systematic effects. The forward-backward asymmetries at each energy were obtained by counting the numbers of events in the forward and backward hemispheres, after correcting for background and efficiency. The asymmetries were corrected to the full angular range by applying a multiplicative correction obtained from ZFITTER to the asymmetry measured within the acceptance of the selection cuts ($|\cos \theta| < 0.95$).

4.3.2 Systematic Uncertainties

Systematic errors on the $\mu^+\mu^-$ cross-sections are summarized in Table 11, with a detailed breakdown at 200 GeV given in Table 13. The main contributions are discussed below.

Efficiency. The systematic uncertainty in the efficiency was evaluated using high statistics LEP 1 data and Monte Carlo samples. The $\mu^+\mu^-$ cross-section at the Z peak is well known: it has been measured with a systematic uncertainty of about 0.2% [39]. The $\mu^+\mu^-$ selection cuts were applied to the LEP 1 data and Monte Carlo samples. A statistically significant difference between the number of data events selected and the number expected from Monte Carlo was observed, and this difference was used to estimate the systematic error associated with the efficiency. Most kinematic cuts are a function of \sqrt{s} and scale smoothly to the Z peak; for this comparison it was necessary only to relax the cut on the visible energy so that the efficiency for events on the Z peak remained high. LEP 2 events have a different angular distribution from LEP 1 events, and in particular radiative events are boosted towards the endcap regions of the detector. The agreement between data and Monte Carlo was therefore checked as a function of $\cos \theta$, and the results were reweighted to the angular distribution of the high energy data to obtain the systematic error on the total cross-section. To check for possible changes of the detector response with time, this procedure was repeated with the calibration data taken at the Z during 1998–2000; the observed difference between data and Monte Carlo was consistent with that determined from the LEP 1 study, but with poorer statistical precision.

Initial-state radiation modelling. The systematic error on efficiency derived from the LEP 1 data does not include the effects of uncertainties in the modelling of initial-state radiation. As for hadronic events, this uncertainty was estimated by reweighting KK2f events from $\mathcal{O}(\alpha^2)$ to $\mathcal{O}(\alpha)$ CEEX and taking half the predicted change in efficiency.

Feedthrough. The uncertainty in the feedthrough of events with lower s' into the $s'/s > 0.7225$ sample was estimated by comparing the prediction of KK2f with that of KORALZ.

Cosmic background. The uncertainty due to any remaining cosmic background in the muon pairs was estimated from the vertex distribution of events after relaxing some of the time-of-flight and vertex criteria.

Other backgrounds. The main backgrounds in the muon pairs arise from various leptonic four-fermion final states and from tau pairs. The four-fermion backgrounds are principally channels including at least two muons, and include a significant contribution from production of $e^+e^-\mu^+\mu^-$ final states via two-photon processes. Backgrounds were studied by considering

distributions of selection variables after loosening some of the selection cuts. The numbers of events in data and Monte Carlo were compared for a region enriched in a particular background, and the difference, or its statistical error, whichever was greater, used to estimate the systematic error from that background source. For example, the two-photon $e^+e^-\mu^+\mu^-$ background was studied using the distribution of visible energy after removing the cuts on visible energy and muon-pair mass, shown in Fig. 6(b); the comparison was made in the visible energy range between 10% and 40% of the centre-of-mass energy, which is completely dominated by this background.

Interference. The uncertainty arising from the removal of the contribution from interference between initial- and final-state radiation was estimated as described in Section 2.1.

Asymmetry. Systematic uncertainties in the asymmetry measurement were assessed by comparing results obtained using different combinations of tracking and muon chambers to measure the muon angles. The change in asymmetry when same-sign events were excluded from the sample was included as a systematic error. Other small contributions arise from the efficiency and background correction and subtraction of interference between initial- and final-state radiation.

4.4 Tau Pairs

4.4.1 Event Selection

The selection of $e^+e^- \rightarrow \tau^+\tau^-$ events is based on that used in previous analyses [1], using information from the central tracking detectors and electromagnetic calorimetry to identify events with two collimated, low multiplicity jets. However, the cuts have been tightened to improve the background rejection at higher energies. The efficiency of the selection cuts is typically $\sim 33\%$ for inclusive events and $\sim 48\%$ for non-radiative events. The corresponding purities of the selected samples are $\sim 88\%$ and $\sim 92\%$ respectively.

Tracks and electromagnetic clusters, each treated as separate particles with no attempt to correct for double-counting of energy, were combined into jets in the following way. First the highest energy particle in the event was selected and a cone with a half angle of 35° was defined around it. The particle with the next highest energy inside the cone was combined with the first. The momenta of the combined particles were added and the direction of the sum was used to define a new cone, inside which the next highest energy particle was again sought. This procedure was repeated until no more particles were found inside the cone. Similarly, starting with the highest energy particle among the remainder, a new cone was initiated and treated in the same way. This process continued until finally all the particles in the event had been assigned to a cone.

The following cuts were applied to select $\tau^+\tau^-$ candidates.

- Hadronic events were rejected by demanding low multiplicity: the number of tracks reconstructed in the central tracking detectors had to be at least two and at most six, and the sum of the number of tracks plus the number of electromagnetic clusters not more than 15.
- The total energy of an event was restricted in order to reject events from $e^+e^- \rightarrow e^+e^-(\gamma)$, $\mu^+\mu^-(\gamma)$ and two-photon processes. The total event energy, E_{tot} , defined as the scalar

sum of all track momenta plus all electromagnetic calorimeter energy, was required to be less than $1.1\sqrt{s}$. The total electromagnetic calorimeter energy was required to be between $0.02\sqrt{s}$ and $0.7\sqrt{s}$ and the scalar sum of track momenta less than $0.8\sqrt{s}$. Either the total electromagnetic calorimeter energy or the scalar sum of track momenta was required to be greater than $0.2\sqrt{s}$. The distribution of E_{tot}/\sqrt{s} , after all other cuts have been applied, is shown in Fig. 7(a) for all centre-of-mass energies combined. The agreement between data and simulation is good in the region dominated by the $\tau^+\tau^-$ signal, but poor in regions dominated by background; this discrepancy is used to estimate the systematic uncertainty in the background.

- Background from two-photon events was further reduced by cuts on the missing momentum and its direction. The missing momentum in the plane transverse to the beam axis, calculated using the electromagnetic calorimeter, was required to exceed $0.015\sqrt{s}$, and the polar angle of the missing momentum was required to satisfy $|\cos \theta| < 0.99$. Fig. 7(b) shows the distribution of the missing momentum after all other cuts have been applied, for all centre-of-mass energies combined.
- Vertex and TOF cuts were imposed to remove cosmic ray events, as for $\mu^+\mu^-$ events. In addition, events identified as $e^+e^- \rightarrow \mu^+\mu^-$ using the criteria described in Section 4.3 were removed.
- Cones formed from tracks and clusters as described above were classified as either charged or neutral. A charged cone was required to contain at least one charged particle with transverse momentum greater than 100 MeV and one electromagnetic cluster with energy greater than 100 MeV, and the sum of the energy in the electromagnetic calorimeter and the track momenta in the cone had to be more than 1% of the beam energy. Neutral cones were required to contain no charged particle and an energy in the electromagnetic calorimeter of at least 1% of the beam energy. Cones failing these criteria were discarded. Events which had exactly two charged cones were selected as $e^+e^- \rightarrow \tau^+\tau^-$ candidates. The direction of each τ was approximated by that of the total momentum vector of its cone of particles. Events were accepted if both cones satisfied $|\cos \theta| < 0.9$. To remove events with poor momentum reconstruction, the event was rejected if the azimuthal angle of either cone, determined using tracks only, lay within 0.5° of an anode plane of the central tracking chamber. In addition to the two charged cones, an event may contain any number of neutral cones.
- To suppress electron- and muon-pair events further, we reject events with cone energies or momenta compatible with these final states. Assuming that the final state consists only of two leptons plus a single unobserved photon along the beam direction, the values of the polar angles of the two τ cones were used to calculate the expected energy of each lepton X_1, X_2 . It was required that

$$0.02 < \sqrt{(E_1^2 + E_2^2)/(X_1^2 + X_2^2)} < 0.8,$$

and

$$\sqrt{(P_1^2 + P_2^2)/(X_1^2 + X_2^2)} < 0.8,$$

where E_1, E_2 and P_1, P_2 are the total electromagnetic calorimeter energies and scalar sums of track momenta, respectively, in each τ cone.

- Remaining background from $e^+e^- \rightarrow e^+e^-(\gamma)$ and $e^+e^-e^+e^-$ events was reduced by rejecting events if the ratio of the electromagnetic energy to the track momentum in each of the τ cones was consistent with that expected for an electron.
- Most of the remaining background from two-photon processes was rejected by a cut on the acollinearity and acoplanarity angles of the two τ cones: the acollinearity angle, in degrees, was required to satisfy

$$\theta_{\text{acol}} < (180^\circ - 2 \tan^{-1}(2m_Z \sqrt{s}/(s - m_Z^2))) + 10^\circ$$

and the acoplanarity angle was required to be less than 30° . The value of the cut on acollinearity was chosen such as to include the peak from radiative return events at each energy; it is 92° at 200 GeV. The acoplanarity cut was not applied to events with a photon observed in the detector with energy above 30 GeV, if the event was planar (i.e. the sum of the opening angles between the three particles was greater than 358°).

- Events classified as W^+W^- candidates according to the criteria in [33] were rejected.
- After the above cuts, the region of $\sqrt{s'}$ between the radiative return and full energy peaks, $110 \text{ GeV} < \sqrt{s'} < 0.85\sqrt{s}$, still contains a significant fraction of background from two-photon events. To reduce this background, a likelihood for the process $e^+e^- \rightarrow \tau^+\tau^-$ was formed from four variables: the missing momentum calculated using electromagnetic clusters, the scalar sum of the track momenta, the invariant mass of the two τ cones and the difference between the electromagnetic calorimeter energy in the two τ cones. The value of this likelihood was required to be greater than 0.5.
- The effective centre-of-mass energy $\sqrt{s'}$ was determined in an identical manner to the determination for muon pairs. The observed distribution of $\sqrt{s'}$ for all energies combined is shown in Fig. 9(c). Inclusive events were required to satisfy $s'/s > 0.01$ and non-radiative events were required to have $s'/s > 0.7225$.

The selection efficiencies and feedthrough of events from lower s' into the non-radiative samples were determined from Monte Carlo events generated with KK2f without interference between initial- and final-state radiation, corrected for the four-fermion contribution as discussed in Section 2.2. Backgrounds were also determined from Monte Carlo simulations. Efficiencies and backgrounds at each energy are summarized in Table 4.

For the measurement of the angular distributions and asymmetries, the small ($\sim 2\%$) fraction of events where the two τ cones have the same charge (as determined from the sum of the charges of the tracks in the cone) was not used. The final values were obtained by averaging the distribution measured using the negative τ with that using the positive τ , as for the muon pairs. The forward-backward asymmetries at each energy were obtained by counting the numbers of events in the forward and backward hemispheres, after correcting for background and efficiency. The asymmetries were corrected to the full angular range by applying a multiplicative correction obtained from ZFITTER to the asymmetry measured within the acceptance of the selection cuts ($|\cos \theta| < 0.9$).

4.4.2 Systematic Uncertainties

Systematic errors on the $\tau^+\tau^-$ cross-sections are summarized in Table 11, with a detailed breakdown at 200 GeV given in Table 14. The main contributions are discussed below.

Efficiency. The systematic error on the efficiency was evaluated using high statistics LEP 1 data and Monte Carlo samples, as for the muon pairs. The $\tau^+\tau^-$ cross-section at the Z peak has been measured with a systematic uncertainty of about 0.5% [39]. As in the case of muon pairs, a statistically significant difference between the observed and expected numbers of events was seen, and the difference was assigned as the systematic error associated with the selection cuts.

Initial-state radiation modelling. The systematic error on efficiency derived from the LEP 1 data does not include the effect of uncertainties in the modelling of initial-state radiation. As for hadronic events and muon pairs, this was estimated by reweighting KK2f events from $\mathcal{O}(\alpha^2)$ to $\mathcal{O}(\alpha)$ CEEX and taking half the predicted change in efficiency.

Feedthrough. The uncertainty in the feedthrough of events with lower s' into the $s'/s > 0.7225$ sample was estimated by comparing the prediction of KK2f with that of KORALZ.

Backgrounds. The largest background in the tau pairs arises from Bhabha events. Other important backgrounds arise from $e^+e^-e^+e^-$ and $e^+e^-\tau^+\tau^-$ final states. As for the muon pairs, systematic errors on each background channel were assessed by comparing data and Monte Carlo distributions of selection variables, after loosening selection cuts, in a region enriched in the particular background under study. For example, the $e^+e^-\mu^+\mu^-$ background was studied using the distribution of total event energy. For small backgrounds which cannot be studied in this way, we conservatively assume an error of 50%.

Interference. The uncertainty arising from the removal of the contribution from interference between initial- and final-state radiation was estimated as described in Section 2.1.

Asymmetry. Systematic errors on the asymmetry measurement were assessed by comparing different methods of determining the asymmetry: using tracks, electromagnetic clusters or both to determine the τ angles.

4.5 Electron Pairs

The production of electron pairs is dominated by t -channel photon exchange, for which a definition of s' as for the other channels is less meaningful. In addition, the increased probability for final-state radiation relative to initial-state radiation renders the separation between initial- and final-state photons more difficult. Events with little radiation were therefore selected by a cut on θ_{acol} , the acollinearity angle between electron and positron. We measure cross-sections for three different acceptance regions, defined in terms of the angle of the electron, θ_{e^-} , or positron, θ_{e^+} , with respect to the incoming electron direction, and the acollinearity angle:

- **A:** $|\cos \theta_{e^-}| < 0.9, |\cos \theta_{e^+}| < 0.9, \theta_{\text{acol}} < 170^\circ$; this is a loose ‘inclusive’ measurement;
- **B:** $|\cos \theta_{e^-}| < 0.7, \theta_{\text{acol}} < 10^\circ$; this acceptance region is enriched in the s -channel contribution, and is used for asymmetry measurements;
- **C:** $|\cos \theta_{e^-}| < 0.96, |\cos \theta_{e^+}| < 0.96, \theta_{\text{acol}} < 10^\circ$; this ‘large acceptance’ region is enriched in the t -channel contribution and acts as a check on the luminosity measurements.

In addition, we measure the electron angular distribution in the region:

- **D:** $|\cos \theta_{e^-}| < 0.9$, $\theta_{\text{acol}} < 10^\circ$.

In all cases, measurements are corrected to correspond to electron and positron energies each greater than 0.2 GeV.

4.5.1 Event Selection

The selection of e^+e^- events is identical to previous analyses [1–3]. The selection efficiencies are typically $\sim 98\%$, and the purities of the selected samples $\sim 98\%$.

- Events were required to have at least two and not more than eight clusters in the electromagnetic calorimeter, and not more than eight tracks in the central tracking chambers.
- At least two clusters were required to have an energy exceeding 20% of the beam energy, and the total energy deposited in the electromagnetic calorimeter was required to be at least 50% of the centre-of-mass energy. For the large acceptance selection, C, which has no requirement on the association of tracks to clusters, the total electromagnetic energy was required to be at least 70% of the centre-of-mass energy. Distributions of total electromagnetic calorimeter energy, after all other cuts, are shown in Fig. 8(b) and (c) for acceptance regions B and C for the data from all years combined. There is reasonable agreement between data and Monte Carlo. The apparent slight excess of data over Monte Carlo at about 80% of the centre-of-mass energy in acceptance B results from poor modelling of the energy resolution in the region $0.6 < |\cos \theta| < 0.7$. The degraded energy resolution in acceptance region C arises from the increased amount of material in front of the electromagnetic calorimeter at large $|\cos \theta|$, where the events are concentrated. The detailed modelling of the electromagnetic calorimeter energy resolution has very little effect on the selection efficiency for e^+e^- events.
- For selections A, B and D, at least two of the three highest energy clusters were required to have an associated central detector track. If a cluster had more than one associated track, the one with the highest momentum was chosen. If all three clusters had an associated track, the two highest energy clusters were chosen to be the electron and positron. For the large acceptance selection, C, no requirement was placed on the association of tracks to clusters.
- For the measurement of the forward-backward asymmetry and the angular distribution, the two tracks were required to have opposite charge. This extra requirement reduces the efficiency by about 3.5% in the region $|\cos \theta| < 0.9$. In addition, due to the extreme charge asymmetry for electrons in the forward direction, the problem of charge misassignment becomes severe for backward events at small angles. In the measurement of the angular distribution we therefore demanded that events with $\cos \theta_{e^-} < -0.8$ satisfy two extra criteria: both electron and positron tracks must have momentum greater than 25% of the beam momentum, and there must be only one good track associated with each cluster. These criteria significantly reduce the problem of charge misassignment, reducing the contamination from wrong-sign events in this region from around 35% to about 15%.

- Acceptance cuts on acollinearity and $\cos \theta$ were made using the calorimeter clusters, with angles corrected for the position of the primary vertex. The acollinearity angle distribution for the inclusive selection, A, is shown in Fig. 8(a), and we see good agreement between data and Monte Carlo expectation, including the peak corresponding to s -channel radiative return to the Z.

These cuts have a very high efficiency for e^+e^- events while providing excellent rejection of backgrounds, which either have high multiplicity or lower energy deposited in the electromagnetic calorimeter. The efficiency of the selection cuts, and small acceptance corrections, have been determined using Monte Carlo events generated with the BWIDE [21] program. These were found to be almost independent of energy over the range considered here. Small corrections have been applied to the efficiencies derived from Monte Carlo simulations to account for tracking losses near the central jet chamber anode planes ($\sim 0.8\%$), and, in the case of the angular distribution, to account for a discrepancy between data and Monte Carlo in the fraction of events where both tracks have the same charge ($\sim 0.5\%$). Remaining backgrounds arise from $\tau^+\tau^-$ events and, in the case of the loose acollinearity cut, also from electron pairs in two-photon events and from radiative Bhabha scattering events in which one electron is outside the detector acceptance but the photon is within the acceptance. In the case of the large acceptance selection, C, which does not require tracks, the main background arises from $\gamma\gamma$ final states. The efficiencies and backgrounds at each energy are summarized in Table 4.

The forward-backward asymmetries for the $\theta_{\text{acol}} < 10^\circ$ sample at each energy within the angular range $|\cos \theta_{e^-}| < 0.7$ were evaluated by counting the numbers of events in the forward and backward $\cos \theta_{e^-}$ hemispheres, after correcting for background and efficiency. For both the asymmetry and angular distribution measurements, the positive or negative track was used on alternate events to reduce systematic effects.

In Fig. 9(d) we show the distribution of $\sqrt{s'}$ for the inclusive e^+e^- events for all energies combined. The value of s' for each event was estimated from the polar angles of the two electrons assuming massless three-body kinematics to calculate the energy of a possible undetected initial-state photon along the beam direction as shown in Equation (4). For e^+e^- , s' is not really well-defined, but this calculation gives an estimate of s' for that part of the cross-section proceeding via the s -channel. Due to the dominance of the t -channel contributions, for electrons, in contrast to the other final states, the radiative return peak forms only a very small contribution.

4.5.2 Systematic Uncertainties

The systematic errors associated with the e^+e^- measurements have generally been estimated in a similar manner to the previous analysis [1]. They are summarized in Table 11, with a detailed breakdown at 200 GeV given in Table 15. The most significant change is that the systematic errors on the differential cross-section measurements (acceptance D) have been estimated separately for three $\cos \theta$ regions, namely $\cos \theta_{e^-} < -0.7$, $|\cos \theta_{e^-}| < 0.7$ and $\cos \theta_{e^-} > +0.7$, rather than considering the whole distribution together. The systematic errors are not expected to be strongly dependent on centre-of-mass energy, so in general they have not been estimated separately for each energy point. The most important ones are discussed below.

Four-fermion contribution. The full size of the change in efficiency arising from including s -channel four-fermion events in the signal definition was included as a systematic error.

This affects the inclusive selection (selection A) only, and is negligible for events with a tight acollinearity cut.

Multiplicity cuts. The uncertainties arising from the requirement of low multiplicity have been estimated from the change in the number of selected events in data when varying the multiplicity cuts used by ± 1 unit.

Calorimeter energy scale and resolution. A detailed comparison between data and Monte Carlo has been made of the energy scale and resolution of the electromagnetic calorimeter, and the results of this study used to assess possible effects on the selection efficiency. Typically the energy scale was varied by 0.3% and the resolution by 10% of its value.

Track requirements. Matching between tracks and clusters has been studied using events passing all selection cuts, except that only one of the three highest energy clusters has an associated track. These events are expected to be mainly $e^+e^-\gamma$ final states where one electron and the photon lie within the acceptance and $\gamma\gamma$ final states where one photon has converted in the detector, with small contributions from other final states. An excess of such events was seen in data compared with Monte Carlo expectation. Part of this excess is concentrated in regions of ϕ near the anode planes of the central jet chamber, and arises from track reconstruction problems in this region. The rest could arise from track reconstruction problems, or could arise from problems modelling $e^+e^-\gamma$ or $\gamma\gamma$ events. For each acceptance region we take the excess seen around the jet chamber anode planes plus half the difference between data and Monte Carlo in the remaining region of ϕ as a correction to the efficiency. This correction is typically around 0.8%. Half the difference between data and Monte Carlo in the regions of ϕ away from the jet chamber anode planes is taken as the systematic error associated with track reconstruction. In the case of the angular distribution, the two tracks in an event are required to have opposite charge. The fraction of same-sign events in data is roughly 0.5% greater than in Monte Carlo. This difference is applied as a correction to the efficiency derived from Monte Carlo, and the value of the correction is included as a systematic error. The higher probability of same-sign events in the data is also used to calculate a correction of $(1.6 \pm 0.5)\%$ to the angular distribution in the region $\cos\theta_{e^-} < -0.7$ arising from charge misassignment.

Acceptance correction. Because of the steepness of the angular distribution, uncertainties in the determination of θ are an important systematic error. These have been assessed by comparing measurements of θ in the electromagnetic calorimeter with those in the central tracking chambers and the muon chambers, using e^+e^- or $\mu^+\mu^-$ events as appropriate. These studies indicate a possible bias in the θ reconstruction of electromagnetic clusters of ~ 1 mrad in the endcap region of the detector. The effect of the observed biases on the acceptance was calculated using Monte Carlo events, and assigned as a systematic error associated with the acceptance correction.

Background. If a tight acollinearity cut is applied, the dominant background in the selections including tracks is from $\tau^+\tau^-$ events. With a loose acollinearity cut, $e^+e^-\gamma$ and $e^+e^-e^+e^-$ events are also significant. The systematic error arising from uncertainty in the background has been assessed by comparing the numbers of events in data and Monte Carlo which pass all cuts except the cut on total calorimeter energy; these events are predominantly background. In each acceptance region the larger of the difference between data and Monte Carlo or the statistical precision of the test was taken as the associated systematic error. For the selection which does not use tracks, acceptance C, the only important background is from $\gamma\gamma$ final states; here we used the statistical precision of the OPAL $e^+e^- \rightarrow \gamma\gamma$ cross-section measurement [40] to estimate the uncertainty in this background.

Asymmetry. Systematic uncertainties in the asymmetry measurement arise from the effects of θ mismeasurement, charge misassignment and background and efficiency corrections, and amount to 0.004.

4.6 Results

The numbers of selected events and measured cross-sections for all channels are summarized in Table 5. Asymmetries for the leptonic final states are summarized in Table 6, while the measured differential cross-sections are given in Tables 7, 8, 9 and 10 for hadrons, $\mu^+\mu^-$, $\tau^+\tau^-$ and e^+e^- respectively.

5 Comparison with Standard Model Predictions

The cross-section and asymmetry measurements at 189–207 GeV are compared with the Standard Model predictions in Tables 5–6. Figures 10–13 show cross-sections, for both inclusive and non-radiative events, as a function of \sqrt{s} , while Fig. 14 shows the measured asymmetry values. The Standard Model predictions are calculated using BHWIDE [21] for the e^+e^- final state and ZFITTER [6] for all other final states; in this paper we use ZFITTER version 6.30 with the following input parameters: $m_Z = 91.1852$ GeV [39], $m_{top} = 174.3$ GeV [41], $m_{Higgs} = 115$ GeV, $\Delta\alpha_{had}^{(5)} = 0.02761$ [42] and $\alpha_s(m_Z^2) = 0.1185$ [41]. The theoretical uncertainties on the cross-section predictions are estimated to be 0.26% for hadronic final states, 0.4% for muon and tau final states, 0.5% for electron final states in the endcap region and 2.0% for electron final states in the barrel region [7]. In the fits described in Section 7 we assign these values as the theoretical errors on the Standard Model cross-sections. For the non-radiative asymmetry values we use a theoretical error of 0.004, derived from comparison of the predictions of ZFITTER and KK2f. The agreement between the measured cross-sections and asymmetry values and the Standard Model predictions is generally good.

The measured differential cross-sections at each energy are given in Tables 7–10. The luminosity-weighted averages of data at all energies are compared with Standard Model predictions in Figs. 15 and 16. The data are well-described by the Standard Model curves.

In order to make a more quantitative test of the compatibility of our cross-sections and asymmetries with the Standard Model, we calculate a χ^2 value between the measurements and the Standard Model predictions taking into account statistical and systematic errors and their correlations. Correlations between hadron and lepton cross-sections are very small, arising mainly from the common luminosity measurements. Correlations between cross-sections at different energies for the same channel arise from the systematic uncertainties in both efficiency and background, but amount at most to 7.6% for hadrons, 4.8% for $\mu^+\mu^-$ and 11.4% for $\tau^+\tau^-$. Correlations between cross-section and asymmetry measurements are generally negligible, amounting at most to about 1% for $\tau^+\tau^-$, arising from uncertainties in the (mainly Bhabha) background.

The χ^2 values for the hadronic cross-sections, and the $\mu^+\mu^-$ and $\tau^+\tau^-$ cross-sections and asymmetries, are shown in Table 16. Note that the ‘non-radiative’ samples with $s'/s > 0.7225$ are a subset of the inclusive events with $s'/s > 0.01$, so the two χ^2 values are not independent. All measurements are in agreement with the Standard Model expectations.

The χ^2 test would not necessarily reveal a discrepancy in the overall scale of the cross-sections or asymmetries compared with the Standard Model expectations. Therefore, as a further check, we have also calculated the average value of the ratio of the measurement to the Standard Model prediction, using a χ^2 minimization technique including the experimental systematic errors. The results are shown in Table 16. All mean values are compatible with unity. The data are thus shown to be compatible with the Standard Model expectations to a precision of 1% for hadrons and $\sim 3\%$ for leptons.

The cross-sections for e^+e^- events are dominated by the large $\cos\theta$ region. Rather than comparing the measured integrated cross-sections with the Standard Model, we have calculated a χ^2 for the differential cross-sections, as presented in Table 10. Correlations between $\cos\theta$ bins and between energies are less than 10%, except for the region $\cos\theta > 0.7$ where the systematic error is a significant fraction of the total error; in this region the correlation between measurements at different energies is 30%–40%. We find a χ^2 value of 83.3 for 105 degrees of freedom, showing excellent agreement.

5.1 Energy Dependence of α_{em}

In [1–3] we used non-radiative cross-section and asymmetry measurements to determine the electromagnetic coupling constant α_{em} at LEP 2 energies. We have repeated this fit including the new measurements of hadronic, $\mu^+\mu^-$ and $\tau^+\tau^-$ cross-sections and the $\mu^+\mu^-$ and $\tau^+\tau^-$ asymmetry values for $s'/s > 0.7225$ presented here. As before, we form the χ^2 between the measured values and the Standard Model predictions calculated as a function of $\alpha_{\text{em}}(\sqrt{s})$ using ZFITTER, with all other ZFITTER input parameters fixed [6]. Correlations between measurements are fully taken into account. In Table 17 we show the results of these fits. We perform fits to the data at each energy and also perform a fit to data at all centre-of-mass energies in which α_{em} runs with energy with a slope³ obtained from fixing $1/\alpha_{\text{em}}(0) = 137.036$. As input to the combined fit we use the new measurements presented here together with the corresponding measurements at 130–183 GeV from [2, 3]. For the combined fit the value of α_{em} is quoted at the centre-of-mass energy corresponding to the luminosity-weighted average of $1/s$. The errors on the fitted values of α_{em} arise from the errors on the measurements; errors due to uncertainties in the ZFITTER input parameters are negligible. The measured values of α_{em} are shown in Fig. 17. They are consistent with the Standard Model expectations.

The fits described above use measurements of cross-sections which depend on the measurement of luminosity. The luminosity measurement assumes the Standard Model running of α_{em} from $Q^2 = 0$ to typically $Q^2 = (4 \text{ GeV})^2$, where⁴ $1/\alpha_{\text{em}} \simeq 134$. The fits therefore measure the running of α_{em} only from $Q_{\text{lumi}} \simeq 4 \text{ GeV}$ upwards. To become independent of the luminosity measurement, we have repeated the fits replacing the cross-sections for hadrons, muon and tau pairs with the ratios $\sigma(\mu\mu)/\sigma(q\bar{q})$ and $\sigma(\tau\tau)/\sigma(q\bar{q})$. This is possible since, above the Z peak, hadrons and leptons have very different sensitivity to α_{em} as discussed in [3]. The results of these fits are also shown in Table 17. The values of $1/\alpha_{\text{em}}$ are close to those obtained from the cross-section fits but with somewhat larger errors. The value of $1/\alpha_{\text{em}}$ obtained from the combined fit is $1/\alpha_{\text{em}}(193.2 \text{ GeV}) = 126.7^{+2.4}_{-2.3}$. This is about 4.3 standard deviations below the low energy limit of $137.03599976(50)$ [45], thus demonstrating the running of α_{em} from $Q^2 = 0$.

³If the Standard Model running of α_{em} is given by $\alpha_{\text{em}}^{\text{SM}} = \alpha_{\text{em}}(0)/(1 - \Pi(Q))$, then we determine a constant κ close to 1 such that $\alpha_{\text{em}}^{\text{fit}} = \alpha_{\text{em}}(0)/(1 - \kappa\Pi(Q))$, i.e. the slope $d\alpha_{\text{em}}/d\ln Q$ is multiplied by κ .

⁴The hadronic vacuum polarization contribution used in the luminosity measurement is from [46].

to LEP 2 energies. This measurement of α_{em} does not depend on calculations of low-mass hadronic loops and is nearly independent of the mass of the Higgs boson and α_s ; it can be scaled to the mass of the Z, giving $1/\alpha_{\text{em}}(91.19 \text{ GeV}) = 127.9^{+2.1}_{-2.8}$, in good agreement with the Standard Model prediction of 128.936 ± 0.046 [42].

6 S-matrix Analysis

6.1 Introduction

Fermion-pair production cross-sections and asymmetries at LEP 1 provide precise information about the Z resonance. The resonance can be described with five parameters: the Z mass m_Z , the Z width Γ_Z , the total hadronic cross-section at the peak, its ratio to the leptonic cross-section and the leptonic forward-backward asymmetry at the peak. Fitting the OPAL data for just these five parameters leads to a precise determination of the Z mass $m_Z = 91.1852 \pm 0.0030 \text{ GeV}$ [39]. However, this fit assumes the contribution to the hadronic cross-section from $\gamma - Z$ interference behaves as predicted by the Standard Model. A more model-independent description of the Z lineshape is provided by the S-matrix approach discussed in this section.

The S-matrix formalism [5] describes the process $e^+e^- \rightarrow Z/\gamma^* \rightarrow f\bar{f}$ assuming only the exchange of a combination of two neutral spin-1 bosons of which one is massless. Contributions from boson exchange and interference are explicitly allowed to vary independently. The resulting parameterizations of the fermion-pair cross-section $\sigma_{\text{tot}}^0(s)$ and asymmetry $A_{\text{fb}}^0(s)$ in lowest order are:

$$\begin{aligned} \sigma_{\text{tot}}^0(s) &= \frac{4}{3}\pi\alpha_{\text{em}}^2 \left[\frac{g_f^{\text{tot}}}{s} + \frac{j_f^{\text{tot}}(s - \overline{m}_Z^2) + r_f^{\text{tot}} s}{(s - \overline{m}_Z^2)^2 + \overline{m}_Z^2 \overline{\Gamma}_Z^2} \right] \\ A_{\text{fb}}^0(s) &= \frac{\pi\alpha_{\text{em}}^2}{\sigma_{\text{tot}}^0} \left[\frac{g_f^{\text{fb}}}{s} + \frac{j_f^{\text{fb}}(s - \overline{m}_Z^2) + r_f^{\text{fb}} s}{(s - \overline{m}_Z^2)^2 + \overline{m}_Z^2 \overline{\Gamma}_Z^2} \right]. \end{aligned} \quad (5)$$

Besides the Z mass \overline{m}_Z and width $\overline{\Gamma}_Z$ there are six parameters per final state fermion f, three for the cross-sections and three for the asymmetries. The photon exchange is described by g_f^{tot} and $g_f^{\text{fb}} (\equiv 0)$ and is assumed to be known. This leaves four parameters, namely r_f^{tot} , r_f^{fb} describing the Z exchange and j_f^{tot} , j_f^{fb} for the interference. For the hadronic final state, the parameters are summed over all colours and open flavours. Since the hadronic asymmetry is not measured, $r_{\text{had}}^{\text{fb}}$ and $j_{\text{had}}^{\text{fb}}$ cannot be determined. The lowest order expressions in Equation (5) serve to introduce the S-matrix parameters, but cannot be used directly to fit the data without the inclusion of large QED radiative corrections. To fit the data, expectations for cross-sections and asymmetries depending on S-matrix parameters including QED radiative corrections were calculated using the program SMATASY [47] together with ZFITTER [6]. These calculations also include very small electroweak corrections to the photon couplings.

In Equation (5) the Z resonance is described with an s -independent width. Usually loop corrections to the Z propagator are absorbed in an s -dependent width via the transformation $\overline{\Gamma}_Z \rightarrow s\Gamma_Z/m_Z^2$. This results in a redefinition of the Z mass and width leading to a numerical

shift of:

$$\begin{aligned}\overline{m}_Z &= m_Z / \sqrt{1 + \Gamma_Z^2/m_Z^2} \approx m_Z - 34 \text{ MeV}, \\ \overline{\Gamma}_Z &= \Gamma_Z / \sqrt{1 + \Gamma_Z^2/m_Z^2} \approx \Gamma_Z - 1 \text{ MeV}.\end{aligned}\quad (6)$$

Although the S-Matrix parameters are \overline{m}_Z and $\overline{\Gamma}_Z$, in this paper the above relations are used to give numerical results for m_Z and Γ_Z to facilitate comparisons with other measurements.

A fit to LEP 1 data alone leaving the parameters describing the interference free leads to a large uncertainty on the Z mass. This is because most LEP 1 data (about 88%) are hadronic events taken at three energy points. This results in effectively three very precise measurements which dominate the determination of the Z properties. From these three measurements the four parameters m_Z , Γ_Z , $r_{\text{had}}^{\text{tot}}$ and $j_{\text{had}}^{\text{tot}}$ cannot be determined simultaneously. The interference increases the cross-sections at energies above the peak and decreases them at lower energies. Therefore a change in this contribution effectively shifts the position of the peak, which can be interpreted as a change in the Z mass. This leads to a strong anti-correlation of 96% between the fit results of $m_Z = 91.1901 \pm 0.0115$ GeV and $j_{\text{had}}^{\text{tot}} = 0.010 \pm 0.650$ from LEP 1 data alone [39].

LEP 2 data provide additional independent measurements to constrain the contribution from interference. Using all OPAL measurements therefore leads to a determination of the Z mass which is less model-dependent than that from the five parameter fit to LEP 1 data, with an error that is only slightly larger. A similar analysis has been performed previously by other experiments [48, 49]. Results presented here supersede the OPAL analysis at lower energies [3].

6.2 Fit Results

To derive results for the S-matrix parameters a fit is performed comparing the predictions with OPAL measurements of fermion-pair production cross-sections and asymmetries at all LEP energies.

The LEP 1 measurements are described in [39]. The results for the hadronic, e^+e^- , $\mu^+\mu^-$ and $\tau^+\tau^-$ cross-sections are given in Tables 8-12 of that paper. Leptonic asymmetries can be found in Tables 22-24. The measurements used in this analysis are those already corrected for the beam energy spread. In the analytical program used to calculate the S-matrix predictions t -channel exchange is not implemented. To use Bhabha cross-sections and asymmetries the t -channel contribution is corrected in the same way as described in [39]. ALIBABA [50] is used to determine the Bhabha forward and backward cross-section for the full $s+t$ -channel and for the s -channel only. During the fit the difference is added to the S-matrix predictions. The t -channel correction is parameterized as a function of $(\sqrt{s} - m_Z)$ and thus depends on the value of the fitted Z mass. The systematic errors and their correlations are taken as described in [39]. The treatment of the errors on the centre-of-mass energy and beam-energy spread is however simplified. For the fits described in [39] the effects of these errors were determined iteratively during the fitting procedure. In this analysis the effect is calculated prior to the fit according to the lineshape determined in [39]. With this simplified error treatment the S-matrix result given in [39] can be reproduced, with deviations of all fit parameters less than 3% of their total error.

The high energy measurements used are the non-radiative cross-sections and asymmetries for hadrons, $\mu^+\mu^-$ and $\tau^+\tau^-$ presented here, together with the corresponding results from

130–183 GeV [2, 3]⁵. Bhabha cross-sections and asymmetries are not included since even with a tight selection⁶ the observed total cross-section, including $s + t$ -channel, is about an order of magnitude larger than the s -channel contribution alone. Correlations between the LEP 2 measurements are taken into account as discussed in Section 5. The systematic errors on the LEP 1 and LEP 2 data are basically uncorrelated. The only common error is the systematic and theoretical error on the luminosity determination. The resulting effect is found to be small and has been neglected.

Expectations for cross-sections and asymmetries depending on S-matrix parameters are calculated using the program SMATASY [47] together with ZFITTER [6]. A χ^2 is calculated between the predictions and the measurements of cross-sections and asymmetries. The results of fits to OPAL data taken at all LEP energies, with and without the assumption of lepton universality, are given in Table 18. The correlation matrices are given in Tables 19 and 20. In principle the results for the S-matrix parameters do not depend on the values of the Standard Model parameters. However, there is a small effect due to the correction from the s -independent width parameters \bar{m}_Z , $\bar{\Gamma}_Z$ to the usual parameters m_Z , Γ_Z since the width Γ_Z depends on the Standard Model parameters. This effect is negligible compared with the overall errors on the fitted parameters. As a cross-check a fit is performed using only the LEP 2 data with the constraint of the S-matrix result given in [39]. This leads to results very similar to the full fit, with differences of all fit parameters being less than 2% of their error.

As can be seen in Table 18 the fitted Z mass gets smaller by 1.0 MeV when lepton universality is imposed. This shift was already observed in a C -parameter fit described in Section 11.1 of [39], although it is larger in the S-matrix fit presented here. It is due to a subtle effect in the Bhabha t -channel correction, which gives an additional weak constraint on m_Z (see [39] Appendix B).

Figure 18 shows the correlation between m_Z and $j_{\text{had}}^{\text{tot}}$ expressed as confidence level contours from fits with lepton universality imposed. Using only LEP 1 data the error on $j_{\text{had}}^{\text{tot}}$ is large with a correlation coefficient of -0.96 to m_Z . Including the LEP 2 data reduces the error on $j_{\text{had}}^{\text{tot}}$ by a factor of five and the correlation is reduced to -0.39 . As a result the error on m_Z is much improved from 11.5 MeV (LEP 1 only) to 3.3 MeV. This is now comparable to the error of 3.0 MeV obtained from the five parameter fit at LEP 1 which assumes the $\gamma - Z$ interference according to the Standard Model. Since the fit result for $j_{\text{had}}^{\text{tot}}$ is close to the Standard Model expectation the central values for m_Z are in good agreement.

7 Limits on New Physics

New physics could be revealed by deviations of the measured data from Standard Model predictions. The generally good agreement seen between data and the Standard Model places severe constraints on the energy scale of such new phenomena. The new data presented here have been combined with previous measurements in order to provide updated limits on four-fermion contact interactions. In addition we present limits on the mass of a possible Z' boson.

⁵At centre-of-mass energies of 161 GeV and 172 GeV the cut is $s'/s > 0.8$.

⁶Acollinearity $\theta_{\text{acol}} < 10^\circ$ and angular range for the electron $|\cos \theta_{e^-}| < 0.7$.

7.1 Limits on Four-fermion Contact Interactions

In the context of composite models of leptons and quarks, a four-fermion contact interaction arises as a remnant of the binding force between the substructure of fermions. Alternatively, a four-fermion contact interaction could be a good description of deviations from the Standard Model due to the exchange of a new very heavy boson of mass m_X if $m_X \gg \sqrt{s}$. More generally, the contact interaction is considered to be a convenient parameterization to describe possible deviations from the Standard Model which may be caused by some unknown new physics.

In this analysis we consider four-fermion contact interactions which conserve flavour and helicity, and in which the $SU(3) \times SU(2) \times U(1)$ gauge structure of the Standard Model is valid. In this framework [51] the Standard Model Lagrangian for $e^+e^- \rightarrow f\bar{f}$ is extended by a term describing a new effective interaction with an unknown coupling constant g and energy scale Λ :

$$\mathcal{L}^{\text{contact}} = \frac{g^2}{(1+\delta)\Lambda^2} \sum_{i,j=L,R} \eta_{ij} [\bar{e}_i \gamma^\mu e_i] [\bar{f}_j \gamma_\mu f_j], \quad (7)$$

where $\delta = 1$ for $e^+e^- \rightarrow e^+e^-$ and $\delta = 0$ otherwise. Here $e_L(f_L)$ and $e_R(f_R)$ are chirality projections of electron (fermion) spinors, and η_{ij} describes the chiral structure of the interaction. The parameters η_{ij} are free in these models, but typical values are between -1 and $+1$, depending on the type of theory assumed [52]. For example, a coupling of two right-handed currents is given by ($\eta_{RR} = \pm 1$, $\eta_{LL} = \eta_{LR} = \eta_{RL} = 0$). Here we consider the same set of models as in [1–3]. The values of η_{ij} which define these models are shown in Table 21.

The inclusion of a contact interaction modifies both the total cross-section and the angular distribution of fermion-pair production. In general, the differential cross-section can be written in terms of a parameter $\varepsilon = (g^2/4\pi)/\Lambda^2$ as

$$\frac{d\sigma}{d \cos \theta} = \sigma_{\text{SM}}(s, t) + C_2^0(s, t)\varepsilon + C_4^0(s, t)\varepsilon^2. \quad (8)$$

Here $t = -s(1 - \cos \theta)/2$ and θ is the polar angle of the outgoing fermion with respect to the e^- beam direction. The C_2^0 term describes the interference between the Standard Model and the contact interaction, the C_4^0 term is the pure contact interaction contribution. The exact form of these terms depends on the type of fermion in the final state and the particular model chosen, and is given, for example, in [53]⁷. The interference term depends linearly on the η_{ij} parameters, and thus can be positive or negative depending on their sign. In fits to the data, the Standard Model cross-sections $\sigma_{\text{SM}}(s, t)$ were calculated using BHWIDE for the e^+e^- final state and ZFITTER for all other final states. Radiative corrections to the lowest order contact interaction terms were taken into account as described in [3].

We have fitted the measurements of the non-radiative cross-sections for $e^+e^- \rightarrow q\bar{q}$, non-radiative cross-sections and asymmetries for $e^+e^- \rightarrow \mu^+\mu^-$ and $e^+e^- \rightarrow \tau^+\tau^-$ and the differential cross-sections for $e^+e^- \rightarrow e^+e^-$ at 189 GeV to 207 GeV presented here, together with the corresponding measurements at 130–183 GeV [2, 3]. In all cases we use a χ^2 fit, including the correlated systematic errors between the measurements and theoretical uncertainties in the Standard Model predictions as discussed in Section 5. Fits are performed with the parameter ε as the fitting parameter. The results for positive and negative interference with the Standard

⁷Equation (2) in [53] has a typographical error: the factor $4s$ on the left-hand side should be replaced by $2s$.

Model (i.e. the sign of the η_{ij} parameters) are equivalent under the transformation $\varepsilon \leftrightarrow -\varepsilon$; it is therefore sufficient to fit only for the case of positive interference but to allow ε to be both positive and negative. Limits on the energy scale Λ were extracted assuming $g^2/4\pi = 1$. The 95% confidence limits correspond to a change in χ^2 of 3.84.

The results are shown in Table 21 and illustrated graphically in Fig. 19. The limits for $q\bar{q}$ are derived from the hadronic cross-sections assuming the new interaction couples to all flavours equally. Those for up-type quarks and down-type quarks are obtained by fitting the hadronic cross-sections assuming the new interaction couples only to one flavour, whereas those for $u\bar{u} + d\bar{d}$ assume a coupling to one generation only. The combined results include all leptonic channels and the hadronic cross-sections. The two sets of values Λ_+ and Λ_- shown in Table 21 correspond to positive and negative values of ε respectively, reflecting the two possible signs of η_{ij} in Equation (7). The data are particularly sensitive to the VV and AA models; the combined data give lower limits on Λ in the range 13–16 TeV for these models. For the other models the lower limits generally lie in the range 9–13 TeV. The limits are typically 1 TeV higher than those for 130–189 GeV data alone [1].

Contact interactions involving quarks have also been studied in ep and pp collisions, where limits comparable to our values are found [54, 55]. Atomic physics parity violation experiments can place higher limits ($\simeq 15$ TeV [56]) on models of eeuu and eedd contact interactions which violate parity.

7.2 Limits on a Z' Boson

7.2.1 Z' Model Predictions

Many theories predict a second heavy neutral vector boson Z'^0 in addition to the Standard Model gauge boson Z^0 . The Z^0 has fermion couplings as predicted by the Standard Model, whereas the axial and vector coupling constants of the Z'^0 to fermions are parameters of the particular model. In general the additional heavy boson Z'^0 will mix with the Z^0 boson. The observed particles are the mass eigenstates Z and Z' [57]:

$$\begin{pmatrix} Z \\ Z' \end{pmatrix} = \begin{pmatrix} \cos \theta_M & \sin \theta_M \\ -\sin \theta_M & \cos \theta_M \end{pmatrix} \begin{pmatrix} Z^0 \\ Z'^0 \end{pmatrix}. \quad (9)$$

The mixing angle θ_M is a free parameter of the model. Here and in the following Z^0 and Z'^0 denote gauge eigenstates whereas the mass eigenstates formed by mixing within the Z' model are denoted as Z and Z' .

In this paper we consider several Z' models. In E6 GUT, the E(6) group may incorporate the Standard Model groups of colour $SU(3)_C$, weak isospin $SU(2)_L$ and hypercharge $U(1)_Y$ in the following way [58]:

$$\begin{aligned} E(6) &\rightarrow SO(10) \times U(1)_\chi \\ SO(10) &\rightarrow SU(5) \times U(1)_\psi \\ SU(5) &\rightarrow SU(3)_C \times SU(2)_L \times U(1)_Y. \end{aligned} \quad (10)$$

Thus the two additional gauge groups $U(1)_\chi$ and $U(1)_\psi$ are introduced, each related to a new gauge boson. In general, the Z'^0 will be a mixed state of these two groups:

$$Z'^0 = Z_\psi \sin \theta_{E6} + Z_\chi \cos \theta_{E6}. \quad (11)$$

We derive limits on the Z' mass and mixing angle for all values of θ_{E6} , with particular emphasis on three special cases: the two no-mixing models χ and ψ ($\theta_{E6} = 0$ and $\pi/2$) and the η model with $\theta_{E6} = -\arctan\sqrt{5/3} = -0.91$. In this latter case the E6 group is broken by a non-Abelian discrete symmetry to a rank-5 group which may occur in superstring theories [58].

Another approach is the left-right symmetric model (LR) [59]. In this scenario a symmetry group $SU(2)_R$ is introduced whose three vector bosons couple to right-handed fermions. The coupling constants of the Z'^0 to fermions depend on one parameter α_{LR} . This can take values $\sqrt{2/3} < \alpha_{LR} < \sqrt{(\cos^2 \theta_W - \sin^2 \theta_W)/\sin^2 \theta_W}$, where θ_W is the weak mixing angle. For $\alpha_{LR} = 1.53$ (the upper limit of the allowed range) left and right-handed coupling constants are approximately the same. For $\alpha_{LR} = \sqrt{2/3}$ the LR model is equivalent to the E6 χ model. We derive limits on the Z' mass and mixing angle as a function of α_{LR} ; of particular interest is the symmetric case of equal left- and right-handed couplings. The axial and vector coupling constants of the Z'^0 to fermions for the E6 and LR models can be found in [58, 60].

In addition to the models described above, we also present limits in the case of a sequential Standard Model (SSM) Z' , which has the same couplings to fermions as the Standard Model Z .

In a more model-independent approach, the Z' can be directly described in terms of its axial and vector couplings to fermions, a'_f and v'_f [61]. At energies far from the Z' resonance, the data are sensitive to the normalized couplings

$$a_f^N \sim a'_f \sqrt{\frac{g^2}{4\pi}} \frac{\sqrt{s}}{m_{Z'}}, \quad v_f^N \sim v'_f \sqrt{\frac{g^2}{4\pi}} \frac{\sqrt{s}}{m_{Z'}}.$$

We present limits on the leptonic couplings, assuming lepton universality and $g^2/4\pi = 1$.

In this analysis, cross-sections and asymmetries predicted by the Z' models are obtained using **ZFITTER** [6] together with **ZEFIT** [60]. Input parameters to the routine are the model parameters: masses of Z and Z' , model angle θ_{E6} or α_{LR} and mixing angle θ_M between Z and Z' . In addition the usual **ZFITTER** input parameters, as described in Section 5, are used. For the Z' mass range relevant here ($300 \leq m_{Z'} \leq 5000$ GeV) the difference between the fitted Z mass within the Standard Model and the mass within the Z' model is less than 1 MeV, well within the experimental uncertainty of the OPAL measurement, $m_Z = 91.1852 \pm 0.0030$ GeV [39]. In the fits described below, m_Z is treated as a free parameter. The parameters α_s , m_{top} and m_{Higgs} are fixed to the values given in Section 5 unless otherwise stated.

7.2.2 Analysis and Results

Cross-sections and asymmetries measured at energies around the Z peak give a precise determination of the properties of the Z boson. If this particle is not the Standard Model Z^0 but a mixture with Z'^0 the couplings to fermions will change. In particular, the measured width of the Z is sensitive to the mixing angle θ_M , and this angle is therefore constrained by the LEP 1 data. At energies above 130 GeV the interference between Z and Z' becomes increasingly important and the data are very sensitive to the mass of the Z' . Since changes to cross-sections and asymmetries arise from interference terms, the precise form of these changes depends strongly on the model.

To obtain limits on the Z' properties, cross-sections for the processes $e^+e^- \rightarrow \mu^+\mu^-, \tau^+\tau^-$, $q\bar{q}$ and the forward-backward asymmetries for the leptonic processes $e^+e^- \rightarrow \mu^+\mu^-, \tau^+\tau^-$ at energies around the Z resonance [39] and the non-radiative values at $\sqrt{s} = 130-183$ GeV [2, 3]

and 189–207 GeV presented here are compared to the predictions of the Z' models. Cross-sections and asymmetries for b- and c-quark production are found to yield negligible additional sensitivity and are not used. In calculating the χ^2 between the predictions of the model and the measurements the correlations of the experimental errors are taken into account as in the S-matrix fit.

A χ^2 between model predictions and the measurements is calculated for different values of the Z' mass and the mixing angle θ_M . The difference between the minimum χ^2 and the Standard Model χ^2 is small for all models, being at most 0.8 for the LR model.

In Fig. 20 we show the 95% confidence level exclusion contours in the $m_{Z'} - \theta_M$ plane for the E6 models χ, ψ, η and the LR model with $\alpha_{LR} = 1.53$. These correspond to $\chi^2 > \chi_{\min}^2 + 5.99$. The limit on the Z' mass depends strongly on the model. The allowed range for the mixing angle is approximately $-2 \text{ mrad} < \theta_M < 3 \text{ mrad}$, and only for the E6 η model is the contour much broader. For very large Z' masses the contours for the different models become similar.

In Fig. 21(a) and (b) we present one-dimensional limits on $m_{Z'}$ and θ_M for a scan over the E6 and LR model angles. The 95% confidence level limits correspond to $\chi^2 > \chi_{\min}^2 + 3.84$. The Standard Model parameters were again fixed. Numerical values of the limits on $m_{Z'}$ and θ_M for parameters corresponding to the χ, ψ, η and symmetric LR models obtained from these one-dimensional fits are given in Table 22, where we also present corresponding limits on the sequential Standard Model Z' .

To assess the effect of fixing the Standard Model parameters, we have also performed fits in which the strong coupling constant and the top quark mass were treated as free parameters, but constrained by their experimental error. The Higgs boson mass was fixed. The sensitivity of the LEP 1 data to m_{Higgs} arises mainly from the Z width, which changes in Z' models. The data cannot discriminate between Z' and Higgs effects, therefore a fit with a free Higgs boson mass would be numerically unstable. Figure 21(c) shows the change in the limit on the mixing angle as a function of model parameters. The limit on the mixing angle obtained with α_s and m_{top} free is typically 10% less restrictive than that obtained when fixing these parameters. Changes to the limits on the Z' mass are at most a few GeV. Since the Higgs boson mass is unknown its influence on the limits has been studied by performing fits with a different fixed mass. Figure 21(d) shows the change in the limit on the mixing angle when the Higgs boson mass is set to 250 GeV rather than its default value of 115 GeV. The change is generally small, but amounts to almost 30% in the region of the E6 η model.

Limits on the vector and axial-vector couplings of a Z' boson to leptons within the model-independent framework were derived with the mixing angle θ_M set to zero. Therefore only the leptonic data at energies of 130 GeV and above were used in the fit, and the Z mass was fixed. The couplings cannot be determined independently from the Z' mass, so we have determined limits for fixed masses of 300, 500 and 1000 GeV. The 95% confidence level limits on the vector and axial-vector couplings, v'_ℓ and a'_ℓ are shown in Fig. 22. The exclusion contours are roughly rectangular in shape. In terms of the normalized couplings, calculated at the luminosity-weighted mean centre-of-mass energy of 193.2 GeV, we find 95% confidence level limits of $|a_\ell^N| < 0.145$ and $|v_\ell^N| < 0.127$.

8 Conclusions

We have presented new measurements of cross-sections and asymmetries for hadronic and lepton-pair production in e^+e^- collisions at centre-of-mass energies between 189 GeV and 209 GeV. At these energies, strong initial-state radiation leads to excitation of the Z. We therefore distinguish two kinematic regions depending on s' , the square of the centre-of-mass energy of the e^+e^- system after initial-state radiation: an ‘inclusive’ region with $s'/s > 0.01$ and a ‘non-radiative’ region with $s'/s > 0.7225$. The results for both inclusive fermion-pair production and for non-radiative events are in good agreement with Standard Model expectations. From these and earlier measurements we derive a value for the electromagnetic coupling constant $1/\alpha_{\text{em}}(193.2 \text{ GeV}) = 127.4^{+2.1}_{-2.0}$. In addition, the results have been used together with OPAL measurements at 91–183 GeV within the S-matrix formalism assuming lepton universality to determine the γ -Z interference term $j_{\text{had}}^{\text{tot}} = 0.144 \pm 0.078$ and to make an almost model-independent measurement of the Z mass, $m_Z = 91.1872 \pm 0.0033 \text{ GeV}$.

The measurements have also been used to place limits on new physics. In the context of a four-fermion contact interaction we have improved the limits on the energy scale Λ from typically 3–13 TeV to 5–16 TeV, assuming $g^2/4\pi = 1$. Lower limits on the mass of a possible Z' boson in the range 334 GeV to 1018 GeV, depending on the model, have been obtained.

Acknowledgements

We particularly wish to thank the SL Division for the efficient operation of the LEP accelerator at all energies and for their close cooperation with our experimental group. In addition to the support staff at our own institutions we are pleased to acknowledge the
Department of Energy, USA,
National Science Foundation, USA,
Particle Physics and Astronomy Research Council, UK,
Natural Sciences and Engineering Research Council, Canada,
Israel Science Foundation, administered by the Israel Academy of Science and Humanities,
Benoziyo Center for High Energy Physics,
Japanese Ministry of Education, Culture, Sports, Science and Technology (MEXT) and a grant under the MEXT International Science Research Program,
Japanese Society for the Promotion of Science (JSPS),
German Israeli Bi-national Science Foundation (GIF),
Bundesministerium für Bildung und Forschung, Germany,
National Research Council of Canada,
Hungarian Foundation for Scientific Research, OTKA T-038240, and T-042864,
The NWO/NATO Fund for Scientific Research, the Netherlands.

References

- [1] OPAL Collab., G. Abbiendi et al., Eur. Phys. J. **C13** (2000) 553.
- [2] OPAL Collab., G. Abbiendi et al., Eur. Phys. J. **C6** (1999) 1.
- [3] OPAL Collab., K. Ackerstaff et al., Eur. Phys. J. **C2** (1998) 441.
- [4] ALEPH Collab., D. Buskulic et al., Phys. Lett. **B378** (1996) 373;
ALEPH Collab., R. Barate et al., Eur. Phys. J. **C12** (2000) 183;
DELPHI Collab., P. Abreu et al., Eur. Phys. J. **C11** (1999) 383;
DELPHI Collab., P. Abreu et al., Phys. Lett. **B485** (2000) 45;
L3 Collab., M. Acciarri et al., Phys. Lett. **B370** (1996) 195;
L3 Collab., M. Acciarri et al., Phys. Lett. **B407** (1997) 361;
L3 Collab., M. Acciarri et al., Phys. Lett. **B414** (1997) 373;
L3 Collab., M. Acciarri et al., Phys. Lett. **B433** (1998) 163;
L3 Collab., M. Acciarri et al., Phys. Lett. **B464** (1999) 135;
L3 Collab., M. Acciarri et al., Phys. Lett. **B470** (1999) 281;
L3 Collab., M. Acciarri et al., Phys. Lett. **B479** (2000) 101;
L3 Collab., M. Acciarri et al., Phys. Lett. **B489** (2000) 81.
- [5] A. Leike, T. Riemann and T. Rose, Phys. Lett. **B273** (1991) 513;
T. Riemann, Phys. Lett. **B293** (1992) 451.
- [6] D. Bardin et al., Comp. Phys. Comm. **133** (2001) 229;
D. Bardin et al., Phys. Lett. **B255** (1991) 290;
D. Bardin et al., Nucl. Phys. **B351** (1991) 1;
D. Bardin et al., Z. Phys. **C44** (1989) 493.
We use ZFITTER version 6.30 with default parameters, except `INTF=0`, `FINR=0`, `BOXD=2`, `CONV=2` and `ALEM=2`, and with the following input parameters: $m_Z=91.1852$ GeV, $m_{\text{top}}=174.3$ GeV, $m_{\text{Higgs}}=115$ GeV, $\Delta\alpha_{\text{had}}^{(5)}=0.02761$, $\alpha_s(m_Z)=0.1185$.
- [7] *Report of the Working Groups on Precision Calculations for LEP2 Physics*, CERN 2000-009, ed. S. Jadach, G. Passarino and R. Pittau, pages 269–378.
- [8] S. Jadach, B.F.L. Ward and Z. Wąs, Phys. Lett. **B449** (1999) 97;
S. Jadach et al., Comp. Phys. Comm. **130** (2000) 260.
- [9] J. Fujimoto et al., Comp. Phys. Comm. **100** (1997) 128.
- [10] S. Jadach et al., Comp. Phys. Comm. **119** (1999) 272.
- [11] OPAL Collab., K. Ahmet et al., Nucl. Instr. and Meth. **A305** (1991) 275.
- [12] S. Anderson et al., Nucl. Instr. and Meth. **A403** (1998) 326.
- [13] M. Arignon et al., Nucl. Instr. and Meth. **A313** (1992) 103;
M. Arignon et al., Nucl. Instr. and Meth. **A333** (1993) 330.
- [14] J.T. Baines et al., Nucl. Instr. and Meth. **A325** (1993) 271;
D.G. Charlton, F. Meijers, T.J. Smith and P.S. Wells, Nucl. Instr. and Meth. **A325** (1993) 129.

- [15] OPAL Collab., G. Abbiendi et al., Eur. Phys. J. **C14** (2000) 373.
- [16] LEP Energy Working Group, *Evaluation of the LEP centre-of-mass energy for data taken in 2000*, LEP Energy Working Group 01/01 (March 2001);
 LEP Energy Working Group, *Evaluation of the LEP centre-of-mass energy for data taken in 1999*, LEP Energy Working Group 00/01 (June 2000);
 LEP Energy Working Group, *Evaluation of the LEP centre-of-mass energy for data taken in 1998*, LEP Energy Working Group 99/01 (March 1998);
 See <http://lepecal.web.cern.ch/LEPECAL/>;
 LEP Energy Working Group, A Blondel et al., Eur. Phys. J. **C11** (1999) 573.
- [17] T. Sjöstrand et al., Comp. Phys. Comm. **135** (2001) 238.
- [18] G. Marchesini et al., Comp. Phys. Comm. **67** (1992) 465;
 G. Corcella et al., JHEP **0101** (2001) 101.
- [19] L. Lönnblad, Comp. Phys. Comm. **71** (1992) 15.
- [20] OPAL Collab., G. Alexander et al., Z. Phys. **C69** (1996) 543;
 OPAL Collab., G. Abbiendi et al., CERN-EP-2003-031, submitted to Eur. Phys. J. **C**.
- [21] S. Jadach, W. Placzek and B.F.L. Ward, Phys. Lett. **B390** (1997) 298.
- [22] S. Jadach, B.F.L. Ward and Z. Wąs, Comput. Phys. Commun. **79** (1994) 503.
- [23] R. Engel and J. Ranft, Phys. Rev. **D54** (1996) 4244.
- [24] A. Buijs et al., Comp. Phys. Comm. **79** (1994) 523.
- [25] OPAL Collab. K. Ackerstaff et al., Z. Phys. **C74** (1997) 33.
- [26] F.A. Berends, P.H. Daverveldt and R. Kleiss, Nucl. Phys. **B253** (1985) 421;
 F.A. Berends, P.H. Daverveldt and R. Kleiss, Comp. Phys. Comm. **40** (1986) 271, 285 and 309.
- [27] J.A.M. Vermaseren, Nucl. Phys. **B229** (1983) 347.
- [28] F.A. Berends and R. Kleiss, Nucl. Phys. **B186** (1981) 22.
- [29] D. Karlen, Nucl. Phys. **B289** (1987) 23.
- [30] J. Allison et al., Nucl. Instr. and Meth. **A317** (1992) 47.
- [31] S. Jadach et al., Comp. Phys. Comm. **102** (1997) 229.
- [32] W. Placzek et al., hep-ph/9903381.
- [33] OPAL Collab., G. Abbiendi et al., Phys. Lett. **B493** (2000) 249.
- [34] S. Catani et al., Phys. Lett. **B269** (1991) 432.
- [35] OPAL Collab., K. Ackerstaff et al., Eur. Phys. J. **C2** (1998) 213.
- [36] OPAL Collab., G. Alexander et al., Phys. Lett. **B376** (1996) 232.

- [37] S. Jadach et al., Comp. Phys. Comm. **140** (2001) 475.
- [38] R.K. Ellis et al., Nucl. Phys. **B178** (1981) 421.
- [39] OPAL Collab., G. Abbiendi et al., Eur. Phys. J. **C19** (2001) 587.
- [40] OPAL Collab., G. Abbiendi et al., Eur. Phys. J. **C26** (2003) 331.
- [41] Particle Data Group, D.E. Groom et al., Eur. Phys. J. **C15** (2000) 1.
- [42] H. Burkhardt and B. Pietrzyk, Phys. Lett. **B513** (2001) 46.
- [43] TOPAZ Collab., I. Levine et al., Phys. Rev. Lett. **78** (1997) 424.
- [44] M. Kobel, *Direct Measurements of the Electromagnetic Coupling Constant at Large q^2* , FREIBURG-EHEP 97-13, Contributed paper to the XVIII International Symposium on Lepton Photon Interactions, Hamburg, July 1997.
- [45] P.J. Mohr and B.N. Taylor, Rev. Mod. Phys. **72** (2000) 351.
- [46] H. Burkhardt and B. Pietrzyk, Phys. Lett. **B356** (1995) 398.
- [47] S. Kirsch and T. Riemann, Comp. Phys. Comm. **88** (1995) 89.
- [48] L3 Collab., M. Acciarri et al., Phys. Lett. **B489** (2000) 93.
- [49] DELPHI Collab., P. Abreu et al., Eur. Phys. J. **C11** (1999) 383.
- [50] W. Beenakker, F.A. Berends and S.C. van der Marck, Nucl. Phys. **B349** (1991) 323.
- [51] E. Eichten, K. Lane and M. Peskin, Phys. Rev. Lett. **50** (1983) 811.
- [52] See for example *Contact interactions and new heavy bosons at HERA: a model independent analysis*, P. Haberl, F. Schrempp and H.U. Martyn, in Proceedings, Physics at HERA, vol. **2**, (1991) 1133.
- [53] OPAL Collab., G. Alexander et al., Phys. Lett. **B387** (1996) 432.
- [54] H1 Collab., C. Adloff et al., Phys. Lett. **B479** (2000) 358;
ZEUS Collab., J. Breitweg et al., Eur. Phys. J. **C14** (2000) 239.
- [55] D0 Collab., B. Abbott et al., Phys. Rev. D Rapid. Comm. **62** (2000) 031101;
CDF Collab., F. Abe et al., Phys. Rev. Lett. **79** (1997) 2198.
- [56] A. Deandrea, Phys. Lett. **B409** (1997) 277.
- [57] G. Altarelli et al., Phys. Lett. **B318** (1993) 139.
- [58] G. Bélanger and S. Godfrey, Phys. Rev. **D35** (1987) 378.
- [59] G. Senjanovic, Nucl. Phys. **B153** (1979) 334.
- [60] A. Leike, S. Riemann and T. Riemann, hep-ph/9808374 (1991);
A. Leike, S. Riemann and T. Riemann, Phys. Lett. **B291** (1992) 187.
- [61] A. Leike, Z. Phys. **C62** (1994) 265.

Interference Corrections $s'/s > 0.01$					
\sqrt{s} / GeV	$\Delta\sigma/\sigma_{\text{SM}}(q\bar{q})$ (%)	$\Delta\sigma/\sigma_{\text{SM}}(\mu\mu)$ (%)	$\Delta\sigma/\sigma_{\text{SM}}(\tau\tau)$ (%)	$\Delta A_{\text{fb}}(\mu\mu)$	$\Delta A_{\text{fb}}(\tau\tau)$
189	+0.04±0.06	-0.63±0.01	-0.47±0.04	-0.0070±0.0002	-0.0057±0.0001
192	+0.04±0.06	-0.63±0.01	-0.49±0.04	-0.0070±0.0002	-0.0058±0.0002
196	+0.05±0.05	-0.64±0.01	-0.47±0.04	-0.0071±0.0002	-0.0058±0.0002
200	+0.06±0.04	-0.65±0.01	-0.48±0.04	-0.0072±0.0002	-0.0059±0.0002
202	+0.06±0.04	-0.65±0.01	-0.51±0.03	-0.0072±0.0002	-0.0061±0.0001
205	+0.07±0.05	-0.65±0.01	-0.51±0.03	-0.0073±0.0002	-0.0060±0.0002
207	+0.08±0.05	-0.65±0.01	-0.50±0.04	-0.0073±0.0002	-0.0061±0.0001
Interference Corrections $s'/s > 0.7225$					
\sqrt{s} / GeV	$\Delta\sigma/\sigma_{\text{SM}}(q\bar{q})$ (%)	$\Delta\sigma/\sigma_{\text{SM}}(\mu\mu)$ (%)	$\Delta\sigma/\sigma_{\text{SM}}(\tau\tau)$ (%)	$\Delta A_{\text{fb}}(\mu\mu)$	$\Delta A_{\text{fb}}(\tau\tau)$
189	+0.14±0.24	-1.46±0.12	-0.95±0.02	-0.0133±0.0015	-0.101±0.0009
192	+0.17±0.21	-1.46±0.12	-0.96±0.02	-0.0135±0.0015	-0.102±0.0009
196	+0.22±0.18	-1.46±0.12	-0.93±0.02	-0.0136±0.0015	-0.101±0.0008
200	+0.27±0.13	-1.46±0.12	-0.94±0.02	-0.0137±0.0015	-0.103±0.0009
202	+0.30±0.11	-1.46±0.12	-0.96±0.02	-0.0137±0.0015	-0.105±0.0009
205	+0.34±0.09	-1.46±0.12	-0.96±0.02	-0.0139±0.0015	-0.105±0.0009
207	+0.37±0.10	-1.46±0.11	-0.95±0.02	-0.0139±0.0015	-0.105±0.0009

Table 1: Corrections $\Delta\sigma$ and ΔA_{fb} which have been applied to the measured cross-sections and asymmetries in order to remove the contribution from interference between initial- and final-state radiation. Cross-section corrections are expressed as a percentage of the expected Standard Model cross-sections, calculated using ZFITTER, while asymmetry corrections are given as absolute numbers.

\sqrt{s} / GeV			$\int \mathcal{L} dt$ / pb $^{-1}$	$\Delta \mathcal{L}/\mathcal{L}$ (%)
nominal	range	mean		
189		188.635 \pm 0.040	185	0.21
192		191.590 \pm 0.042	29	0.32
196		195.526 \pm 0.042	77	0.26
200		199.522 \pm 0.042	79	0.27
202		201.636 \pm 0.042	38	0.30
205	202.5 – 205.5	204.881 \pm 0.050	82	0.26
207	205.5 – 209.0	206.561 \pm 0.050	137	0.24

Table 2: Centre-of-mass energy range, luminosity-weighted mean centre-of-mass energy [16], approximate integrated luminosity collected and total error on the luminosity measurement at each nominal energy point. The precise amount of data used in each analysis varies slightly from channel to channel.

\sqrt{s} / GeV	189	192	196	200	202	205	207
Experimental systematic	0.15	0.20	0.18	0.19	0.19	0.18	0.18
Beam energy	0.04	0.04	0.04	0.04	0.04	0.05	0.05
Theory	0.12	0.12	0.12	0.12	0.12	0.12	0.12
Data statistics	0.09	0.20	0.13	0.13	0.19	0.13	0.10
Total	0.21	0.32	0.26	0.27	0.30	0.26	0.24

Table 3: Errors on the luminosity measurement (in %) at each nominal centre-of-mass energy.

Efficiencies and backgrounds at $\sqrt{s} = 189$ GeV				
Channel		Efficiency (%)	Background / pb	Feedthrough / pb
q̄q	$s'/s > 0.01$	86.6 ± 0.3	6.1 ± 0.7	—
	$s'/s > 0.7225$	87.0 ± 0.3	1.55 ± 0.06	0.959 ± 0.043
$\mu^+\mu^-$	$s'/s > 0.01$	74.7 ± 0.8	0.42 ± 0.02	—
	$s'/s > 0.7225$	87.9 ± 0.9	0.058 ± 0.006	0.044 ± 0.005
$\tau^+\tau^-$	$s'/s > 0.01$	33.8 ± 0.8	0.32 ± 0.03	—
	$s'/s > 0.7225$	48.4 ± 1.2	0.123 ± 0.014	0.055 ± 0.003
e^+e^-	A: $ \cos \theta_{e^\pm} < 0.9, \theta_{\text{acol}} < 170^\circ$	97.5 ± 0.4	1.8 ± 0.3	—
	B: $ \cos \theta_{e^-} < 0.7, \theta_{\text{acol}} < 10^\circ$	99.0 ± 0.3	0.25 ± 0.03	—
	C: $ \cos \theta_{e^\pm} < 0.96, \theta_{\text{acol}} < 10^\circ$	98.5 ± 0.4	10.4 ± 0.5	—
Efficiencies and backgrounds at $\sqrt{s} = 192$ GeV				
Channel		Efficiency (%)	Background / pb	Feedthrough / pb
q̄q	$s'/s > 0.01$	85.9 ± 0.3	6.2 ± 0.7	—
	$s'/s > 0.7225$	86.7 ± 0.3	1.54 ± 0.06	0.972 ± 0.044
$\mu^+\mu^-$	$s'/s > 0.01$	74.4 ± 0.8	0.43 ± 0.02	—
	$s'/s > 0.7225$	87.9 ± 0.9	0.062 ± 0.005	0.042 ± 0.004
$\tau^+\tau^-$	$s'/s > 0.01$	33.6 ± 0.8	0.31 ± 0.03	—
	$s'/s > 0.7225$	48.4 ± 1.2	0.121 ± 0.013	0.052 ± 0.003
e^+e^-	A: $ \cos \theta_{e^\pm} < 0.9, \theta_{\text{acol}} < 170^\circ$	97.5 ± 0.4	1.7 ± 0.3	—
	B: $ \cos \theta_{e^-} < 0.7, \theta_{\text{acol}} < 10^\circ$	98.9 ± 0.3	0.24 ± 0.02	—
	C: $ \cos \theta_{e^\pm} < 0.96, \theta_{\text{acol}} < 10^\circ$	98.5 ± 0.4	10.0 ± 0.5	—
Efficiencies and backgrounds at $\sqrt{s} = 196$ GeV				
Channel		Efficiency (%)	Background / pb	Feedthrough / pb
q̄q	$s'/s > 0.01$	85.1 ± 0.3	6.2 ± 0.7	—
	$s'/s > 0.7225$	86.2 ± 0.3	1.52 ± 0.06	0.868 ± 0.039
$\mu^+\mu^-$	$s'/s > 0.01$	74.0 ± 0.8	0.45 ± 0.02	—
	$s'/s > 0.7225$	87.9 ± 0.9	0.068 ± 0.005	0.040 ± 0.004
$\tau^+\tau^-$	$s'/s > 0.01$	33.3 ± 0.8	0.31 ± 0.03	—
	$s'/s > 0.7225$	48.4 ± 1.1	0.118 ± 0.012	0.049 ± 0.003
e^+e^-	A: $ \cos \theta_{e^\pm} < 0.9, \theta_{\text{acol}} < 170^\circ$	97.4 ± 0.4	1.7 ± 0.2	—
	B: $ \cos \theta_{e^-} < 0.7, \theta_{\text{acol}} < 10^\circ$	98.9 ± 0.3	0.23 ± 0.02	—
	C: $ \cos \theta_{e^\pm} < 0.96, \theta_{\text{acol}} < 10^\circ$	98.5 ± 0.4	9.7 ± 0.5	—

Table 4: Efficiency of selection cuts, accepted background, and feedthrough of events generated with lower s' into the non-radiative samples, for each channel at each energy. The (very small) contribution of events with $s'/s < 0.01$ to the inclusive sample is included in the efficiency. The errors include Monte Carlo statistics and systematic effects. In the case of electron pairs, the efficiencies are effective values including the efficiency of selection cuts for events within the acceptance region and the effect of acceptance corrections. An acceptance of $|\cos \theta_{e^\pm}| < 0.9$ (or 0.96) means that both electron and positron must satisfy this cut, whereas $|\cos \theta_{e^-}| < 0.7$ means that only the electron need do so.

Efficiencies and backgrounds at $\sqrt{s} = 200$ GeV				
Channel		Efficiency (%)	Background / pb	Feedthrough / pb
$q\bar{q}$	$s'/s > 0.01$	84.2 ± 0.4	6.2 ± 0.6	—
	$s'/s > 0.7225$	85.8 ± 0.3	1.50 ± 0.06	0.832 ± 0.037
$\mu^+\mu^-$	$s'/s > 0.01$	73.7 ± 0.8	0.47 ± 0.02	—
	$s'/s > 0.7225$	87.9 ± 0.9	0.073 ± 0.005	0.038 ± 0.004
$\tau^+\tau^-$	$s'/s > 0.01$	32.9 ± 0.8	0.30 ± 0.02	—
	$s'/s > 0.7225$	48.4 ± 1.1	0.115 ± 0.011	0.045 ± 0.002
e^+e^-	A: $ \cos \theta_{e^\pm} < 0.9, \theta_{\text{acol}} < 170^\circ$	97.4 ± 0.4	1.6 ± 0.3	—
	B: $ \cos \theta_{e^-} < 0.7, \theta_{\text{acol}} < 10^\circ$	98.9 ± 0.3	0.22 ± 0.02	—
	C: $ \cos \theta_{e^\pm} < 0.96, \theta_{\text{acol}} < 10^\circ$	98.4 ± 0.4	9.3 ± 0.5	—
Efficiencies and backgrounds at $\sqrt{s} = 202$ GeV				
Channel		Efficiency (%)	Background / pb	Feedthrough / pb
$q\bar{q}$	$s'/s > 0.01$	83.8 ± 0.4	6.2 ± 0.6	—
	$s'/s > 0.7225$	85.6 ± 0.3	1.49 ± 0.06	0.819 ± 0.036
$\mu^+\mu^-$	$s'/s > 0.01$	73.5 ± 0.8	0.47 ± 0.02	—
	$s'/s > 0.7225$	87.9 ± 0.9	0.076 ± 0.005	0.037 ± 0.004
$\tau^+\tau^-$	$s'/s > 0.01$	32.8 ± 0.8	0.29 ± 0.02	—
	$s'/s > 0.7225$	48.4 ± 1.1	0.114 ± 0.011	0.043 ± 0.002
e^+e^-	A: $ \cos \theta_{e^\pm} < 0.9, \theta_{\text{acol}} < 170^\circ$	97.4 ± 0.4	1.6 ± 0.3	—
	B: $ \cos \theta_{e^-} < 0.7, \theta_{\text{acol}} < 10^\circ$	98.9 ± 0.3	0.22 ± 0.02	—
	C: $ \cos \theta_{e^\pm} < 0.96, \theta_{\text{acol}} < 10^\circ$	98.4 ± 0.4	9.1 ± 0.5	—
Efficiencies and backgrounds at $\sqrt{s} = 205$ GeV				
Channel		Efficiency (%)	Background / pb	Feedthrough / pb
$q\bar{q}$	$s'/s > 0.01$	83.1 ± 0.4	6.3 ± 0.6	—
	$s'/s > 0.7225$	85.2 ± 0.3	1.48 ± 0.05	0.805 ± 0.036
$\mu^+\mu^-$	$s'/s > 0.01$	73.2 ± 0.8	0.49 ± 0.02	—
	$s'/s > 0.7225$	87.9 ± 0.9	0.080 ± 0.006	0.035 ± 0.004
$\tau^+\tau^-$	$s'/s > 0.01$	32.5 ± 0.8	0.29 ± 0.02	—
	$s'/s > 0.7225$	48.4 ± 1.1	0.111 ± 0.010	0.040 ± 0.002
e^+e^-	A: $ \cos \theta_{e^\pm} < 0.9, \theta_{\text{acol}} < 170^\circ$	97.2 ± 0.5	1.5 ± 0.3	—
	B: $ \cos \theta_{e^-} < 0.7, \theta_{\text{acol}} < 10^\circ$	98.8 ± 0.4	0.21 ± 0.02	—
	C: $ \cos \theta_{e^\pm} < 0.96, \theta_{\text{acol}} < 10^\circ$	98.4 ± 0.4	8.8 ± 0.4	—
Efficiencies and backgrounds at $\sqrt{s} = 207$ GeV				
Channel		Efficiency (%)	Background / pb	Feedthrough / pb
$q\bar{q}$	$s'/s > 0.01$	82.7 ± 0.4	6.3 ± 0.6	—
	$s'/s > 0.7225$	85.0 ± 0.3	1.47 ± 0.05	0.746 ± 0.033
$\mu^+\mu^-$	$s'/s > 0.01$	73.0 ± 0.8	0.50 ± 0.03	—
	$s'/s > 0.7225$	87.9 ± 0.9	0.082 ± 0.006	0.034 ± 0.003
$\tau^+\tau^-$	$s'/s > 0.01$	32.4 ± 0.8	0.28 ± 0.02	—
	$s'/s > 0.7225$	48.4 ± 1.1	0.110 ± 0.011	0.039 ± 0.002
e^+e^-	A: $ \cos \theta_{e^\pm} < 0.9, \theta_{\text{acol}} < 170^\circ$	97.2 ± 0.5	1.5 ± 0.3	—
	B: $ \cos \theta_{e^-} < 0.7, \theta_{\text{acol}} < 10^\circ$	98.8 ± 0.4	0.21 ± 0.02	—
	C: $ \cos \theta_{e^\pm} < 0.96, \theta_{\text{acol}} < 10^\circ$	98.4 ± 0.4	8.7 ± 0.4	—

Table 4: Continued

Cross-sections at $\sqrt{s} = 189$ GeV				
Channel	$\int \mathcal{L} dt / pb^{-1}$	Events	σ / pb	σ^{SM} / pb
$q\bar{q}$	$s'/s > 0.01$	185.9	17146	$99.5 \pm 0.8 \pm 0.9$
			4019	$22.0 \pm 0.4 \pm 0.1$
$\mu^+\mu^-$	$s'/s > 0.01$	178.6	1128	$7.85 \pm 0.25 \pm 0.09$
			519	$3.14 \pm 0.15 \pm 0.03$
$\tau^+\tau^-$	$s'/s > 0.01$	179.0	554	$8.17 \pm 0.39 \pm 0.21$
			333	$3.45 \pm 0.21 \pm 0.09$
e^+e^-	A: $ \cos \theta_{e^\pm} < 0.9, \theta_{acol} < 170^\circ$	185.9	20538	$111.5 \pm 0.8 \pm 0.6$
	B: $ \cos \theta_{e^-} < 0.7, \theta_{acol} < 10^\circ$		3758	$20.2 \pm 0.3 \pm 0.1$
	C: $ \cos \theta_{e^\pm} < 0.96, \theta_{acol} < 10^\circ$		57669	$304.4 \pm 1.3 \pm 1.5$
Cross-sections at $\sqrt{s} = 192$ GeV				
Channel	$\int \mathcal{L} dt / pb^{-1}$	Events	σ / pb	σ^{SM} / pb
$q\bar{q}$	$s'/s > 0.01$	29.6	2617	$95.9 \pm 2.0 \pm 0.9$
			643	$22.2 \pm 0.9 \pm 0.1$
$\mu^+\mu^-$	$s'/s > 0.01$	29.0	173	$7.40 \pm 0.61 \pm 0.09$
			77	$2.86 \pm 0.34 \pm 0.03$
$\tau^+\tau^-$	$s'/s > 0.01$	29.1	85	$7.74 \pm 0.95 \pm 0.20$
			50	$3.17 \pm 0.50 \pm 0.08$
e^+e^-	A: $ \cos \theta_{e^\pm} < 0.9, \theta_{acol} < 170^\circ$	29.5	3084	$105.6 \pm 1.9 \pm 0.6$
	B: $ \cos \theta_{e^-} < 0.7, \theta_{acol} < 10^\circ$		577	$19.5 \pm 0.8 \pm 0.1$
	C: $ \cos \theta_{e^\pm} < 0.96, \theta_{acol} < 10^\circ$		9034	$301.0 \pm 3.3 \pm 1.6$
Cross-sections at $\sqrt{s} = 196$ GeV				
Channel	$\int \mathcal{L} dt / pb^{-1}$	Events	σ / pb	σ^{SM} / pb
$q\bar{q}$	$s'/s > 0.01$	77.8	6351	$88.8 \pm 1.2 \pm 0.9$
			1509	$19.8 \pm 0.6 \pm 0.1$
$\mu^+\mu^-$	$s'/s > 0.01$	76.0	435	$7.08 \pm 0.37 \pm 0.08$
			207	$2.93 \pm 0.22 \pm 0.03$
$\tau^+\tau^-$	$s'/s > 0.01$	75.9	206	$7.21 \pm 0.57 \pm 0.19$
			120	$2.89 \pm 0.30 \pm 0.07$
e^+e^-	A: $ \cos \theta_{e^\pm} < 0.9, \theta_{acol} < 170^\circ$	77.7	7879	$102.3 \pm 1.2 \pm 0.5$
	B: $ \cos \theta_{e^-} < 0.7, \theta_{acol} < 10^\circ$		1448	$18.6 \pm 0.5 \pm 0.1$
	C: $ \cos \theta_{e^\pm} < 0.96, \theta_{acol} < 10^\circ$		22618	$285.7 \pm 2.0 \pm 1.5$

Table 5: Measured cross-sections, integrated luminosity used in the analysis and numbers of selected events at each energy. For the cross-sections, the first error shown is statistical, the second systematic. As in [3], the cross-sections for hadrons, $\mu^+\mu^-$ and $\tau^+\tau^-$ are defined to cover phase-space up to the limit imposed by the s'/s cut, with $\sqrt{s'}$ defined as the invariant mass of the outgoing two-fermion system *before* final-state radiation. The contribution of interference between initial- and final-state radiation has been removed. The last column shows the Standard Model cross-section predictions from ZFITTER [6] (hadrons, $\mu^+\mu^-$, $\tau^+\tau^-$) and BHWIDE [21] (e^+e^-).

Cross-sections at $\sqrt{s} = 200$ GeV				
Channel	$\int \mathcal{L} dt / pb^{-1}$	Events	σ / pb	σ^{SM} / pb
$q\bar{q}$	$s'/s > 0.01$	79.4	6100	$83.9 \pm 1.2 \pm 0.9$
			1468	$18.9 \pm 0.5 \pm 0.1$
$\mu^+\mu^-$	$s'/s > 0.01$	78.2	423	$6.67 \pm 0.36 \pm 0.08$
			202	$2.77 \pm 0.21 \pm 0.03$
$\tau^+\tau^-$	$s'/s > 0.01$	78.0	205	$7.04 \pm 0.56 \pm 0.18$
			132	$3.14 \pm 0.30 \pm 0.08$
e^+e^-	A: $ \cos \theta_{e^\pm} < 0.9, \theta_{acol} < 170^\circ$	79.4	7819	$99.5 \pm 1.1 \pm 0.5$
	B: $ \cos \theta_{e^-} < 0.7, \theta_{acol} < 10^\circ$		1444	$18.2 \pm 0.5 \pm 0.1$
	C: $ \cos \theta_{e^\pm} < 0.96, \theta_{acol} < 10^\circ$		22046	$272.8 \pm 1.9 \pm 1.4$
Cross-sections at $\sqrt{s} = 202$ GeV				
Channel	$\int \mathcal{L} dt / pb^{-1}$	Events	σ / pb	σ^{SM} / pb
$q\bar{q}$	$s'/s > 0.01$	38.2	2898	$83.2 \pm 1.7 \pm 0.9$
			692	$18.5 \pm 0.8 \pm 0.1$
$\mu^+\mu^-$	$s'/s > 0.01$	36.8	171	$5.63 \pm 0.48 \pm 0.07$
			82	$2.36 \pm 0.28 \pm 0.03$
$\tau^+\tau^-$	$s'/s > 0.01$	36.9	104	$7.69 \pm 0.84 \pm 0.20$
			59	$2.95 \pm 0.43 \pm 0.07$
e^+e^-	A: $ \cos \theta_{e^\pm} < 0.9, \theta_{acol} < 170^\circ$	38.2	3697	$97.8 \pm 1.6 \pm 0.5$
	B: $ \cos \theta_{e^-} < 0.7, \theta_{acol} < 10^\circ$		682	$17.8 \pm 0.7 \pm 0.1$
	C: $ \cos \theta_{e^\pm} < 0.96, \theta_{acol} < 10^\circ$		10551	$271.7 \pm 2.7 \pm 1.4$
Cross-sections at $\sqrt{s} = 205$ GeV				
Channel	$\int \mathcal{L} dt / pb^{-1}$	Events	σ / pb	σ^{SM} / pb
$q\bar{q}$	$s'/s > 0.01$	82.3	6094	$81.7 \pm 1.1 \pm 0.9$
			1458	$18.2 \pm 0.5 \pm 0.1$
$\mu^+\mu^-$	$s'/s > 0.01$	78.9	418	$6.53 \pm 0.35 \pm 0.08$
			212	$2.88 \pm 0.21 \pm 0.03$
$\tau^+\tau^-$	$s'/s > 0.01$	78.9	199	$6.84 \pm 0.55 \pm 0.18$
			117	$2.72 \pm 0.28 \pm 0.07$
e^+e^-	A: $ \cos \theta_{e^\pm} < 0.9, \theta_{acol} < 170^\circ$	82.3	7613	$93.6 \pm 1.1 \pm 0.6$
	B: $ \cos \theta_{e^-} < 0.7, \theta_{acol} < 10^\circ$		1433	$17.4 \pm 0.5 \pm 0.1$
	C: $ \cos \theta_{e^\pm} < 0.96, \theta_{acol} < 10^\circ$		21916	$261.8 \pm 1.8 \pm 1.3$
Cross-sections at $\sqrt{s} = 207$ GeV				
Channel	$\int \mathcal{L} dt / pb^{-1}$	Events	σ / pb	σ^{SM} / pb
$q\bar{q}$	$s'/s > 0.01$	137.4	9686	$77.7 \pm 0.9 \pm 0.8$
			2260	$16.8 \pm 0.4 \pm 0.1$
$\mu^+\mu^-$	$s'/s > 0.01$	134.4	739	$6.81 \pm 0.28 \pm 0.08$
			347	$2.77 \pm 0.16 \pm 0.03$
$\tau^+\tau^-$	$s'/s > 0.01$	134.5	318	$6.39 \pm 0.41 \pm 0.17$
			203	$2.78 \pm 0.22 \pm 0.07$
e^+e^-	A: $ \cos \theta_{e^\pm} < 0.9, \theta_{acol} < 170^\circ$	137.7	12335	$90.6 \pm 0.8 \pm 0.6$
	B: $ \cos \theta_{e^-} < 0.7, \theta_{acol} < 10^\circ$		2320	$16.9 \pm 0.4 \pm 0.1$
	C: $ \cos \theta_{e^\pm} < 0.96, \theta_{acol} < 10^\circ$		35997	$257.1 \pm 1.4 \pm 1.3$

Table 5: Continued

Asymmetries at $\sqrt{s} = 189$ GeV				
	N_f	N_b	A_{fb}	A_{fb}^{SM}
$\mu^+\mu^-$	$s'/s > 0.01$	733	395	$0.252 \pm 0.030 \pm 0.006$
	$s'/s > 0.7225$	399.5	119.5	$0.548 \pm 0.039 \pm 0.005$
$\tau^+\tau^-$	$s'/s > 0.01$	373	170	$0.304 \pm 0.046 \pm 0.008$
	$s'/s > 0.7225$	253.5	73.5	$0.591 \pm 0.054 \pm 0.012$
e^+e^-	$ \cos \theta_{e^-} < 0.7$ and $\theta_{\text{acol}} < 10^\circ$	3332	354	$0.811 \pm 0.010 \pm 0.004$
Asymmetries at $\sqrt{s} = 192$ GeV				
	N_f	N_b	A_{fb}	A_{fb}^{SM}
$\mu^+\mu^-$	$s'/s > 0.01$	100	73	$0.095 \pm 0.080 \pm 0.006$
	$s'/s > 0.7225$	52	25	$0.341 \pm 0.115 \pm 0.005$
$\tau^+\tau^-$	$s'/s > 0.01$	62	21	$0.444 \pm 0.111 \pm 0.008$
	$s'/s > 0.7225$	42.5	6.5	$0.813 \pm 0.109 \pm 0.013$
e^+e^-	$ \cos \theta_{e^-} < 0.7$ and $\theta_{\text{acol}} < 10^\circ$	518	46	$0.841 \pm 0.023 \pm 0.004$
Asymmetries at $\sqrt{s} = 196$ GeV				
	N_f	N_b	A_{fb}	A_{fb}^{SM}
$\mu^+\mu^-$	$s'/s > 0.01$	305.5	129.5	$0.358 \pm 0.048 \pm 0.005$
	$s'/s > 0.7225$	172.5	34.5	$0.683 \pm 0.055 \pm 0.005$
$\tau^+\tau^-$	$s'/s > 0.01$	125.5	72.5	$0.175 \pm 0.077 \pm 0.008$
	$s'/s > 0.7225$	78	36	$0.373 \pm 0.103 \pm 0.013$
e^+e^-	$ \cos \theta_{e^-} < 0.7$ and $\theta_{\text{acol}} < 10^\circ$	1276	137	$0.810 \pm 0.016 \pm 0.004$

Table 6: Measured asymmetry values and numbers of forward (N_f) and backward (N_b) events at each energy. The measured asymmetry values include corrections for background and efficiency, and in the case of $\mu^+\mu^-$ and $\tau^+\tau^-$ are corrected to the full solid angle with interference between initial- and final-state radiation subtracted. The first error shown is statistical, the second systematic. The final column shows the Standard Model predictions of BHWIDE for e^+e^- and ZFITTER for the other final states.

Asymmetries at $\sqrt{s} = 200$ GeV				
	N_f	N_b	A_{fb}	A_{fb}^{SM}
$\mu^+\mu^-$	$s'/s > 0.01$	294.5	128.5	$0.346 \pm 0.049 \pm 0.005$
	$s'/s > 0.7225$	164	38	$0.637 \pm 0.059 \pm 0.005$
$\tau^+\tau^-$	$s'/s > 0.01$	142	59	$0.341 \pm 0.074 \pm 0.005$
	$s'/s > 0.7225$	107	23	$0.700 \pm 0.077 \pm 0.009$
e^+e^-	$ \cos \theta_{e^-} < 0.7$ and $\theta_{\text{acol}} < 10^\circ$	1290	142	$0.805 \pm 0.016 \pm 0.004$
Asymmetries at $\sqrt{s} = 202$ GeV				
	N_f	N_b	A_{fb}	A_{fb}^{SM}
$\mu^+\mu^-$	$s'/s > 0.01$	114	57	$0.277 \pm 0.080 \pm 0.006$
	$s'/s > 0.7225$	61	21	$0.489 \pm 0.104 \pm 0.005$
$\tau^+\tau^-$	$s'/s > 0.01$	67	36	$0.205 \pm 0.105 \pm 0.006$
	$s'/s > 0.7225$	42.5	16.5	$0.440 \pm 0.138 \pm 0.011$
e^+e^-	$ \cos \theta_{e^-} < 0.7$ and $\theta_{\text{acol}} < 10^\circ$	595	69	$0.795 \pm 0.024 \pm 0.004$
Asymmetries at $\sqrt{s} = 205$ GeV				
	N_f	N_b	A_{fb}	A_{fb}^{SM}
$\mu^+\mu^-$	$s'/s > 0.01$	270	148	$0.234 \pm 0.051 \pm 0.006$
	$s'/s > 0.7225$	160	52	$0.512 \pm 0.063 \pm 0.005$
$\tau^+\tau^-$	$s'/s > 0.01$	133	58	$0.317 \pm 0.076 \pm 0.006$
	$s'/s > 0.7225$	87	26	$0.575 \pm 0.092 \pm 0.011$
e^+e^-	$ \cos \theta_{e^-} < 0.7$ and $\theta_{\text{acol}} < 10^\circ$	1248	147	$0.792 \pm 0.016 \pm 0.004$
Asymmetries at $\sqrt{s} = 207$ GeV				
	N_f	N_b	A_{fb}	A_{fb}^{SM}
$\mu^+\mu^-$	$s'/s > 0.01$	488	251	$0.264 \pm 0.038 \pm 0.006$
	$s'/s > 0.7225$	261	86	$0.508 \pm 0.050 \pm 0.005$
$\tau^+\tau^-$	$s'/s > 0.01$	205	105	$0.230 \pm 0.061 \pm 0.007$
	$s'/s > 0.7225$	142	53	$0.472 \pm 0.075 \pm 0.011$
e^+e^-	$ \cos \theta_{e^-} < 0.7$ and $\theta_{\text{acol}} < 10^\circ$	2062	216	$0.814 \pm 0.012 \pm 0.004$

Table 6: Continued

$q\bar{q}$							
$ \cos \theta $	$d\sigma/d \cos \theta / \text{pb}$						
	189 GeV	192 GeV	196 GeV	200 GeV	202 GeV	205 GeV	207 GeV
[0.0, 0.1]	17.4±1.0	20.8±2.8	16.4±1.5	11.8±1.3	13.6±2.0	12.3±1.3	13.0±1.0
[0.1, 0.2]	17.9±1.0	14.6±2.4	14.4±1.5	15.8±1.5	16.1±2.2	12.8±1.4	13.4±1.1
[0.2, 0.3]	17.8±1.0	18.1±2.6	14.4±1.5	11.9±1.3	15.4±2.2	12.6±1.4	10.7±1.0
[0.3, 0.4]	18.3±1.1	17.6±2.6	16.1±1.6	16.2±1.5	20.5±2.5	15.8±1.5	16.6±1.2
[0.4, 0.5]	18.6±1.1	23.6±3.0	19.2±1.7	17.4±1.6	16.3±2.2	16.5±1.5	15.0±1.1
[0.5, 0.6]	21.3±1.1	23.2±3.0	20.5±1.7	18.0±1.6	14.4±2.1	19.1±1.6	17.1±1.2
[0.6, 0.7]	24.8±1.2	23.1±3.0	23.4±1.8	20.8±1.7	18.6±2.4	20.4±1.7	18.9±1.3
[0.7, 0.8]	25.8±1.2	23.8±3.0	21.3±1.7	21.4±1.7	21.1±2.5	22.4±1.7	17.6±1.2
[0.8, 0.9]	26.6±1.3	29.1±3.3	23.0±1.8	27.6±2.0	23.4±2.6	21.7±1.7	20.9±1.3
[0.9, 1.0]	31.0±1.7	26.2±4.0	28.9±2.6	27.7±2.5	25.3±3.4	28.4±2.5	24.7±1.8

Table 7: Differential cross-sections for $q\bar{q}$ production. The values are for $s'/s > 0.7225$ and are corrected to no interference between initial- and final-state radiation. Errors are statistical only; systematic errors are given in Table 11.

$\mu^+ \mu^-$							
$\cos \theta$	$d\sigma/d\cos \theta / \text{pb}$						
	189 GeV	192 GeV	196 GeV	200 GeV	202 GeV	205 GeV	207 GeV
[-1.0, -0.8]	$0.67 \pm^{0.32}_{0.25}$	$1.3 \pm^{1.3}_{0.8}$	$0.19 \pm^{0.39}_{0.19}$	$0.31 \pm^{0.45}_{0.28}$	$1.0 \pm^{1.0}_{0.7}$	$0.76 \pm^{0.58}_{0.42}$	$0.44 \pm^{0.34}_{0.25}$
[-0.8, -0.6]	$0.47 \pm^{0.18}_{0.14}$	$0.7 \pm^{0.7}_{0.4}$	$0.28 \pm^{0.26}_{0.16}$	$0.17 \pm^{0.23}_{0.13}$	$0.1 \pm^{0.4}_{0.1}$	$0.43 \pm^{0.30}_{0.20}$	$0.49 \pm^{0.22}_{0.17}$
[-0.6, -0.4]	$0.54 \pm^{0.20}_{0.16}$	$0.4 \pm^{0.6}_{0.3}$	$0.79 \pm^{0.38}_{0.29}$	$0.56 \pm^{0.34}_{0.24}$	$0.3 \pm^{0.5}_{0.2}$	$0.72 \pm^{0.35}_{0.26}$	$0.72 \pm^{0.26}_{0.20}$
[-0.4, -0.2]	0.62 ± 0.13	$0.5 \pm^{0.6}_{0.3}$	$0.54 \pm^{0.32}_{0.23}$	$0.60 \pm^{0.33}_{0.24}$	$0.5 \pm^{0.5}_{0.3}$	$0.60 \pm^{0.33}_{0.24}$	$0.70 \pm^{0.25}_{0.20}$
[-0.2, 0.0]	1.27 ± 0.19	$1.9 \pm^{0.8}_{0.6}$	$0.54 \pm^{0.30}_{0.21}$	0.9 ± 0.3	$1.2 \pm^{0.6}_{0.5}$	$1.0 \pm^{0.4}_{0.3}$	1.01 ± 0.20
[0.0, 0.2]	1.35 ± 0.20	$0.8 \pm^{0.6}_{0.4}$	1.7 ± 0.3	1.3 ± 0.3	$0.9 \pm^{0.6}_{0.4}$	1.5 ± 0.3	0.86 ± 0.19
[0.2, 0.4]	2.03 ± 0.25	$2.0 \pm^{0.9}_{0.7}$	1.6 ± 0.3	1.9 ± 0.4	$0.8 \pm^{0.6}_{0.4}$	2.2 ± 0.4	1.7 ± 0.3
[0.4, 0.6]	2.15 ± 0.26	$1.9 \pm^{0.9}_{0.7}$	2.2 ± 0.4	1.6 ± 0.3	$1.4 \pm^{0.7}_{0.5}$	1.8 ± 0.4	2.0 ± 0.3
[0.6, 0.8]	2.85 ± 0.30	$2.7 \pm^{1.0}_{0.8}$	3.0 ± 0.5	2.8 ± 0.5	$2.8 \pm^{0.7}_{0.7}$	2.2 ± 0.4	2.6 ± 0.3
[0.8, 1.0]	3.77 ± 0.42	$1.9 \pm^{1.3}_{0.9}$	3.9 ± 0.6	3.8 ± 0.6	$3.0 \pm^{1.2}_{1.0}$	3.2 ± 0.6	3.3 ± 0.5

Table 8: Differential cross-sections for $\mu^+ \mu^-$ production. The values are for $s'/s > 0.7225$ and are corrected to no interference between initial- and final-state radiation. Errors are statistical only; systematic errors are given in Table 11.

$\tau^+\tau^-$							
$\cos\theta$	$d\sigma/d\cos\theta / \text{pb}$						
	189 GeV	192 GeV	189 GeV	200 GeV	202 GeV	205 GeV	207 GeV
[−1.0, −0.8]	$1.1 \pm^{1.0}_{0.8}$	$-0.1 \pm^{1.6}_{0.0}$	$1.3 \pm^{1.9}_{1.2}$	$0.4 \pm^{1.4}_{0.7}$	$2.5 \pm^{4.0}_{2.6}$	$-0.1 \pm^{0.6}_{0.0}$	$0.2 \pm^{0.9}_{0.4}$
[−0.8, −0.6]	$0.2 \pm^{0.3}_{0.2}$	$-0.1 \pm^{0.5}_{0.0}$	$1.0 \pm^{0.7}_{0.5}$	$0.0 \pm^{0.4}_{0.1}$	$0.3 \pm^{1.0}_{0.5}$	$0.7 \pm^{0.6}_{0.4}$	$0.8 \pm^{0.5}_{0.3}$
[−0.6, −0.4]	$0.9 \pm^{0.4}_{0.3}$	$0.9 \pm^{1.3}_{0.7}$	$0.7 \pm^{0.6}_{0.4}$	$0.5 \pm^{0.6}_{0.4}$	$0.6 \pm^{1.0}_{0.6}$	$1.1 \pm^{0.7}_{0.5}$	$0.7 \pm^{0.4}_{0.3}$
[−0.4, −0.2]	$0.8 \pm^{0.4}_{0.3}$	$0.4 \pm^{1.1}_{0.6}$	$0.9 \pm^{0.7}_{0.5}$	$0.8 \pm^{0.6}_{0.5}$	$1.2 \pm^{1.2}_{0.8}$	$0.4 \pm^{0.6}_{0.4}$	$0.5 \pm^{0.4}_{0.3}$
[−0.2, 0.0]	$0.8 \pm^{0.4}_{0.3}$	$0.5 \pm^{1.1}_{0.5}$	$0.8 \pm^{0.6}_{0.5}$	$0.7 \pm^{0.6}_{0.4}$	$0.5 \pm^{1.0}_{0.6}$	$0.4 \pm^{0.6}_{0.4}$	$1.2 \pm^{0.5}_{0.4}$
[0.0, 0.2]	1.6 ± 0.3	$1.7 \pm^{1.4}_{0.9}$	$1.1 \pm^{0.7}_{0.5}$	$1.5 \pm^{0.8}_{0.6}$	$0.9 \pm^{1.1}_{0.6}$	$1.2 \pm^{0.7}_{0.5}$	1.2 ± 0.3
[0.2, 0.4]	2.0 ± 0.3	$1.8 \pm^{1.5}_{1.0}$	$1.3 \pm^{0.7}_{0.5}$	2.1 ± 0.5	$1.2 \pm^{1.1}_{0.7}$	$1.6 \pm^{0.7}_{0.6}$	1.4 ± 0.3
[0.4, 0.6]	2.7 ± 0.4	$1.9 \pm^{1.4}_{1.0}$	$2.0 \pm^{0.8}_{0.6}$	2.4 ± 0.5	$2.9 \pm^{1.4}_{1.1}$	$1.9 \pm^{0.7}_{0.6}$	2.6 ± 0.4
[0.6, 0.8]	3.1 ± 0.5	$3.7 \pm^{1.8}_{1.4}$	1.9 ± 0.5	3.4 ± 0.7	$2.9 \pm^{1.4}_{1.1}$	2.5 ± 0.6	2.0 ± 0.4
[0.8, 1.0]	4.7 ± 0.8	$6.4 \pm^{4.3}_{3.1}$	$4.1 \pm^{2.0}_{1.6}$	$3.8 \pm^{2.0}_{1.6}$	$3.0 \pm^{3.0}_{2.0}$	$3.7 \pm^{2.0}_{1.5}$	$2.5 \pm^{1.2}_{1.0}$

Table 9: Differential cross-sections for $\tau^+\tau^-$ production. The values are for $s'/s > 0.7225$ and are corrected to no interference between initial- and final-state radiation. Errors are statistical only; systematic errors are given in Table 11.

e^+e^-							
$\cos \theta$	$d\sigma/d\cos \theta / \text{pb}$						
	189 GeV	192 GeV	196 GeV	200 GeV	202 GeV	205 GeV	207 GeV
[-0.90, -0.72]	1.3±0.2	1.4± ^{0.7} _{0.5}	1.3± ^{0.4} _{0.3}	1.5±0.3	2.2± ^{0.7} _{0.6}	0.8± ^{0.3} _{0.2}	1.4±0.2
[-0.72, -0.54]	2.1±0.3	2.5± ^{0.9} _{0.7}	1.5±0.3	1.8±0.4	1.3± ^{0.6} _{0.4}	1.7±0.4	1.7±0.3
[-0.54, -0.36]	2.4±0.3	1.5± ^{0.8} _{0.5}	2.2±0.4	2.0±0.4	2.8± ^{0.8} _{0.7}	2.3±0.4	1.7±0.3
[-0.36, -0.18]	2.5±0.3	2.4± ^{0.9} _{0.7}	2.9±0.5	2.5±0.4	3.8±0.8	2.3±0.4	2.8±0.3
[-0.18, 0.00]	3.8±0.4	2.9± ^{1.0} _{0.8}	3.5±0.5	3.9±0.5	2.2± ^{0.8} _{0.6}	3.8±0.5	2.8±0.4
[0.00, 0.09]	4.5±0.5	6.5± ^{2.0} _{1.6}	5.1±0.9	5.1±0.9	5.0± ^{1.6} _{1.2}	5.7±0.9	3.9±0.6
[0.09, 0.18]	6.3±0.6	6.6± ^{2.1} _{1.6}	5.6±0.9	6.2±1.0	8.2±1.6	6.9±1.0	6.4±0.7
[0.18, 0.27]	9.2±0.8	9.2±1.9	8.4±1.1	9.7±1.2	8.9±1.6	7.2±1.0	7.4±0.8
[0.27, 0.36]	12.3±0.9	13.7±2.3	12.7±1.4	10.0±1.2	10.8±1.8	11.2±1.3	11.9±1.0
[0.36, 0.45]	19.7±1.1	21.2±2.9	14.9±1.5	15.6±1.5	14.6±2.1	14.2±1.4	17.1±1.2
[0.45, 0.54]	31.9±1.4	31.0±3.5	26.7±2.0	28.8±2.1	24.5±2.7	27.2±2.0	25.1±1.5
[0.54, 0.63]	51.6±1.8	45.2±4.3	50.1±2.8	48.4±2.7	45.4±3.8	43.8±2.5	41.9±1.9
[0.63, 0.72]	94.9±2.4	91.6±5.9	90.5±3.6	87.1±3.5	84.4±5.0	79.0±3.3	77.3±2.5
[0.72, 0.81]	215±4	206±9	199±6	194±5	184±8	173±5	174±4
[0.81, 0.90]	684±7	663±16	640±10	606±10	606±14	578±9	565±7

Table 10: Differential cross-sections for e^+e^- production for $\theta_{\text{acol}} < 10^\circ$. Errors are statistical only; systematic errors are given in Table 11.

\sqrt{s} / GeV		189	192	196	200	202	205	207
q̄q	$s'/s > 0.01$	0.90	0.92	0.97	1.00	1.00	1.00	1.04
	$s'/s > 0.7225$	0.57	0.54	0.53	0.52	0.52	0.51	0.54
$\mu^+\mu^-$	$s'/s > 0.01$	1.12	1.13	1.13	1.14	1.19	1.17	1.16
	$s'/s > 0.7225$	1.08	1.08	1.07	1.07	1.08	1.08	1.08
$\tau^+\tau^-$	$s'/s > 0.01$	2.6	2.6	2.6	2.6	2.5	2.6	2.6
	$s'/s > 0.7225$	2.5	2.5	2.5	2.5	2.5	2.5	2.5
e^+e^-	A: $ \cos\theta_{e^\pm} < 0.9, \theta_{\text{acol}} < 170^\circ$	0.51	0.46	0.46	0.46	0.46	0.59	0.59
	B: $ \cos\theta_{e^-} < 0.7, \theta_{\text{acol}} < 10^\circ$	0.31	0.36	0.36	0.36	0.36	0.39	0.39
	C: $ \cos\theta_{e^\pm} < 0.96, \theta_{\text{acol}} < 10^\circ$	0.44	0.43	0.43	0.43	0.43	0.44	0.44
e^+e^-	D: $-0.9 < \cos\theta_{e^-} < -0.7, \theta_{\text{acol}} < 10^\circ$	1.10	1.16	1.16	1.16	1.16	1.18	1.18
	D: $ \cos\theta_{e^-} < 0.7, \theta_{\text{acol}} < 10^\circ$	0.47	0.50	0.50	0.50	0.50	0.52	0.52
	D: $0.7 < \cos\theta_{e^-} < 0.9, \theta_{\text{acol}} < 10^\circ$	0.77	0.86	0.86	0.86	0.86	0.89	0.89

Table 11: Total systematic errors, in %, excluding those on the luminosity measurement, for each channel at each nominal centre-of-mass energy. For the e^+e^- final state, the first three rows refer to the total cross-section measurements, while the last three refer to the differential cross-section, for which extra cuts are applied. For the hadronic, $\mu^+\mu^-$ and $\tau^+\tau^-$ final states, the values given for $s'/s > 0.7225$ apply to both the total cross-section and the differential cross-section.

q̄q		
	$s'/s > 0.01$	$s'/s > 0.7225$
MC statistics (efficiency)	0.03	0.06
MC statistics (background)	0.03	0.04
ISR modelling	0.12	0.02
Fragmentation modelling	0.37	0.26
Detector effects	0.19	0.15
s' determination	0.03	0.19
W^+W^- rejection cuts	0.07	0.13
W^+W^- background	0.21	0.26
Other background	0.87	0.19
Interference	0.04	0.13
Total	1.00	0.52

Table 12: Systematic errors, in %, on the hadronic cross-section measurements at 200 GeV. Values at other energies are very similar, the total errors are given in Table 11. Errors on the luminosity measurement are given in Table 3.

$\mu^+ \mu^-$		
	$s'/s > 0.01$	$s'/s > 0.7225$
MC statistics (efficiency)	0.08	0.08
MC statistics (background)	0.10	0.08
MC statistics (feedthrough)	–	0.03
Efficiency	1.00	1.00
ISR modelling	0.20	0.07
Feedthrough	–	0.16
Cosmic background	0.20	0.20
Other background	0.46	0.20
Interference	0.01	0.12
Total	1.14	1.07

Table 13: Systematic errors, in %, on the $\mu^+ \mu^-$ cross-section measurements at 200 GeV. The errors at other energies are very similar, the totals at each energy are given in Table 11. Errors on the luminosity measurement are given in Table 3.

$\tau^+ \tau^-$		
	$s'/s > 0.01$	$s'/s > 0.7225$
MC statistics (efficiency)	0.19	0.21
MC statistics (background)	0.22	0.20
MC statistics (feedthrough)	–	0.05
Efficiency	2.34	2.34
ISR	0.20	0.04
Feedthrough	–	0.15
Background	0.99	0.69
Interference	0.04	0.01
Total	2.6	2.5

Table 14: Systematic errors, in %, on the $\tau^+ \tau^-$ cross-section measurements at 200 GeV. The errors at other energies are very similar, the totals at each energy are given in Table 11. Errors on the luminosity measurement are given in Table 3.

e^+e^-			
	A $ \cos\theta_{e^\pm} < 0.9$ $\theta_{acol} < 170^\circ$	B $ \cos\theta_{e^-} < 0.7$ $\theta_{acol} < 10^\circ$	C $ \cos\theta_{e^\pm} < 0.96$ $\theta_{acol} < 10^\circ$
MC statistics	0.02	0.04	0.02
4-fermion correction	0.06	—	—
Multiplicity cuts	0.09	0.04	0.03
Calorimeter energy scale/resolution	0.01	< 0.01	0.08
Two track requirement	0.32	0.30	—
Acceptance	0.19	0.14	0.39
Background	0.25	0.13	0.17
Total	0.46	0.36	0.43
	D $-0.9 < \cos\theta_{e^-} < -0.7$ $\theta_{acol} < 10^\circ$	D $ \cos\theta_{e^-} < 0.7$ $\theta_{acol} < 10^\circ$	D $+0.7 < \cos\theta_{e^-} < +0.9$ $\theta_{acol} < 10^\circ$
Multiplicity cuts	0.05	0.04	0.05
Calorimeter energy scale/resolution	0.01	0.01	0.01
Two track requirement	0.48	0.30	0.48
Opposite charge requirement	0.64	0.37	0.64
Charge misassignment	0.50	—	—
Acceptance	0.30	0.10	0.30
Background	0.60	0.11	0.02
Total	1.16	0.50	0.86

Table 15: Systematic errors, in %, on the e^+e^- cross-section and angular distribution measurements at 200 GeV. Values at other energies are very similar, the totals at each energy are given in Table 11. Errors on the luminosity measurement are given in Table 3. In the case of the angular distribution, acceptance D, the errors arising from Monte Carlo statistics are included in the statistical errors given in Table 10.

		Standard Model $\chi^2 / \text{d.o.f}$	Data / Standard Model	
			Mean	$\chi^2 / \text{d.o.f}$
$\sigma(\text{q}\bar{\text{q}})$	$s'/s > 0.01$	5.9/7	0.997 ± 0.010	5.8/6
	$s'/s > 0.7225$	5.0/7	0.990 ± 0.011	4.2/6
$\sigma(\mu^+ \mu^-)$	$s'/s > 0.01$	9.8/7	1.012 ± 0.021	9.5/6
	$s'/s > 0.7225$	4.7/7	0.994 ± 0.028	4.6/6
$A_{\text{fb}}(\mu^+ \mu^-)$	$s'/s > 0.01$	11.6/7	0.975 ± 0.065	11.5/6
	$s'/s > 0.7225$	12.3/7	0.999 ± 0.040	12.3/6
$\sigma(\tau^+ \tau^-)$	$s'/s > 0.01$	2.6/7	1.045 ± 0.039	1.3/6
	$s'/s > 0.7225$	2.4/7	1.052 ± 0.044	1.1/6
$A_{\text{fb}}(\tau^+ \tau^-)$	$s'/s > 0.01$	6.3/7	1.015 ± 0.096	6.2/6
	$s'/s > 0.7225$	13.8/7	1.033 ± 0.057	13.5/6
$\sigma(\ell^+ \ell^-)$	$s'/s > 0.01$	12.4/14	1.020 ± 0.019	11.3/13
	$s'/s > 0.7225$	7.1/14	1.010 ± 0.024	6.9/13
$A_{\text{fb}}(\ell^+ \ell^-)$	$s'/s > 0.01$	17.9/14	0.988 ± 0.054	17.9/13
	$s'/s > 0.7225$	26.2/14	1.010 ± 0.033	26.1/13

Table 16: Comparison of measurements with Standard Model predictions. The first column gives the χ^2 value of the measured cross-sections or asymmetry values at 189–207 GeV presented here with respect to the Standard Model predictions. The second and third columns give the results of fits to the mean ratios of data to Standard Model predictions. Values for $\ell^+ \ell^-$ are for $\mu^+ \mu^-$ and $\tau^+ \tau^-$ together.

\sqrt{s} / GeV	Using cross-sections				Using ratios			
	Fit		Standard Model		Fit		Standard Model	
	$1/\alpha_{\text{em}}$	$\chi^2/\text{d.o.f.}$	$1/\alpha_{\text{em}}$	$\chi^2/\text{d.o.f.}$	$1/\alpha_{\text{em}}$	$\chi^2/\text{d.o.f.}$	$1/\alpha_{\text{em}}$	$\chi^2/\text{d.o.f.}$
188.6	127.1 ± 3.8	2.0/4	127.9	2.0/5	126.2 ± 4.2	1.7/3	127.9	1.9/4
191.6	134.9 ± 16.5	10.0/4	127.9	10.4/5	138.1 ± 14.3	9.1/3	127.9	10.0/4
195.5	131.2 ± 6.9	8.4/4	127.9	8.7/5	129.9 ± 7.6	8.1/3	127.9	8.2/4
199.5	130.3 ± 7.2	6.4/4	127.8	6.6/5	130.3 ± 8.0	6.4/3	127.8	6.5/4
201.6	134.1 ± 11.5	2.8/4	127.8	3.3/5	134.0 ± 12.2	2.8/3	127.8	3.1/4
204.9	122.1 ± 5.5	0.7/4	127.8	1.8/5	123.7 ± 6.8	0.6/3	127.8	0.9/4
206.6	123.4 ± 4.0	4.6/4	127.8	5.7/5	117.9 ± 4.7	0.6/3	127.8	4.5/4
193.2	127.4 ± 2.1	59.1/59	127.9	59.1/60	126.7 ± 2.4	50.4/47	127.9	50.7/48

Table 17: Results of fits for α_{em} . The first seven rows show the fits to data at each energy, the last row the combined fit to these data and measurements at 130–183 GeV [2, 3]. The Standard Model values of $1/\alpha_{\text{em}}$, and the χ^2 between the measurements and the Standard Model predictions are also given for comparison. Results are shown for the fits using cross-sections, and also for the fits to cross-section ratios, as discussed in the text.

Parameter	Without lepton universality	With lepton universality	Standard Model prediction
m_Z / GeV	91.1882 ± 0.0033	91.1872 ± 0.0033	—
Γ_Z / GeV	2.4945 ± 0.0041	2.4943 ± 0.0041	$2.4960^{+0.0016}_{-0.0029}$
$r_{\text{had}}^{\text{tot}}$	2.963 ± 0.009	2.963 ± 0.009	$2.9650^{+0.0037}_{-0.0066}$
$j_{\text{had}}^{\text{tot}}$	0.131 ± 0.078	0.144 ± 0.078	$0.2213^{+0.0027}_{-0.0059}$
r_e^{tot}	0.14134 ± 0.00069		
r_μ^{tot}	0.14215 ± 0.00056		
r_τ^{tot}	0.14228 ± 0.00074		
r_ℓ^{tot}		0.14199 ± 0.00050	$0.14270^{+0.00016}_{-0.00027}$
j_e^{tot}	-0.080 ± 0.044		
j_μ^{tot}	-0.008 ± 0.019		
j_τ^{tot}	-0.004 ± 0.025		
j_ℓ^{tot}		-0.014 ± 0.015	$0.00439^{+0.00010}_{-0.00022}$
r_e^{fb}	0.00138 ± 0.00084		
r_μ^{fb}	0.00270 ± 0.00043		
r_τ^{fb}	0.00248 ± 0.00057		
r_ℓ^{fb}		0.00243 ± 0.00032	$0.00280^{+0.00007}_{-0.00016}$
j_e^{fb}	0.763 ± 0.070		
j_μ^{fb}	0.758 ± 0.024		
j_τ^{fb}	0.788 ± 0.030		
j_ℓ^{fb}		0.767 ± 0.018	$0.7987^{+0.0005}_{-0.0006}$
$\chi^2/\text{d.o.f.}$	$207.0 / 247$	$213.3 / 255$	

Table 18: Results from the fit to all LEP 1 and LEP 2 data for the S-matrix parameters with and without the assumption of lepton universality. The last column gives the Standard Model predictions. An S-matrix fit to only LEP 1 data without lepton universality gives a χ^2 of 146.6 with 187 d.o.f. [39].

Parameter	1	2	3	4	5	6	7	8	9	10	11	12	13	14	15	16
1 m_Z	1.00	0.04	0.06	-0.40	-0.08	0.04	0.03	-0.11	-0.12	-0.11	-0.06	0.07	0.06	0.01	-0.04	-0.03
2 Γ_Z	0.04	1.00	0.92	-0.08	0.57	0.71	0.54	-0.03	0.01	0.02	0.00	0.02	0.01	0.00	0.04	0.04
3 $r_{\text{had}}^{\text{tot}}$	0.06	0.92	1.00	-0.09	0.57	0.71	0.54	-0.04	0.00	0.01	0.01	0.02	0.02	0.00	0.04	0.04
4 $j_{\text{had}}^{\text{tot}}$	-0.40	-0.08	-0.09	1.00	0.00	-0.07	-0.05	0.08	0.09	0.08	0.03	-0.04	-0.03	0.00	0.03	0.02
5 r_e^{tot}	-0.08	0.57	0.57	0.00	1.00	0.45	0.33	0.03	0.02	0.02	0.17	-0.01	-0.01	-0.02	0.03	0.03
6 r_μ^{tot}	0.04	0.71	0.71	-0.07	0.45	1.00	0.41	-0.03	0.08	0.01	0.01	0.03	0.01	0.00	0.09	0.03
7 r_τ^{tot}	0.03	0.54	0.54	-0.05	0.33	0.41	1.00	-0.02	0.00	0.09	0.00	0.01	0.03	0.00	0.03	0.10
8 j_e^{tot}	-0.11	-0.03	-0.04	0.08	0.03	-0.03	-0.02	1.00	0.02	0.02	0.00	-0.01	-0.01	0.24	0.01	0.00
9 j_μ^{tot}	-0.12	0.01	0.00	0.09	0.02	0.08	0.00	0.02	1.00	0.03	0.01	0.06	-0.01	0.00	0.33	0.01
10 j_τ^{tot}	-0.11	0.02	0.01	0.08	0.02	0.01	0.09	0.02	0.03	1.00	0.01	-0.01	0.06	0.00	0.01	0.29
11 r_e^{fb}	-0.06	0.00	0.01	0.03	0.17	0.01	0.00	0.00	0.01	0.01	1.00	-0.01	-0.01	0.06	0.00	0.00
12 r_μ^{fb}	0.07	0.02	0.02	-0.04	-0.01	0.03	0.01	-0.01	0.06	-0.01	-0.01	1.00	0.02	0.00	0.12	0.00
13 r_τ^{fb}	0.06	0.01	0.02	-0.03	-0.01	0.01	0.03	-0.01	-0.01	0.06	-0.01	0.02	1.00	0.00	0.00	0.12
14 j_e^{fb}	0.01	0.00	0.00	0.00	-0.02	0.00	0.00	0.24	0.00	0.00	0.06	0.00	0.00	1.00	0.00	0.00
15 j_μ^{fb}	-0.04	0.04	0.04	0.03	0.03	0.09	0.03	0.01	0.33	0.01	0.00	0.12	0.00	0.00	1.00	0.02
16 j_τ^{fb}	-0.03	0.04	0.04	0.02	0.03	0.03	0.10	0.00	0.01	0.29	0.00	0.00	0.12	0.00	0.02	1.00

Table 19: Error correlation matrix for the S-matrix fit without lepton universality.

Parameter	1	2	3	4	5	6	7	8
1 m_Z	1.00	0.04	0.06	-0.39	0.01	-0.19	0.07	-0.06
2 Γ_Z	0.04	1.00	0.92	-0.08	0.80	0.00	0.02	0.06
3 $r_{\text{had}}^{\text{tot}}$	0.06	0.92	1.00	-0.09	0.80	-0.01	0.03	0.05
4 $j_{\text{had}}^{\text{tot}}$	-0.39	-0.08	-0.09	1.00	-0.06	0.14	-0.03	0.04
5 r_{ℓ}^{tot}	0.01	0.80	0.80	-0.06	1.00	0.06	0.05	0.09
6 j_{ℓ}^{tot}	-0.19	0.00	-0.01	0.14	0.06	1.00	0.05	0.31
7 r_{ℓ}^{fb}	0.07	0.02	0.03	-0.03	0.05	0.05	1.00	0.11
8 j_{ℓ}^{fb}	-0.06	0.06	0.05	0.04	0.09	0.31	0.11	1.00

Table 20: Error correlation matrix for the S-matrix fit assuming lepton universality.

Channel	LL [$\pm 1, 0, 0, 0$]	RR [$0, \pm 1, 0, 0$]	LR [$0, 0, \pm 1, 0$]	RL [$0, 0, 0, \pm 1$]	VV [$\pm 1, \pm 1, \pm 1, \pm 1$]	AA [$\pm 1, \pm 1, \mp 1, \mp 1$]	LL+RR [$\pm 1, \pm 1, 0, 0$]	LR+RL [$0, 0, \pm 1, \pm 1$]	$\bar{\mathcal{O}}_{\text{DB}}$ [$\pm \frac{1}{4}, \pm 1, \pm \frac{1}{2}, \pm \frac{1}{2}$]
e^+e^-	ε_0 4.7 Λ_+ Λ_-	$0.009^{+0.018}_{-0.017}$ 8.1 $0.009^{+0.019}_{-0.017}$ 6.1	$0.009^{+0.019}_{-0.017}$ 4.7 $-0.009^{+0.010}_{-0.009}$ 6.0	$-0.009^{+0.010}_{-0.009}$ 8.1 $0.002^{+0.012}_{-0.013}$ 6.2	$-0.009^{+0.010}_{-0.009}$ 8.1 $0.002^{+0.012}_{-0.013}$ 6.2	$-0.002^{+0.004}_{-0.004}$ 12.6 $0.000^{+0.003}_{-0.003}$ 10.6	$0.006^{+0.005}_{-0.005}$ 8.1 $-0.001^{+0.004}_{-0.004}$ 11.9	$0.004^{+0.009}_{-0.008}$ 6.8 $-0.001^{+0.004}_{-0.004}$ 8.5	$-0.005^{+0.005}_{-0.005}$ 11.8 $0.001^{+0.006}_{-0.006}$ 8.6
	$\mu^+\mu^-$ Λ_+ Λ_-	$-0.002^{+0.009}_{-0.009}$ 8.1 $-0.002^{+0.009}_{-0.009}$ 7.3	$0.002^{+0.012}_{-0.013}$ 6.3 $0.002^{+0.012}_{-0.013}$ 6.3	$0.002^{+0.012}_{-0.013}$ 6.3 $0.002^{+0.018}_{-0.020}$ 6.3	$0.000^{+0.003}_{-0.003}$ 12.7 $0.004^{+0.005}_{-0.005}$ 12.4	$-0.001^{+0.004}_{-0.004}$ 11.3 $0.008^{+0.007}_{-0.007}$ 10.2	$0.001^{+0.004}_{-0.004}$ 11.1 $0.008^{+0.007}_{-0.007}$ 10.1	$0.000^{+0.006}_{-0.006}$ 8.7 $-0.001^{+0.009}_{-0.010}$ 9.3	$0.000^{+0.006}_{-0.006}$ 9.2 $0.007^{+0.009}_{-0.009}$ 9.2
	$\tau^+\tau^-$ Λ_+ Λ_-	$0.015^{+0.013}_{-0.014}$ 4.9 $0.017^{+0.014}_{-0.015}$ 7.2	$0.017^{+0.014}_{-0.015}$ 4.7 $-0.002^{+0.018}_{-0.020}$ 6.9	$-0.002^{+0.018}_{-0.020}$ 5.7 $0.004^{+0.005}_{-0.005}$ 4.6	$-0.002^{+0.018}_{-0.020}$ 5.7 $0.004^{+0.005}_{-0.005}$ 4.6	$0.008^{+0.007}_{-0.007}$ 8.6 $0.008^{+0.007}_{-0.007}$ 11.1	$0.008^{+0.007}_{-0.007}$ 6.7 $0.008^{+0.007}_{-0.007}$ 10.7	$-0.001^{+0.009}_{-0.010}$ 7.8 $0.007^{+0.009}_{-0.009}$ 10.0	$0.007^{+0.009}_{-0.009}$ 6.4 $0.007^{+0.009}_{-0.009}$ 8.4
$\ell^+\ell^-$	ε_0 Λ_+ Λ_-	$0.004^{+0.007}_{-0.007}$ 7.7 $0.004^{+0.007}_{-0.007}$ 9.5	$0.004^{+0.007}_{-0.007}$ 7.4 $-0.005^{+0.007}_{-0.007}$ 9.3	$-0.005^{+0.007}_{-0.007}$ 9.3 $-0.005^{+0.007}_{-0.007}$ 7.3	$0.000^{+0.002}_{-0.002}$ 15.2 $0.003^{+0.003}_{-0.003}$ 15.1	$0.003^{+0.003}_{-0.003}$ 10.5 $0.002^{+0.004}_{-0.004}$ 15.4	$0.002^{+0.004}_{-0.004}$ 10.6 $-0.002^{+0.004}_{-0.004}$ 13.3	$0.000^{+0.004}_{-0.004}$ 13.2 $0.000^{+0.004}_{-0.004}$ 10.3	$0.000^{+0.004}_{-0.004}$ 11.2 $0.000^{+0.004}_{-0.004}$ 11.4
	$q\bar{q}$ Λ_+ Λ_-	$-0.021^{+0.021}_{-0.038}$ 8.2 $0.018^{+0.023}_{-0.022}$ 3.7	$0.018^{+0.023}_{-0.022}$ 4.3 $0.007^{+0.020}_{-0.020}$ 7.0	$0.007^{+0.020}_{-0.020}$ 4.9 $0.011^{+0.013}_{-0.010}$ 6.1	$0.011^{+0.013}_{-0.010}$ 3.1 $0.011^{+0.012}_{-0.012}$ 9.3	$-0.009^{+0.009}_{-0.025}$ 5.7 $-0.009^{+0.009}_{-0.025}$ 10.4	$-0.007^{+0.014}_{-0.014}$ 12.0 $0.010^{+0.045}_{-0.009}$ 5.0	$0.010^{+0.045}_{-0.009}$ 7.5 $0.011^{+0.052}_{-0.010}$ 5.7	$0.011^{+0.052}_{-0.010}$ 3.9 $0.011^{+0.052}_{-0.010}$ 10.3
	combined Λ_+ Λ_-	$0.001^{+0.006}_{-0.006}$ 9.2 $0.006^{+0.007}_{-0.007}$ 9.4	$0.006^{+0.007}_{-0.007}$ 7.2 $-0.003^{+0.007}_{-0.007}$ 10.1	$0.001^{+0.006}_{-0.005}$ 9.4 $0.001^{+0.006}_{-0.005}$ 7.8	$0.000^{+0.002}_{-0.002}$ 9.0 $0.001^{+0.003}_{-0.003}$ 10.1	$0.001^{+0.003}_{-0.003}$ 14.7 $0.002^{+0.003}_{-0.003}$ 16.2	$0.002^{+0.003}_{-0.003}$ 12.6 $0.001^{+0.003}_{-0.003}$ 14.9	$-0.001^{+0.003}_{-0.003}$ 11.1 $0.001^{+0.003}_{-0.003}$ 13.2	$0.002^{+0.004}_{-0.004}$ 12.9 $0.002^{+0.004}_{-0.004}$ 12.3
$u\bar{u}$	ε_0 Λ_+ Λ_-	$0.009^{+0.009}_{-0.009}$ 5.9 $0.014^{+0.015}_{-0.013}$ 9.1	$0.014^{+0.015}_{-0.013}$ 4.8 $0.048^{+0.095}_{-0.047}$ 7.7	$0.048^{+0.095}_{-0.047}$ 2.4 $0.018^{+0.045}_{-0.044}$ 5.4	$0.018^{+0.045}_{-0.044}$ 3.3 $0.005^{+0.005}_{-0.004}$ 4.1	$0.005^{+0.005}_{-0.004}$ 8.5 $0.007^{+0.008}_{-0.007}$ 13.0	$0.007^{+0.008}_{-0.007}$ 6.7 $0.006^{+0.005}_{-0.005}$ 10.7	$0.038^{+0.052}_{-0.038}$ 7.8 $0.009^{+0.009}_{-0.009}$ 11.8	$0.009^{+0.009}_{-0.009}$ 3.0 $0.009^{+0.009}_{-0.009}$ 6.2
	$d\bar{d}$ Λ_+ Λ_-	$-0.011^{+0.011}_{-0.011}$ 8.6 $-0.033^{+0.032}_{-0.140}$ 5.5	$-0.033^{+0.032}_{-0.140}$ 6.0 $-0.036^{+0.047}_{-0.049}$ 2.2	$-0.036^{+0.047}_{-0.049}$ 4.6 $0.045^{+0.092}_{-0.043}$ 2.9	$0.045^{+0.092}_{-0.043}$ 2.4 $-0.009^{+0.009}_{-0.010}$ 5.4	$-0.009^{+0.009}_{-0.010}$ 9.9 $-0.007^{+0.007}_{-0.008}$ 5.6	$-0.007^{+0.007}_{-0.008}$ 10.9 $-0.008^{+0.008}_{-0.008}$ 6.7	$0.019^{+0.032}_{-0.032}$ 10.2 $0.019^{+0.032}_{-0.032}$ 6.5	$-0.034^{+0.033}_{-0.085}$ 3.7 $-0.034^{+0.033}_{-0.085}$ 5.2
	$u\bar{u} + d\bar{d}$ Λ_+ Λ_-	$0.018^{+0.032}_{-0.032}$ 3.7 $0.040^{+0.050}_{-0.039}$ 5.1	$0.040^{+0.050}_{-0.039}$ 3.0 $0.018^{+0.032}_{-0.032}$ 6.2	$0.018^{+0.032}_{-0.032}$ 3.7 $0.039^{+0.051}_{-0.039}$ 5.2	$0.039^{+0.051}_{-0.039}$ 3.0 $0.011^{+0.050}_{-0.011}$ 6.2	$0.011^{+0.050}_{-0.011}$ 3.8 $0.000^{+0.015}_{-0.016}$ 9.7	$0.000^{+0.015}_{-0.016}$ 6.1 $0.028^{+0.035}_{-0.027}$ 6.1	$0.027^{+0.035}_{-0.027}$ 3.6 $0.016^{+0.025}_{-0.015}$ 7.3	$0.016^{+0.025}_{-0.015}$ 2.8 $0.016^{+0.025}_{-0.015}$ 7.9

Table 21: Results of the contact interaction fits to the non-radiative hadron and lepton-pair data. The numbers in square brackets are the values of $[\eta_{\text{LL}}, \eta_{\text{RR}}, \eta_{\text{LR}}, \eta_{\text{RL}}]$ which define the models. ε_0 is the fitted value of $\varepsilon = 1/\Lambda^2$, Λ_\pm are the 95% confidence level limits; the values for Λ_+ and Λ_- correspond to the upper and lower signs, respectively, of the η_{ij} values. The units of Λ are TeV, those of ε_0 are TeV^{-2} .

Model:	χ	ψ	η	LR	SSM
$m_{Z'}^{\text{low}} / \text{GeV}$	781	366	515	518	1018
$\theta_M^{\text{up}} / \text{mrad}$	1.94	2.58	3.31	1.90	0.91
$\theta_M^{\text{low}} / \text{mrad}$	-0.99	-1.29	-4.47	-0.98	-4.22

Table 22: One-dimensional limits at 95% confidence level on the Z' mass, $m_{Z'}^{\text{low}}$, and the mixing angle, θ_M^{up} and θ_M^{low} , for various Z' models. The Z mass is free during the fit and the other three Standard Model parameters (α_s , m_{top} and m_{Higgs}) are fixed at their default values.

OPAL

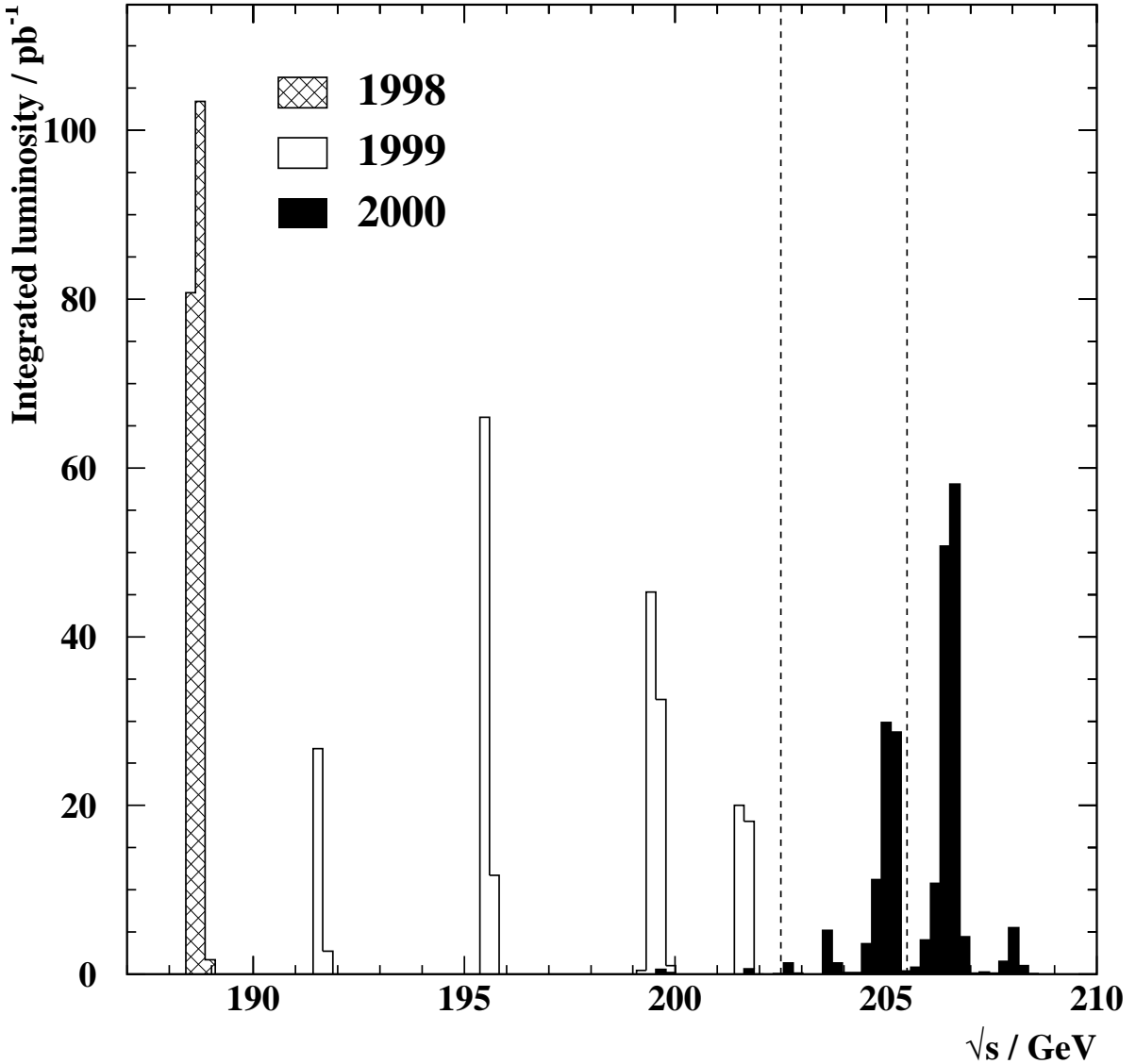


Figure 1: Integrated luminosity collected by OPAL, and used in these analyses, during 1998, 1999 and 2000. The dashed lines indicate the division of the 2000 data into the two centre-of-mass energy bins, $202.5 \text{ GeV} < \sqrt{s} < 205.5 \text{ GeV}$ and $\sqrt{s} > 205.5 \text{ GeV}$. The precise amount of data used in each analysis varies slightly from channel to channel.

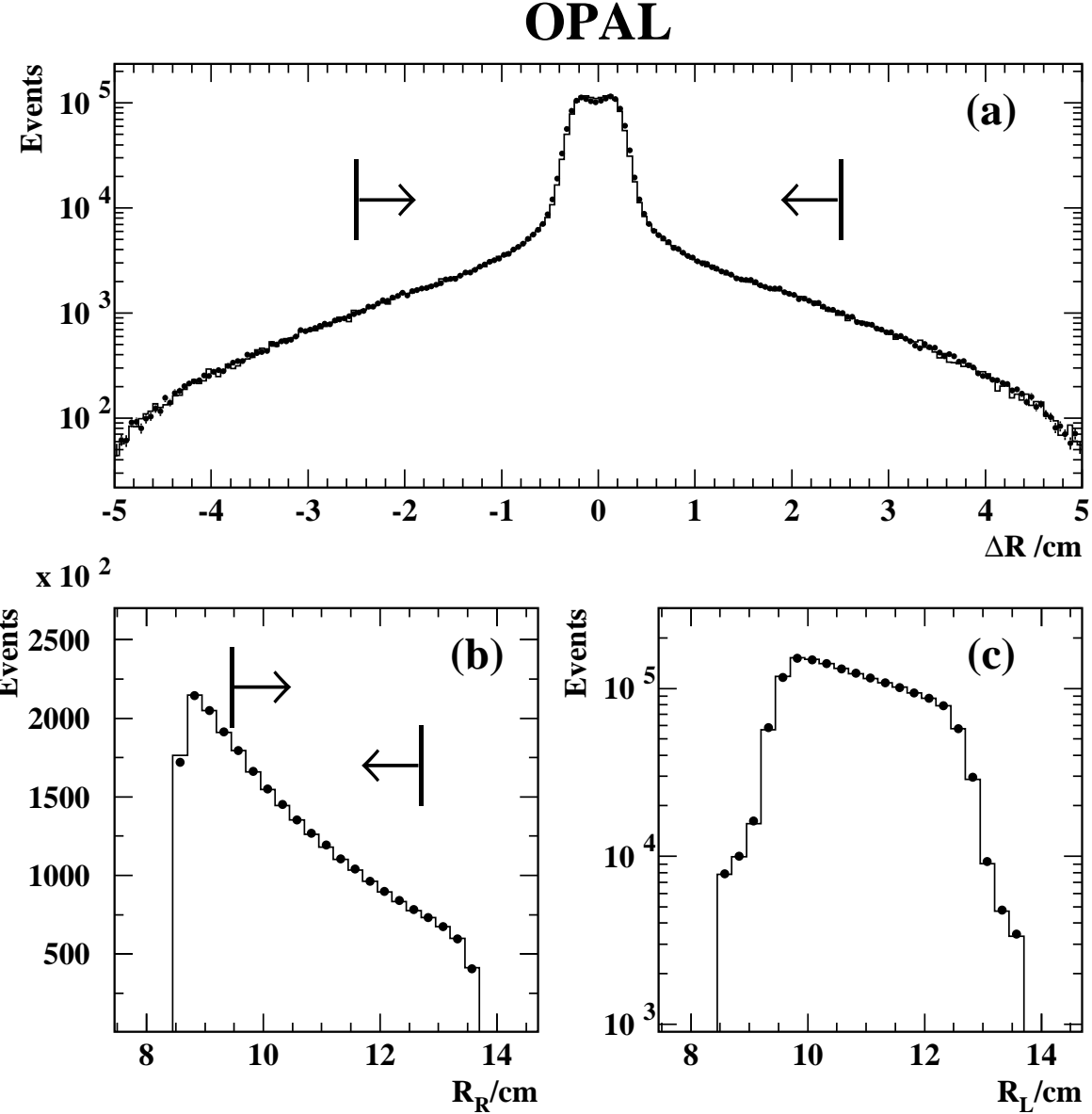


Figure 2: (a) The distribution of the difference in radial coordinate between the two clusters in Bhabha scattering events used for the silicon-tungsten luminosity measurement. Distributions of the radial coordinates of clusters are shown for (b) the ‘narrow’ side and (c) the ‘wide’ side calorimeter. Distributions are shown after all cuts except the acollinearity cut in (a) and the inner and outer radial acceptance cuts, on that side, in (b). Points show the data taken in the year 2000, while the histograms show the Monte Carlo expectation. The vertical bars show the positions of the cuts which define the acceptance, with the arrows pointing into the accepted region.

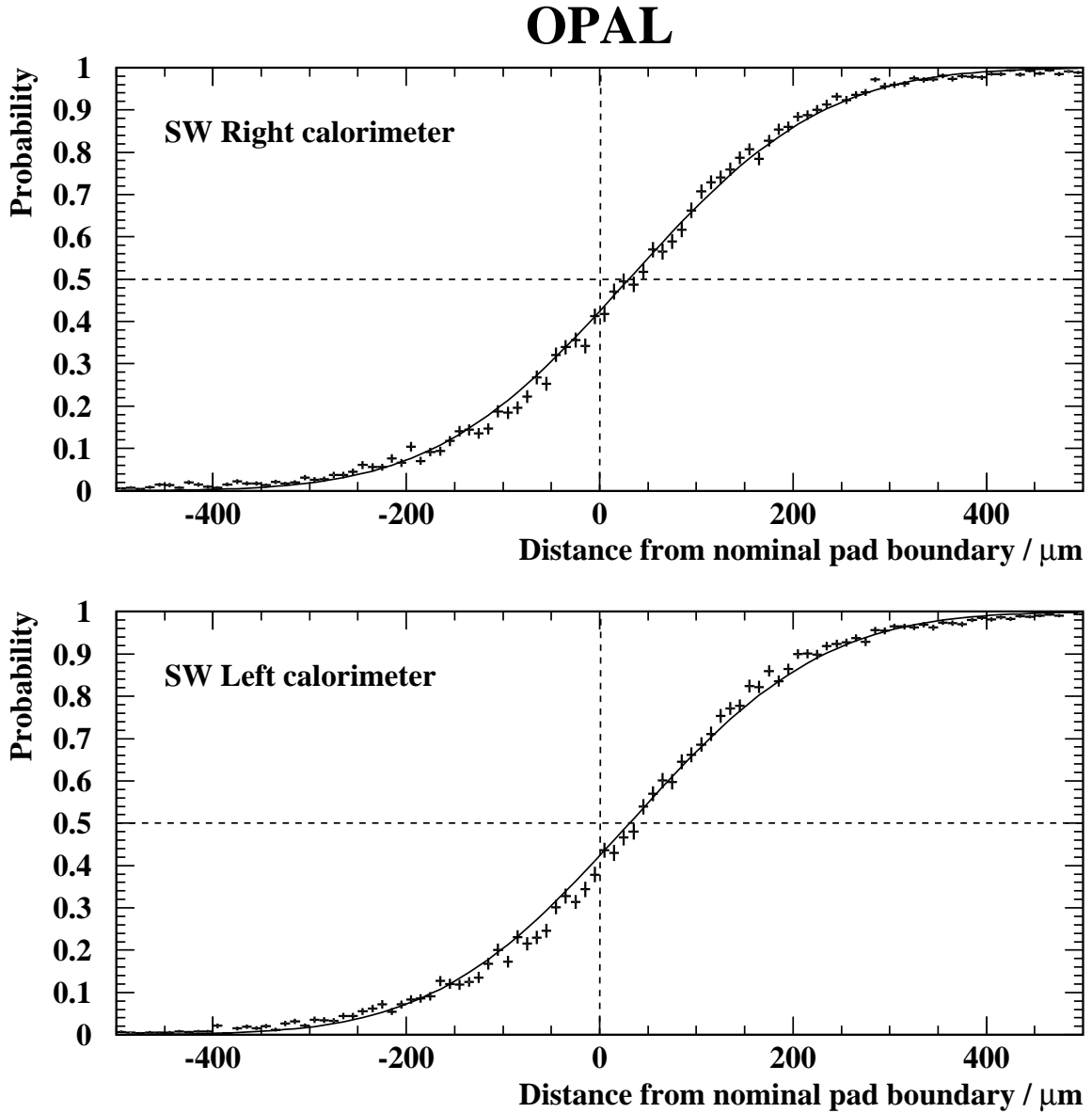


Figure 3: The pad boundary image at the inner acceptance cut ($R_{\text{in}} = 9.45 \text{ cm}$) used in the luminosity measurement. The nominal pad boundary is conventionally set at zero. The points show the fraction of events with pad maximum beyond the nominal cut as a function of distance from the pad boundary for the layer located after 7 radiation lengths, for data taken in 2000. The solid curves show the fitted functions used to determine the coordinate offsets.

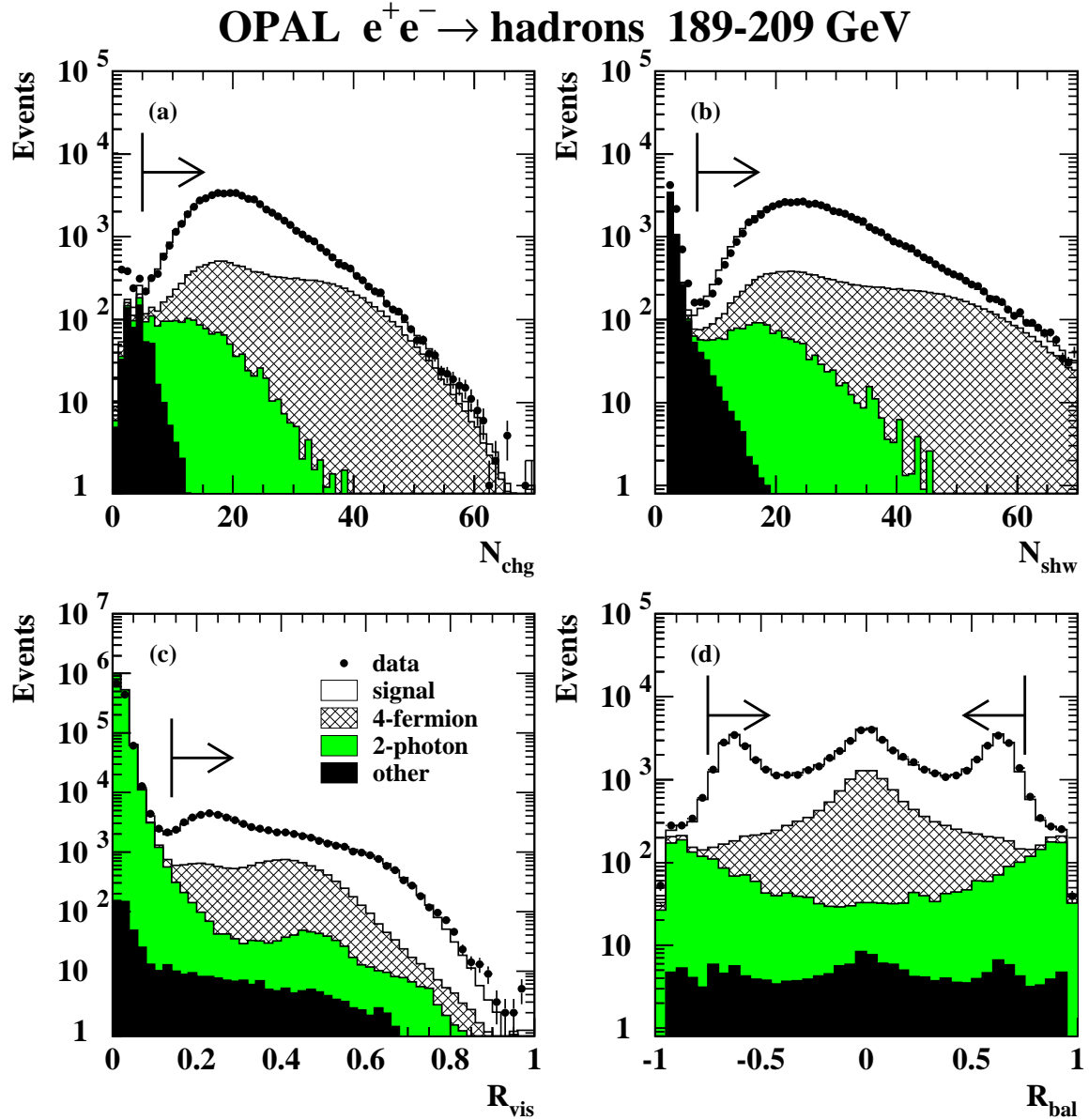


Figure 4: Distributions of variables used in the selection of hadronic events: (a) number of tracks, (b) number of electromagnetic calorimeter clusters, (c) ratio of the visible energy to the centre-of-mass energy and (d) energy balance along the beam direction. The points show the data for all centre-of mass energies combined and the histograms the Monte Carlo predictions normalized to the integrated luminosity of the data. In each case the distribution is shown after the selection cuts associated with the other three variables have been applied. The positions of these cuts are indicated by the vertical bars, with the arrow pointing into the accepted region. The W^+W^- rejection cuts have not been applied. Background labelled ‘other’ is mainly $\tau^+\tau^-$.

OPAL $e^+e^- \rightarrow$ hadrons 189-209 GeV

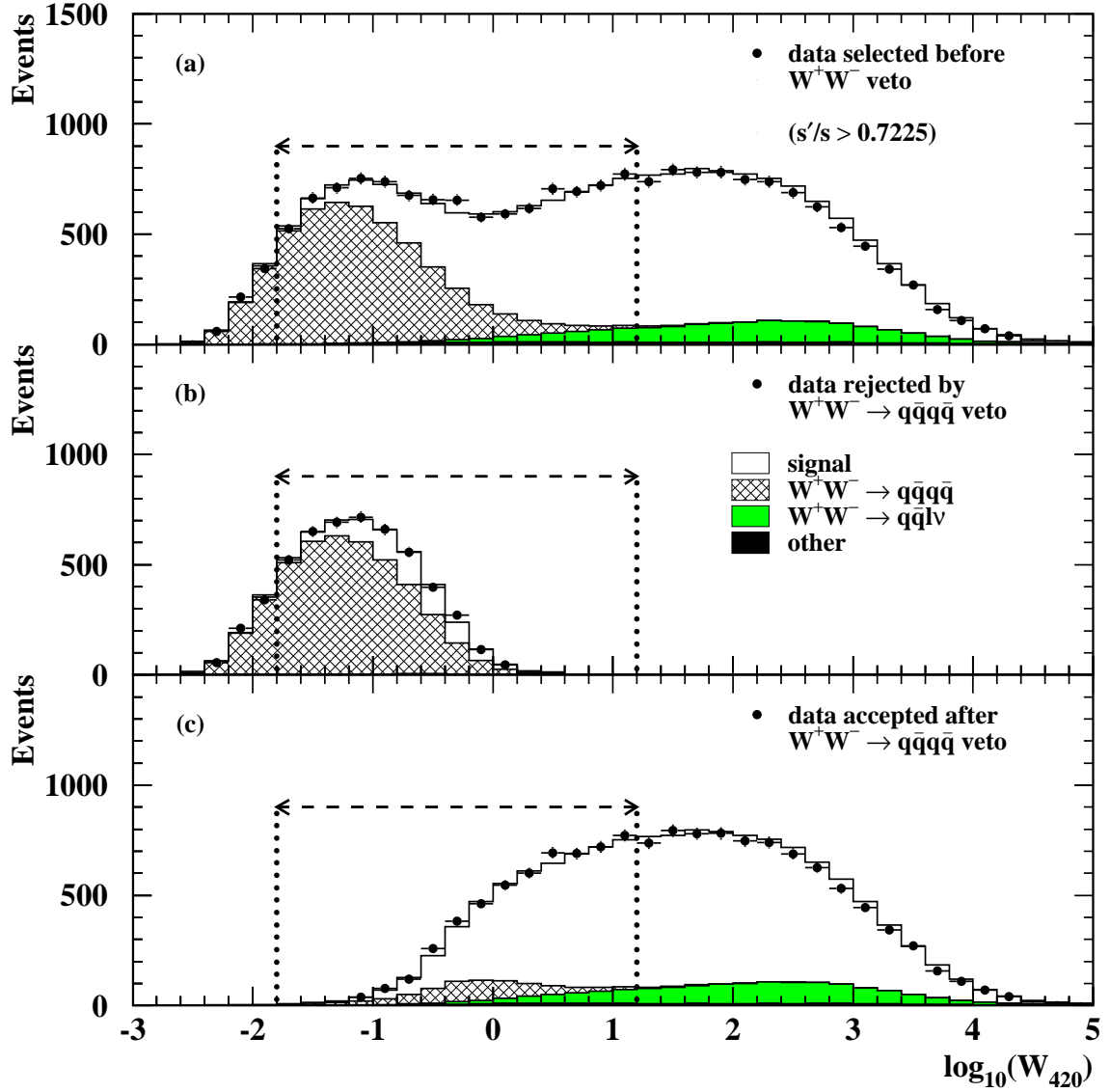


Figure 5: Distributions of the QCD matrix element for four-jet production W_{420} for events (a) passing the hadronic event selection and the non-radiative s' cut before applying the W^+W^- veto, (b) additionally failing the $W^+W^- \rightarrow q\bar{q}q\bar{q}$ veto or (c) additionally passing the $W^+W^- \rightarrow q\bar{q}q\bar{q}$ veto. The points show the data for all centre-of-mass energies combined and the histograms the Monte Carlo predictions normalized to the integrated luminosity of the data. The contributions from signal events and from the various sources of background are indicated, while the fit region (discussed in the text) is shown by the arrows.

OPAL $e^+e^- \rightarrow \mu^+\mu^-$ 189-209 GeV

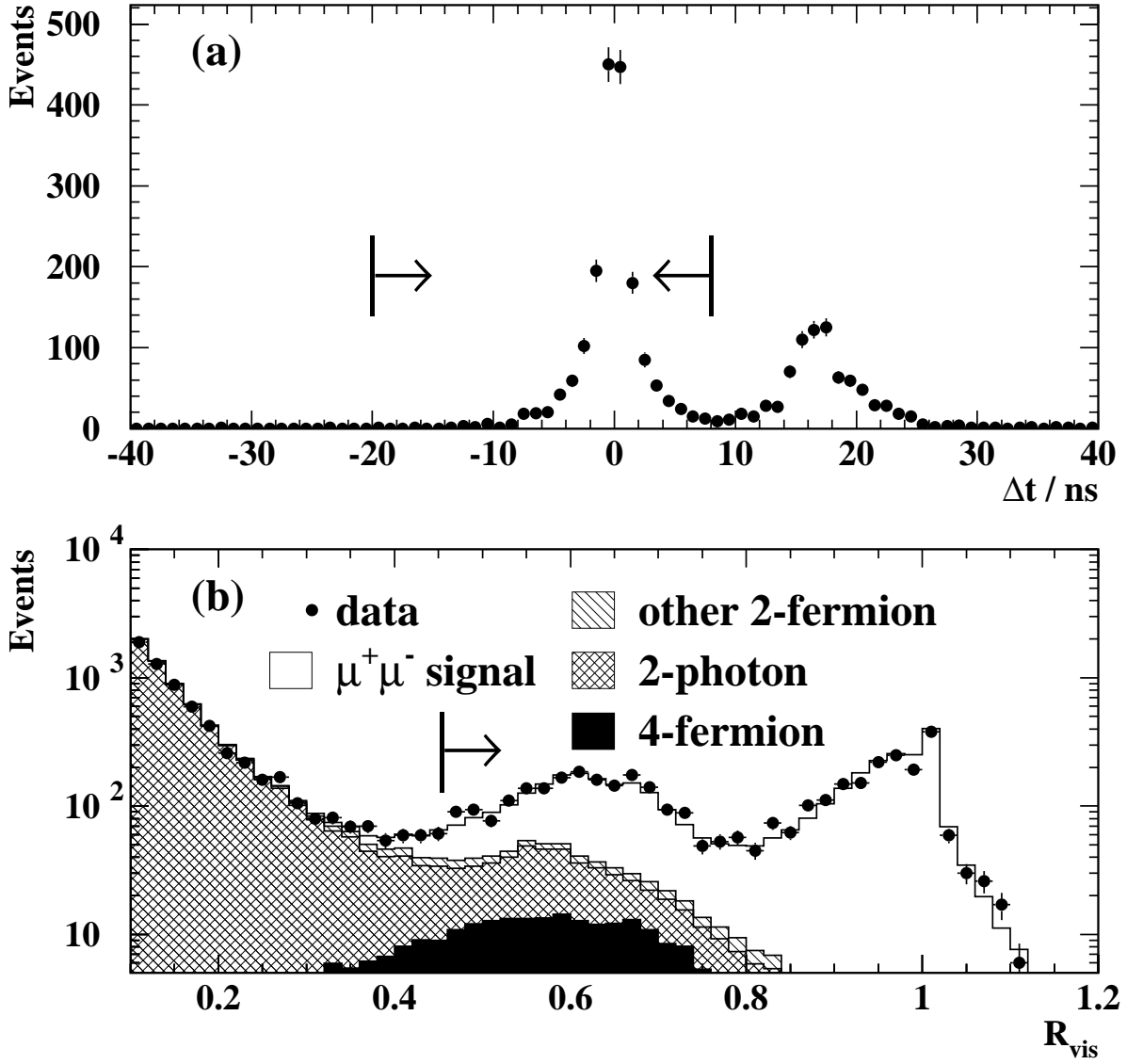


Figure 6: (a) Time difference between back-to-back hits in the time-of-flight counters in the barrel region. Events in the combined data sample which pass all $\mu^+\mu^-$ selection criteria except for the cosmic veto are included, if they have back-to-back TOF hits. (b) Ratio of the visible energy, defined as the sum of the muon momenta plus the energy of the highest energy electromagnetic calorimeter cluster, to the centre-of-mass energy, for $\mu^+\mu^-$ candidates passing all cuts except those on the visible energy and the mass of the muon pair. The points show the combined data and the histograms show the Monte Carlo expectation, normalized to the integrated luminosity of the data, with the background contributions as indicated. The vertical bars indicate the positions of the cuts (for a centre-of-mass energy of 200 GeV in (b)), with the arrow pointing into the accepted region in each case.

OPAL $e^+e^- \rightarrow \tau^+\tau^-$ 189-209 GeV

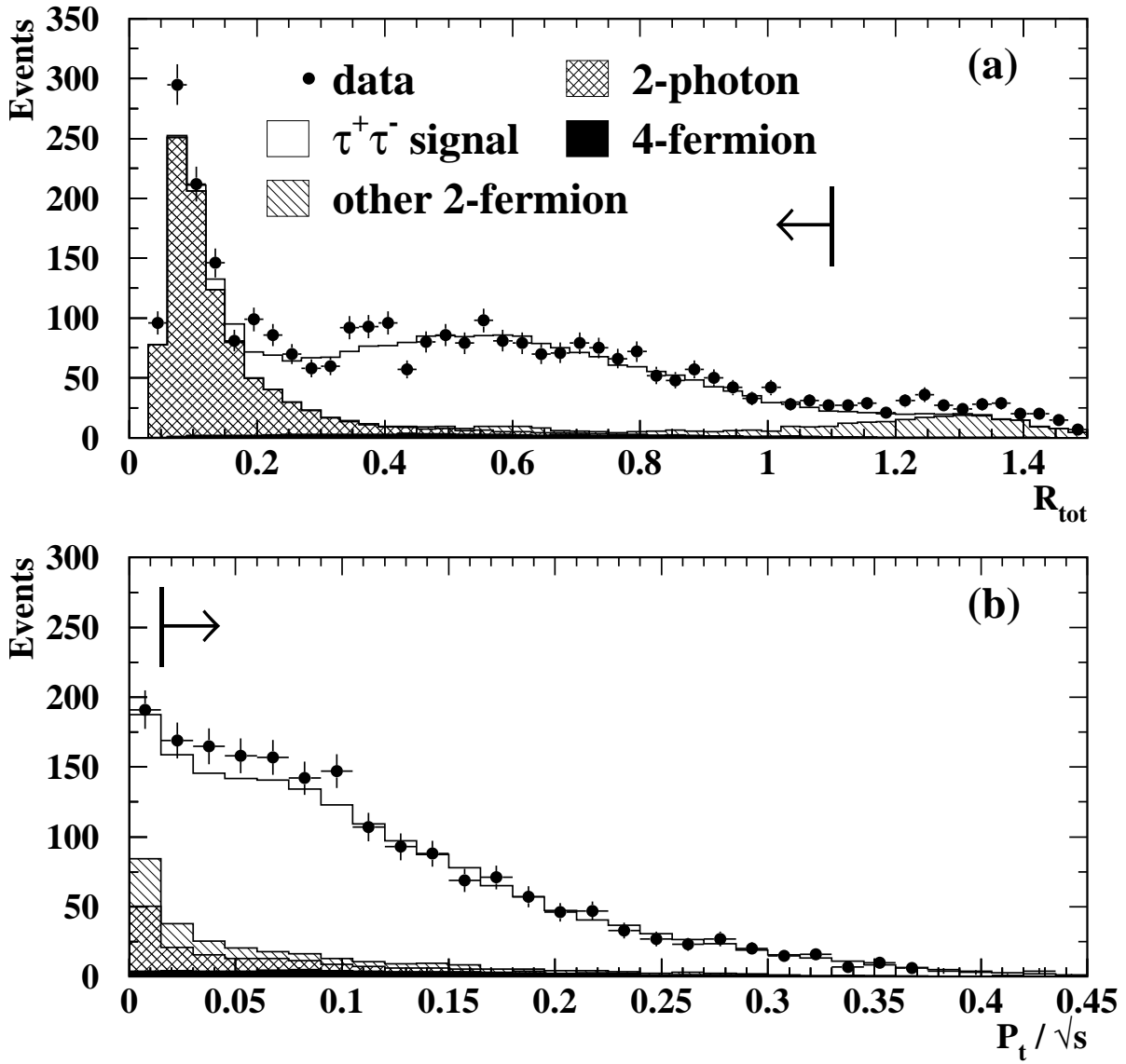


Figure 7: (a) Ratio of the total event energy, defined as the scalar sum of track momenta plus the energy of electromagnetic calorimeter clusters, to the centre-of-mass energy, for $\tau^+\tau^-$ candidates passing all cuts except those on the visible energy and its track and cluster components. (b) The missing momentum, calculated using electromagnetic calorimeter clusters, divided by the centre-of-mass energy for $\tau^+\tau^-$ events passing all cuts except those on the missing momentum and the cosine of the polar angle of its direction. In each case, the points show the combined data and the histograms show the Monte Carlo expectations, normalized to the integrated luminosity of the data, with the background contributions as indicated. The vertical bars indicate the positions of the cuts, with the arrow pointing into the accepted region in each case. Note that, in the case of the total event energy in (a), further cuts are placed on the separate track and cluster components at both low and high values.

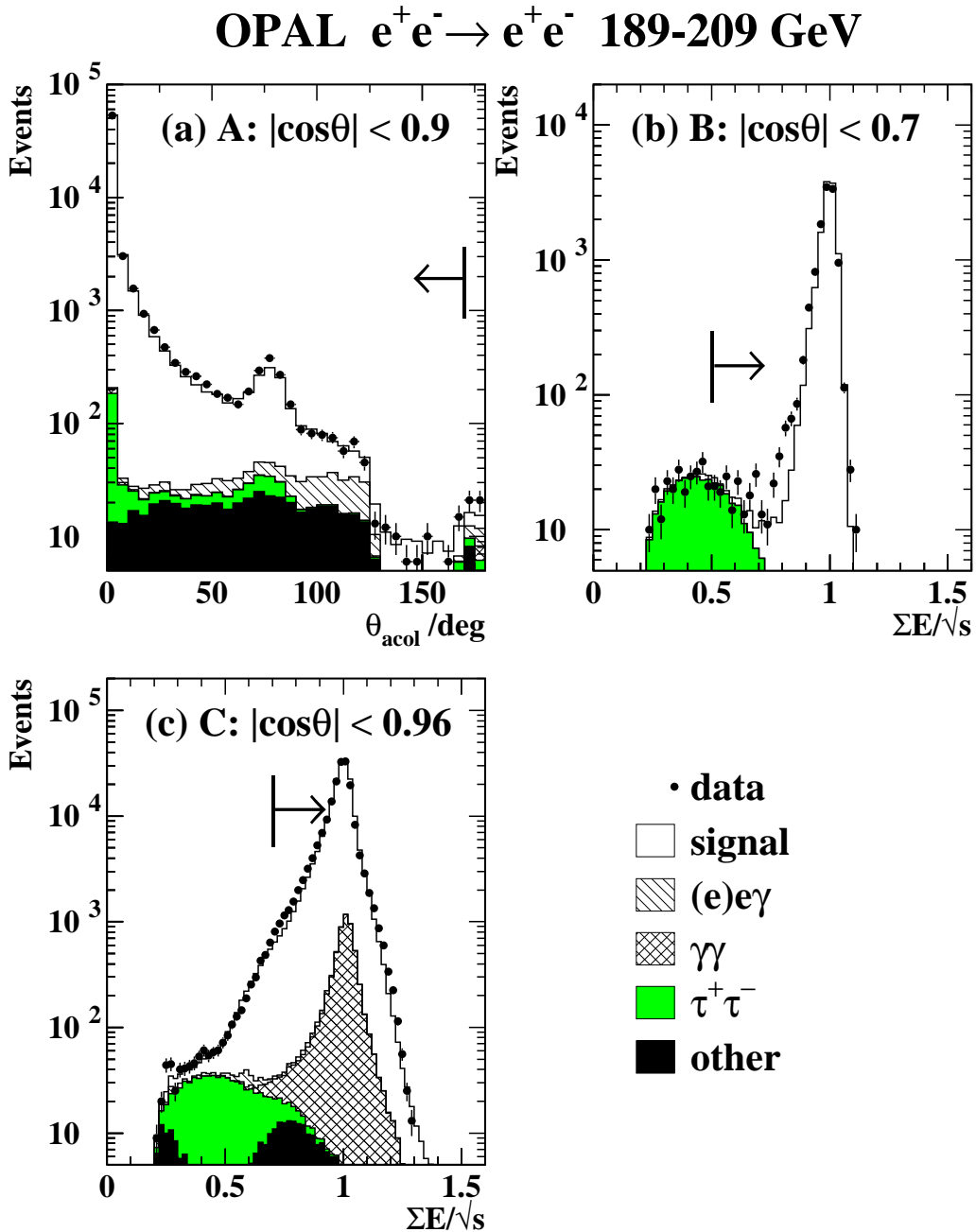


Figure 8: (a) The acollinearity angle distribution for events satisfying the inclusive $e^+e^- \rightarrow e^+e^-$ selection, in the acceptance region A, $|\cos\theta_{e^\pm}| < 0.9$. (b) The distribution of the ratio of total electromagnetic calorimeter energy to the centre-of-mass energy for $e^+e^- \rightarrow e^+e^-$ events in acceptance region B, $|\cos\theta_{e^-}| < 0.7$ and $\theta_{\text{acol}} < 10^\circ$. (c) The same distribution for the large acceptance region, C, $|\cos\theta_{e^\pm}| < 0.96$ and $\theta_{\text{acol}} < 10^\circ$. Distributions are shown after all cuts except the one on the variable plotted. In each case, the points show the combined data and the histograms the Monte Carlo expectations, normalized to the integrated luminosity of the data, with the background contributions as indicated. The vertical bars indicate the positions of the cuts in the displayed variable, with the arrow pointing into the accepted region in each case.

OPAL 189 - 209 GeV

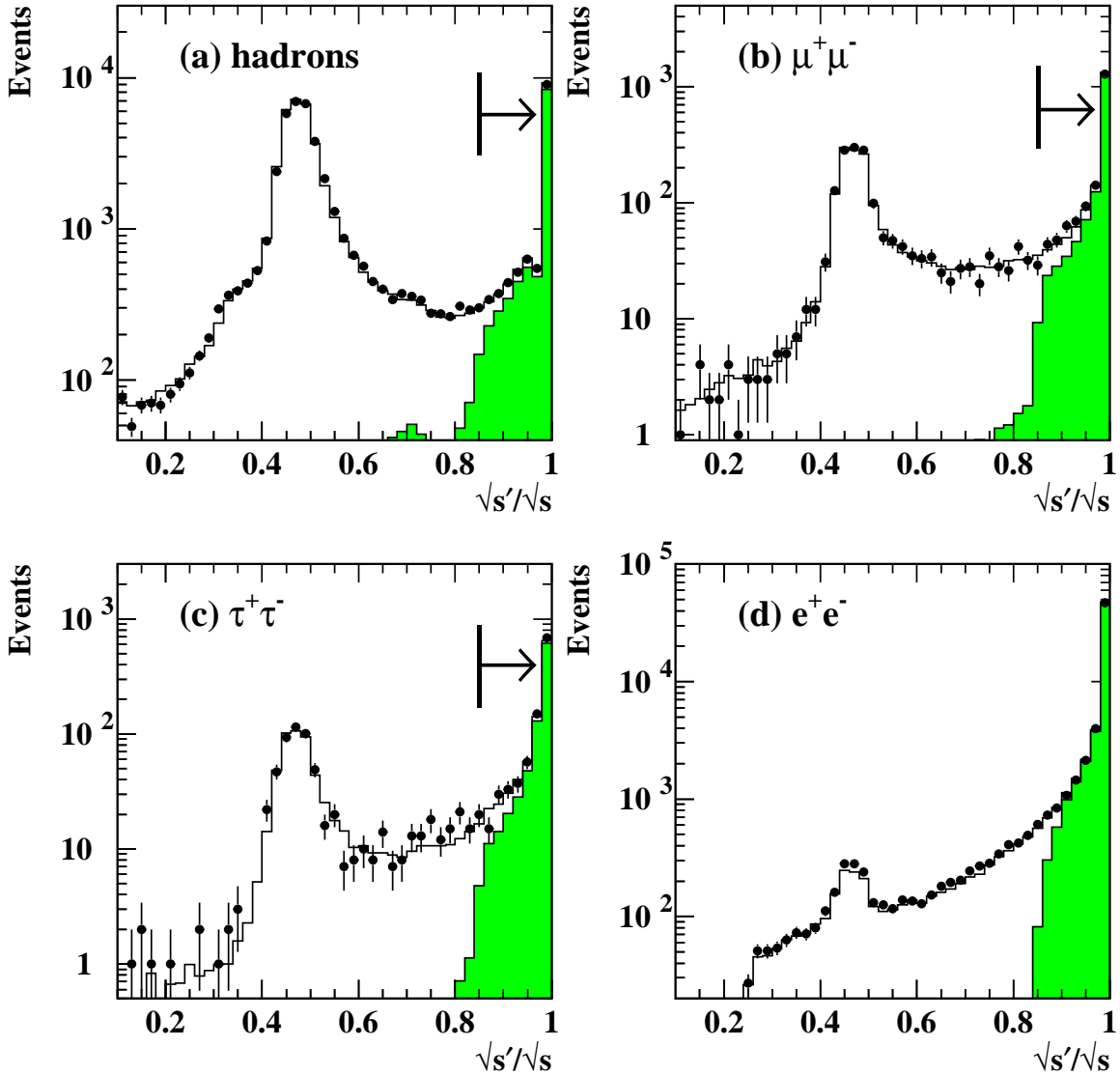


Figure 9: The distributions of reconstructed $\sqrt{s'}/\sqrt{s}$ for (a) hadronic events, (b) $\mu^+ \mu^-$ events, (c) $\tau^+ \tau^-$ events and (d) $e^+ e^-$ events with $|\cos \theta_{e^\pm}| < 0.9$ and $\theta_{\text{acol}} < 170^\circ$, for all data combined. In each case, the points show the data and the histogram the Monte Carlo prediction, normalized to the integrated luminosity of the data, with the contribution from events with true $s'/s > 0.7225$ shaded in (a), (b) and (c), and the contribution from events with $\theta_{\text{acol}} < 10^\circ$ shaded in (d). The vertical bars in (a), (b) and (c) show the position of the cut used to select 'non-radiative' events.

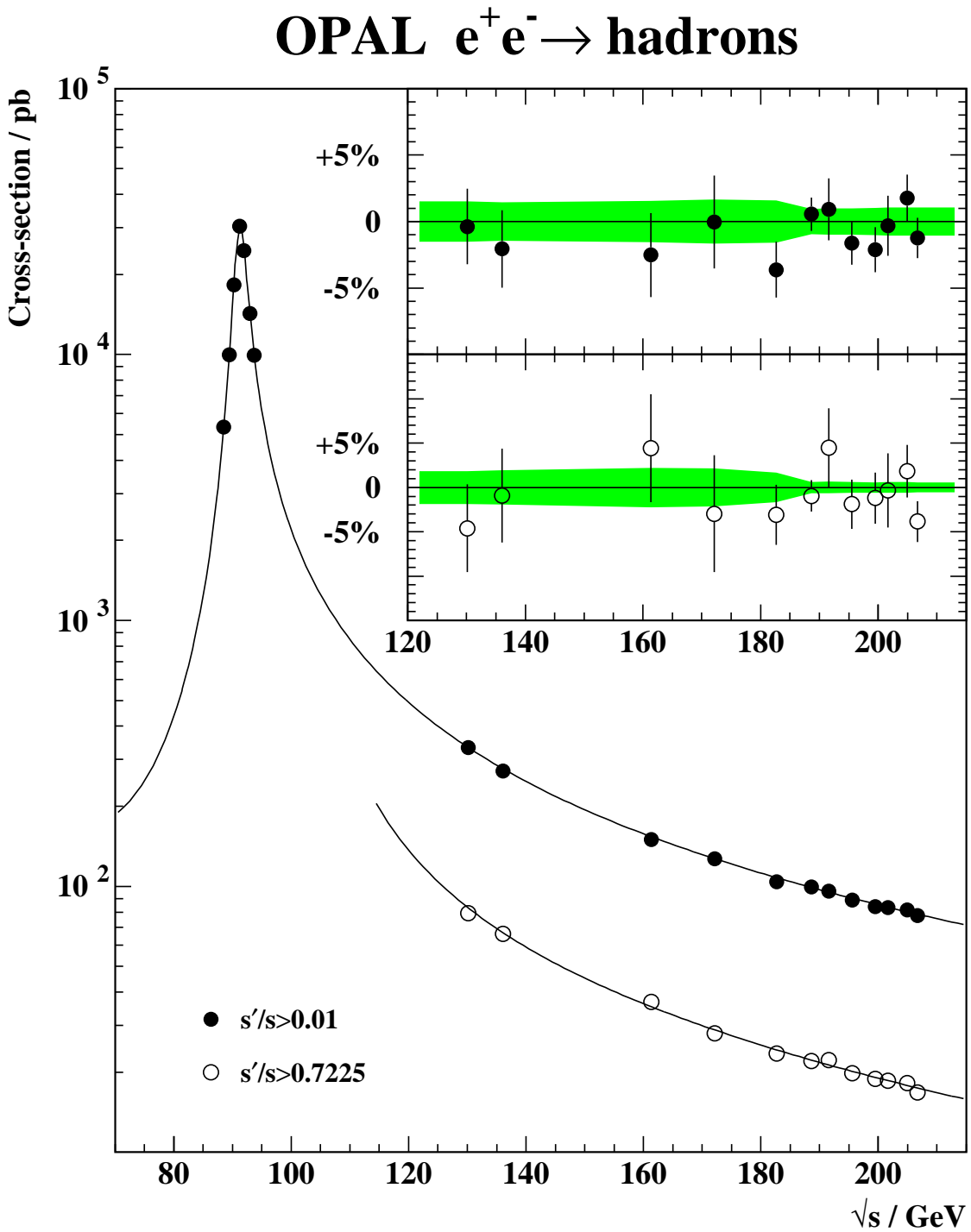


Figure 10: Measured total cross-sections ($s'/s > 0.01$) for hadronic events at lower energies [2, 3, 39] and this analysis. Cross-section measurements for $s'/s > 0.7225$ from this analysis and from [2, 3] are also shown; the values at 161 GeV and 172 GeV have been corrected from $s'/s > 0.8$ to $s'/s > 0.7225$ by adding the prediction of ZFITTER for this difference before plotting. The curves show the predictions of ZFITTER. The insets show the percentage differences between the measured values and the ZFITTER predictions for the high energy points. The error bars on the differences represent statistical errors only; the size of the experimental systematic error is indicated by the shaded band.

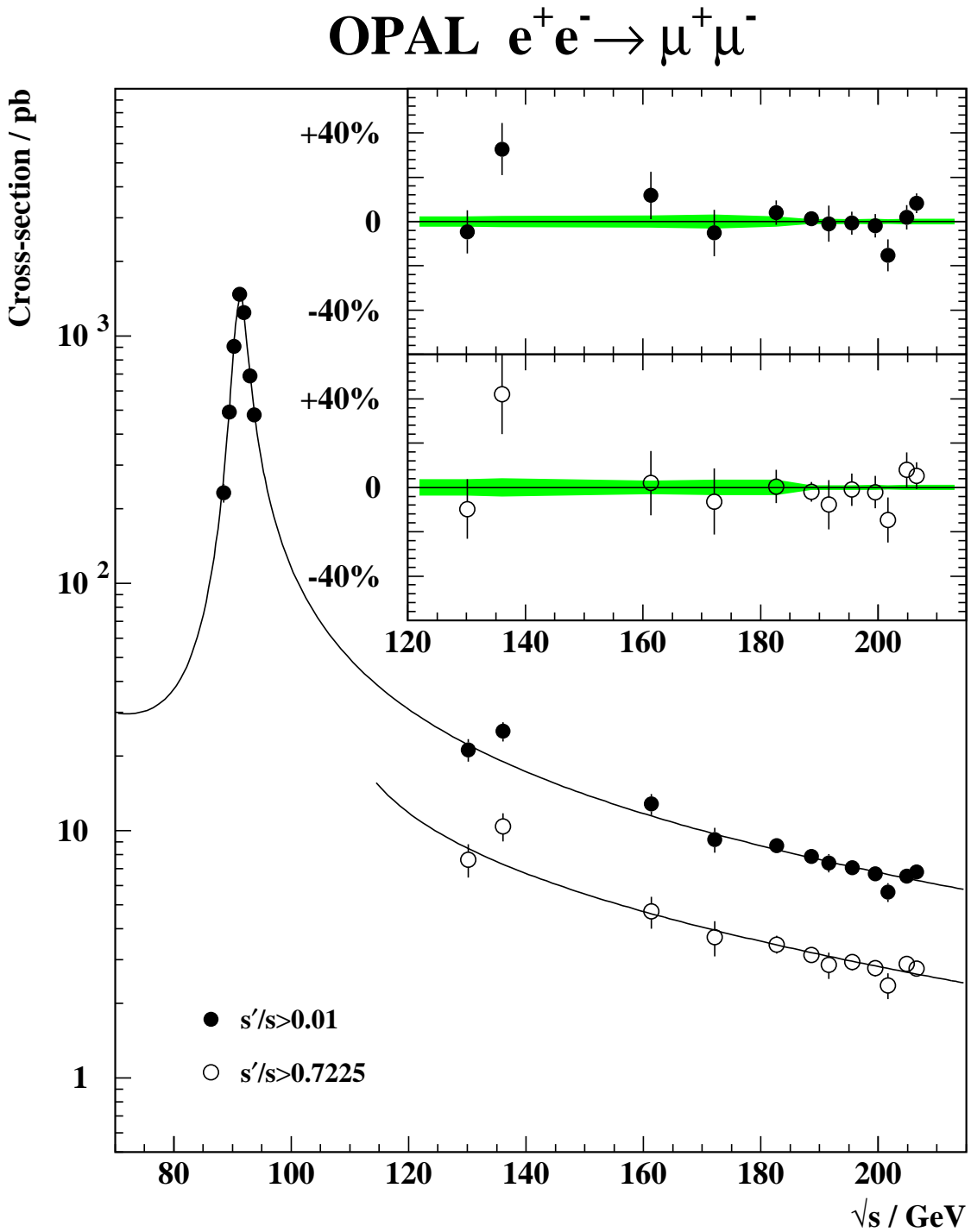


Figure 11: Measured total cross-sections ($s'/s > 0.01$) for $\mu^+\mu^-$ events at lower energies [2,3,39] and this analysis. Cross-section measurements for $s'/s > 0.7225$ from this analysis and from [2, 3] are also shown; the values at 161 GeV and 172 GeV have been corrected from $s'/s > 0.8$ to $s'/s > 0.7225$ by adding the prediction of ZFITTER for this difference before plotting. The curves show the predictions of ZFITTER. The insets show the percentage differences between the measured values and the ZFITTER predictions for the high energy points. The error bars on the differences represent statistical errors only; the size of the experimental systematic error is indicated by the shaded band.

OPAL $e^+e^- \rightarrow \tau^+\tau^-$

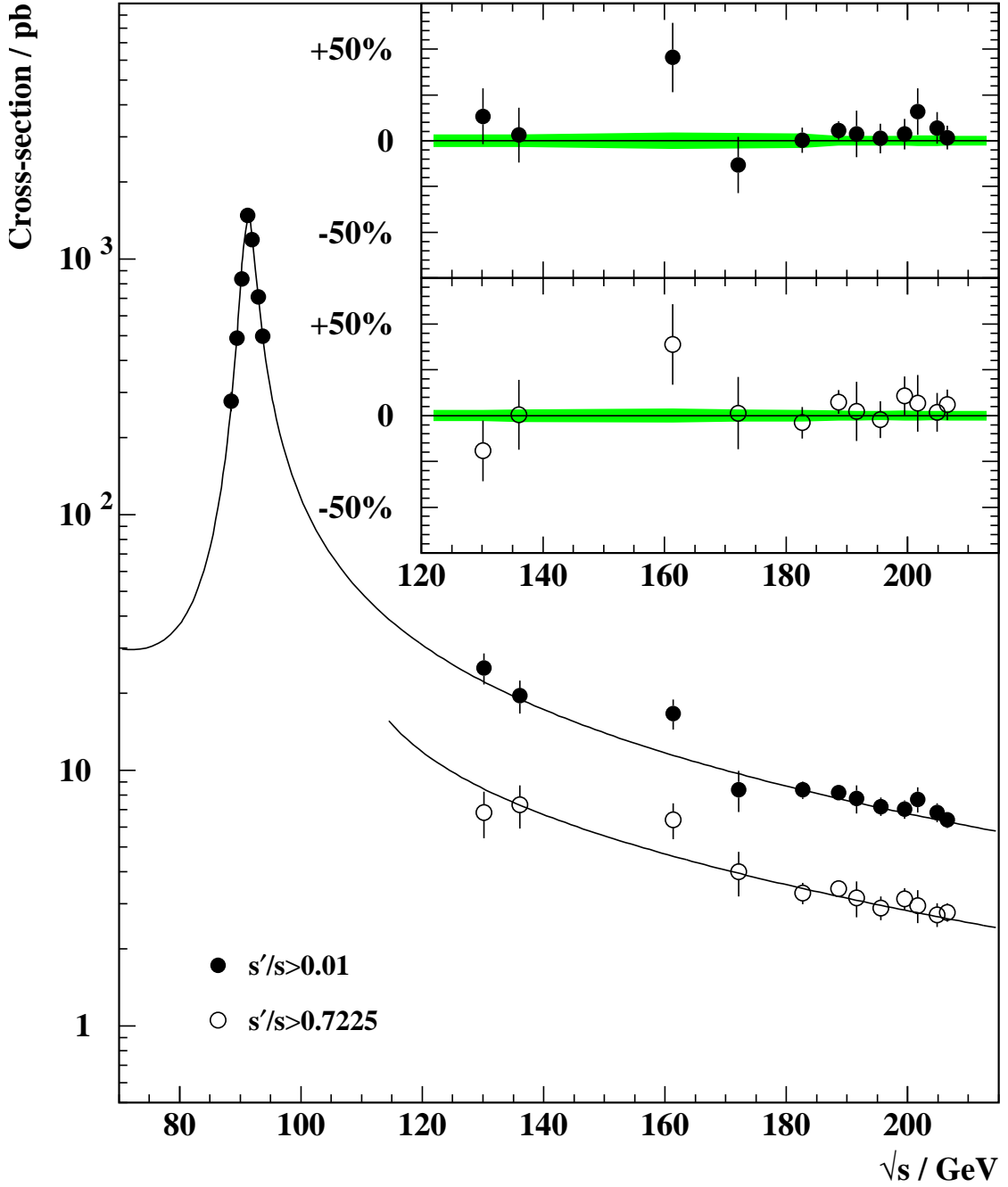


Figure 12: Measured total cross-sections ($s'/s > 0.01$) for $\tau^+\tau^-$ events at lower energies [2,3,39], and this analysis. Cross-section measurements for $s'/s > 0.7225$ from this analysis and from [2, 3] are also shown; the values at 161 GeV and 172 GeV have been corrected from $s'/s > 0.8$ to $s'/s > 0.7225$ by adding the prediction of ZFITTER for this difference before plotting. The curves show the predictions of ZFITTER. The insets show the percentage differences between the measured values and the ZFITTER predictions for the high energy points. The error bars on the differences represent statistical errors only; the size of the experimental systematic error is indicated by the shaded band.

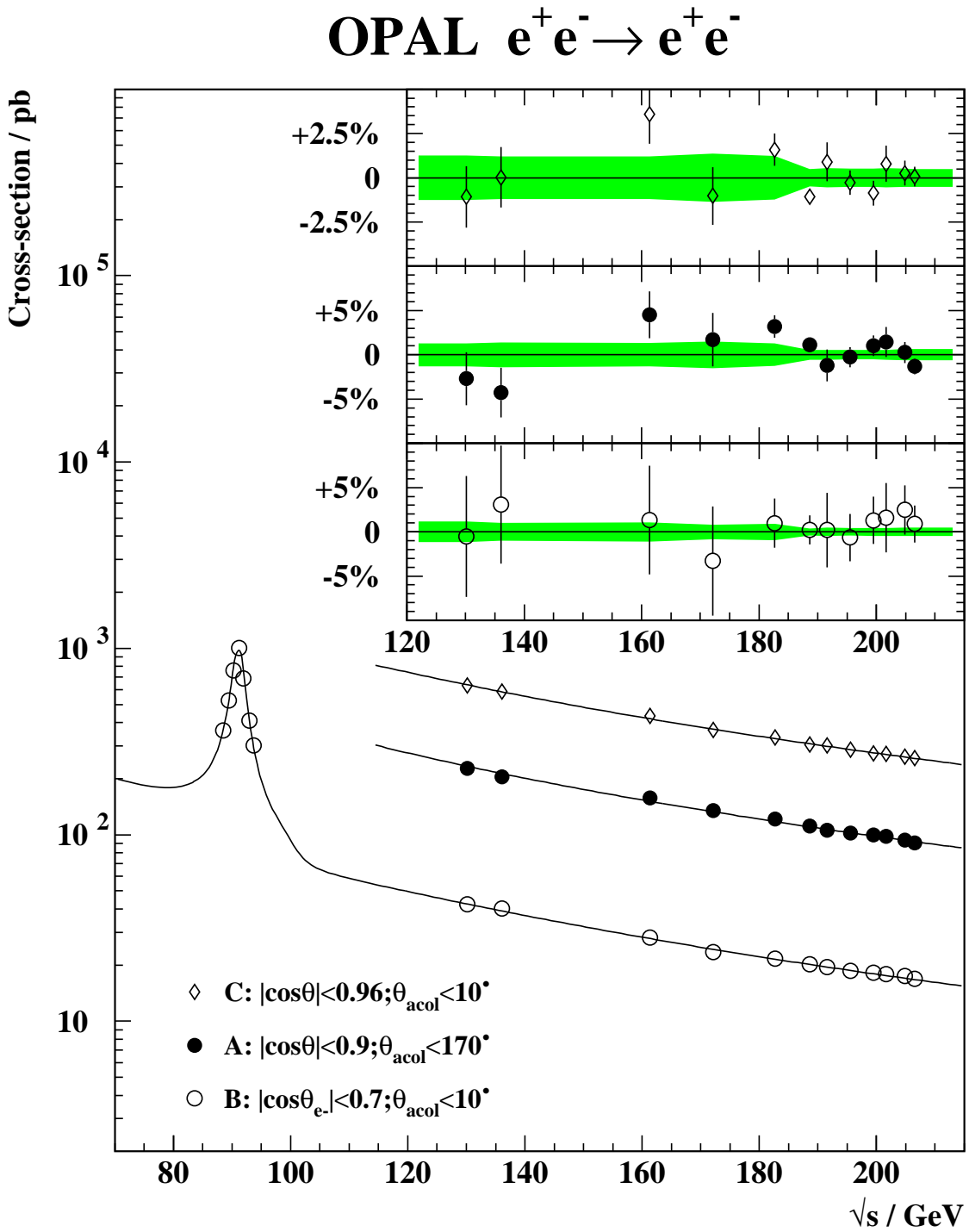


Figure 13: Measured cross-sections for e^+e^- events at lower energies [2,3,39], and this analysis. The curves show the predictions of BHWIDE. The insets show the percentage differences between the measured values and the BHWIDE predictions for the high energy points. The error bars on the differences represent statistical errors only; the size of the experimental systematic error is indicated by the shaded band.

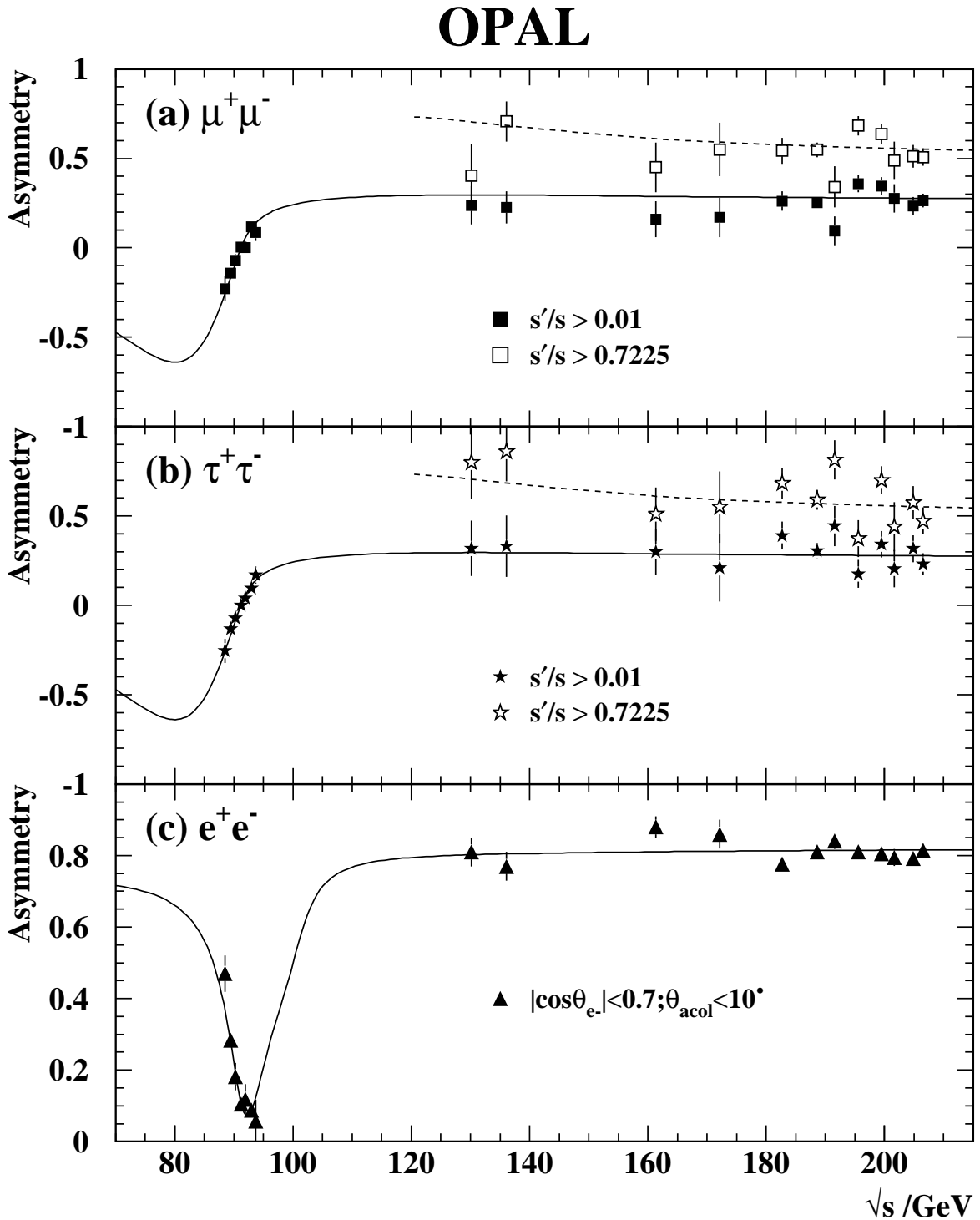


Figure 14: (a) and (b) Measured asymmetries for inclusive ($s'/s > 0.01$) and non-radiative ($s'/s > 0.7225$) samples as functions of \sqrt{s} for $\mu^+\mu^-$ and $\tau^+\tau^-$ events. The curves show ZFITTER predictions for $s'/s > 0.01$ (solid) and $s'/s > 0.7225$ (dashed). (c) Measured forward-backward asymmetry for e^+e^- with $|\cos\theta_{e^-}| < 0.7$ and $\theta_{\text{acol}} < 10^\circ$, as a function of \sqrt{s} . The curve shows the prediction of BHWIDE. Lower energy data values are taken from [2, 3, 39] for all channels.

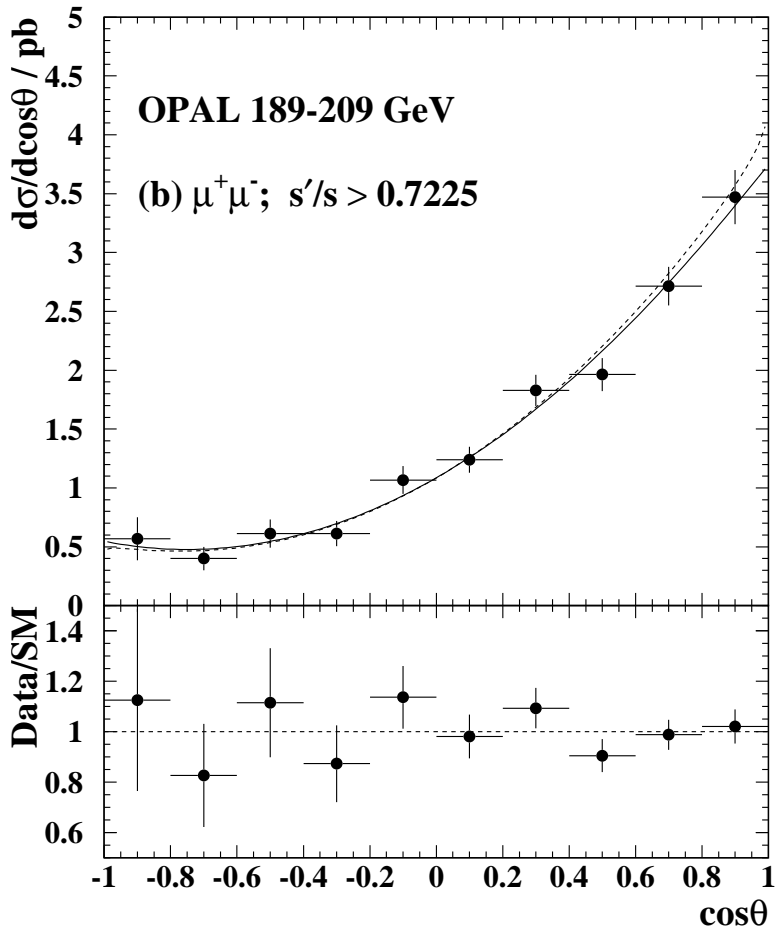
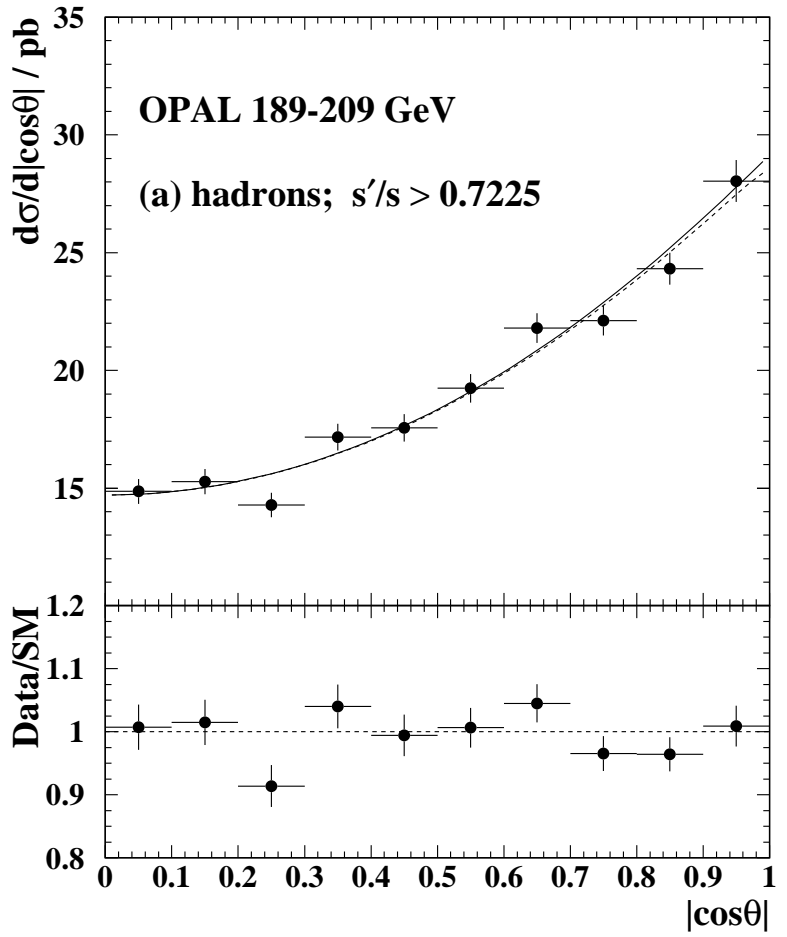


Figure 15: Measured differential cross-sections for (a) hadronic events with $s'/s > 0.7225$ and (b) $\mu^+\mu^-$ events with $s'/s > 0.7225$. The points show the luminosity-weighted average of all data from 189 GeV to 207 GeV, corrected to no interference between initial- and final-state radiation. The curves show the predictions of ZFITTER without interference between initial- and final-state radiation (solid) and with interference (dashed). In each case the lower plot shows the ratio of the measurements to the Standard Model predictions (excluding interference).

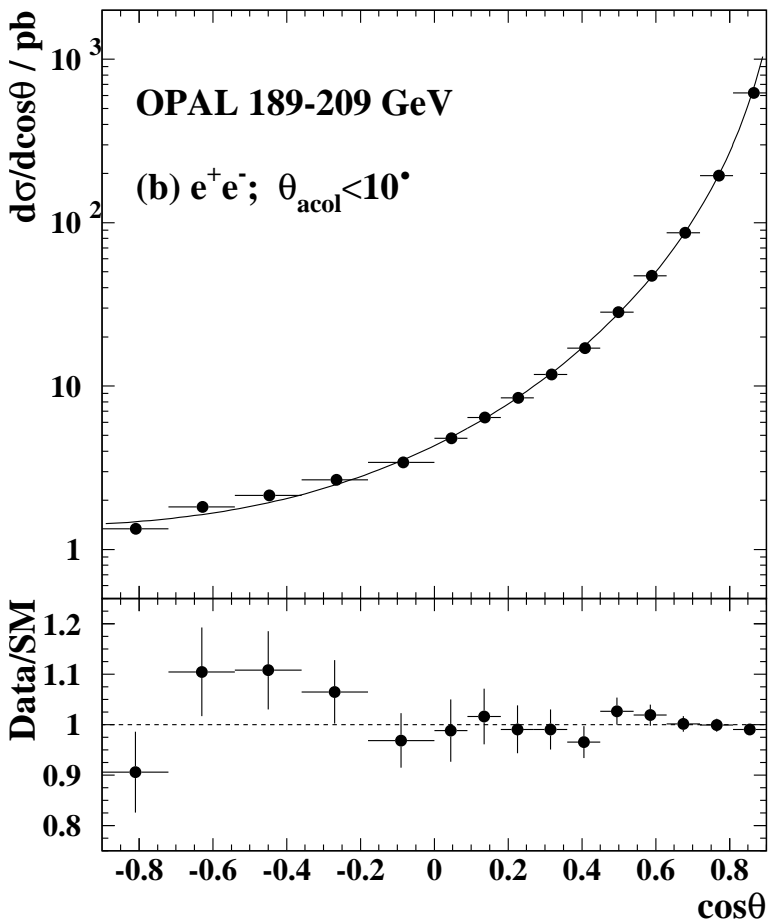
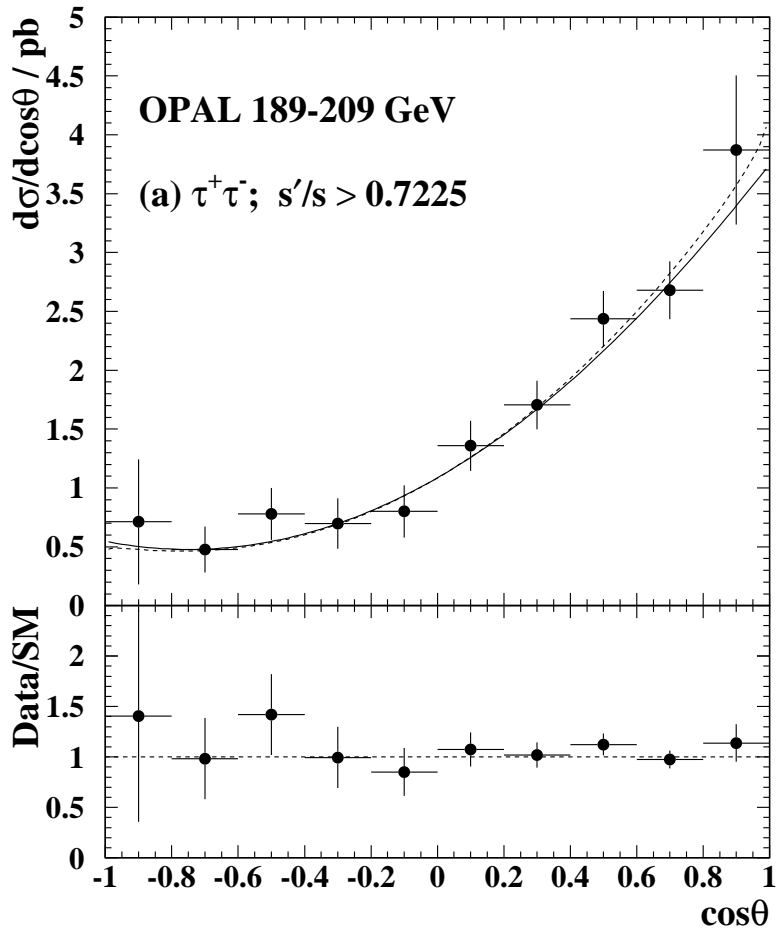


Figure 16: Measured differential cross-sections for (a) $\tau^+\tau^-$ events with $s'/s > 0.7225$ and (b) e^+e^- events with $\theta_{\text{acol}} < 10^\circ$. The points show the luminosity-weighted average of all data from 189 GeV to 207 GeV, corrected to no interference between initial- and final-state radiation in (a). The curves in (a) show the predictions of ZFITTER without interference between initial- and final-state radiation (solid) and with interference (dashed). The curve in (b) shows the prediction of BHWIDE. In each case the lower plot shows the ratio of the measurements to the Standard Model predictions (excluding interference in (a)).

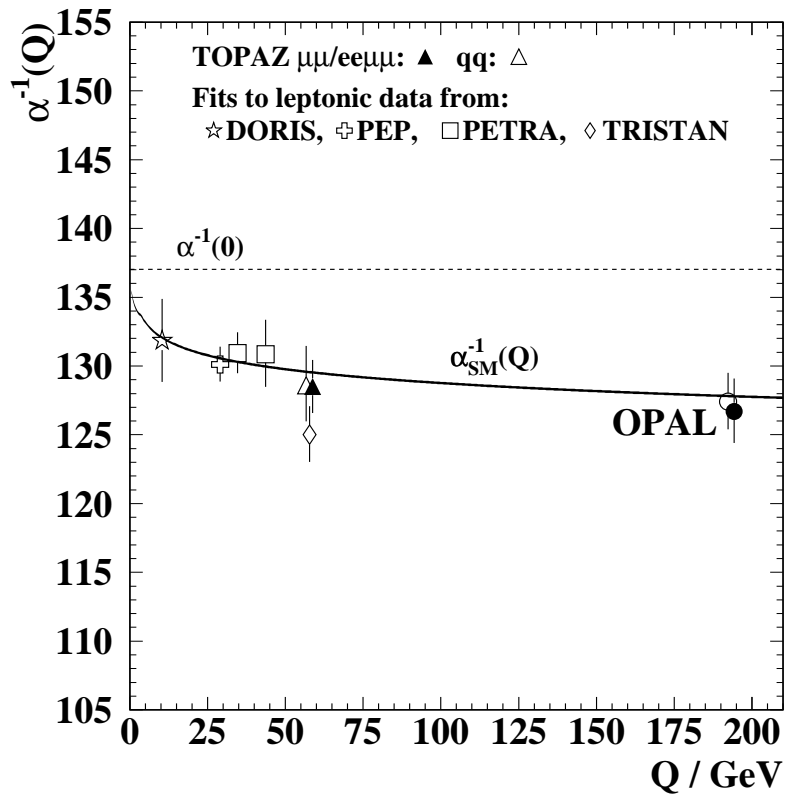
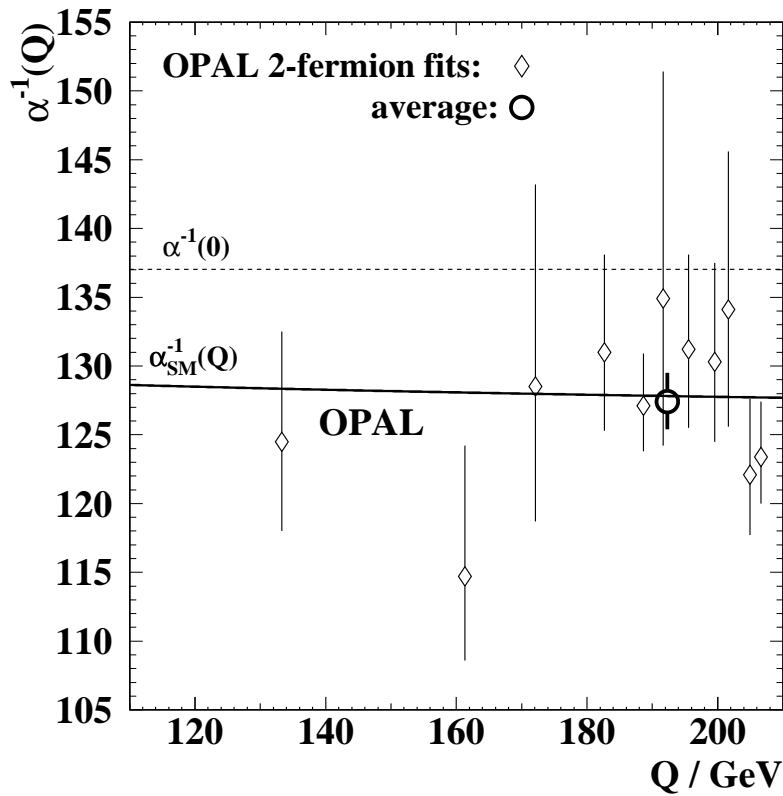


Figure 17: Fitted values of $1/\alpha_{\text{em}}$ as a function of Q , which is \sqrt{s} for the OPAL fits. The left plot shows the results of fits to OPAL data at each centre-of-mass energy and of the combined fit in which α_{em} runs with a slope obtained from fixing $1/\alpha_{\text{em}}(0) = 137.036$. The right plot compares the results of the OPAL combined fits with values obtained by the TOPAZ experiment [43] and from fits to measurements of leptonic cross-sections and asymmetries at the DORIS, PEP, PETRA and TRISTAN e^+e^- storage rings [44]. Measurements shown by open symbols rely on assuming the Standard Model running of α_{em} for Q_{lumi} below 4 GeV, whereas closed symbols indicate values derived from cross-section ratios which do not depend on luminosity, as discussed in Section 5.1. The solid line shows the Standard Model expectation, with the thickness representing the uncertainty, while the value of $1/\alpha_{\text{em}}(0)$ is shown by the dashed line.

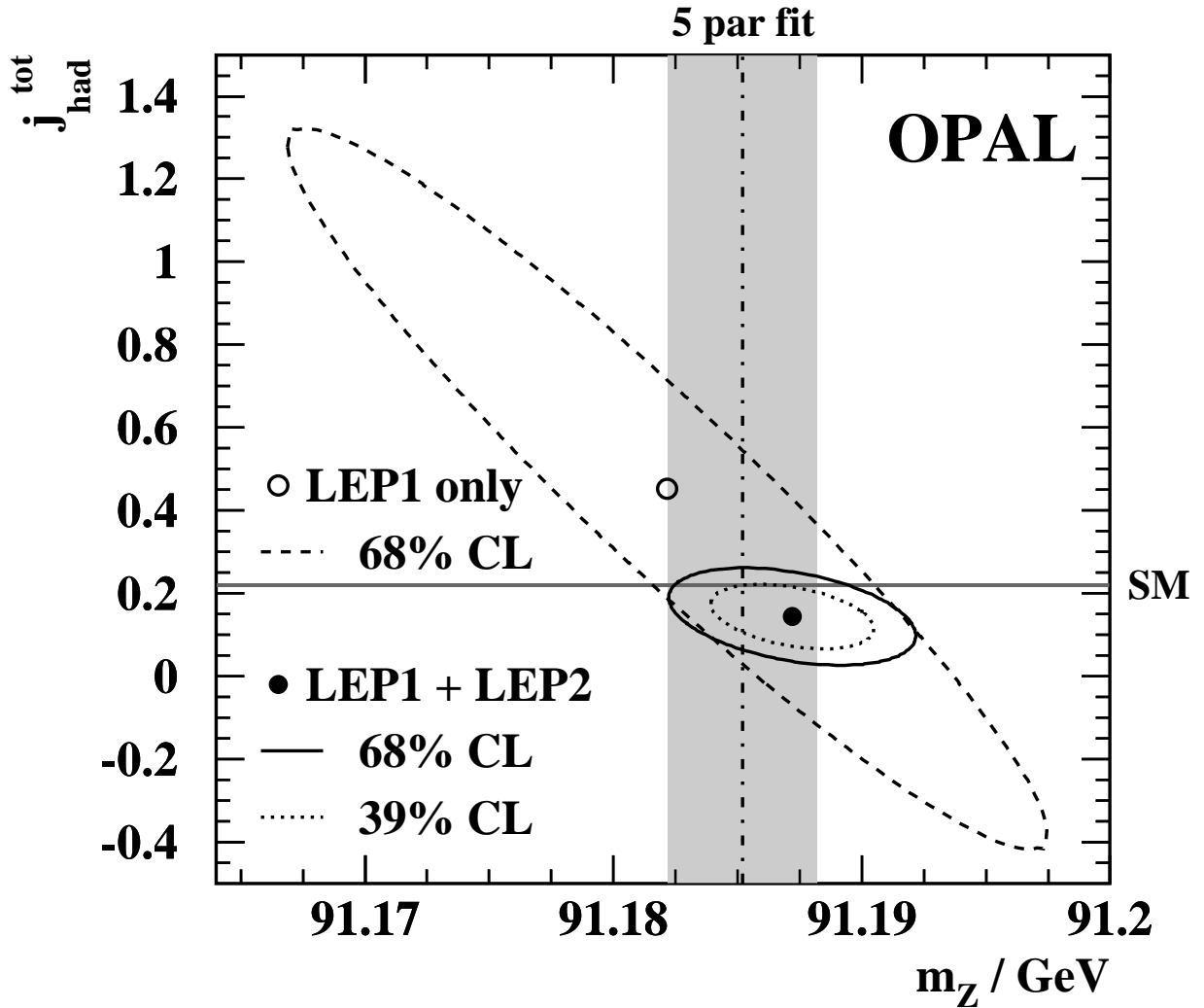


Figure 18: Confidence level contours in the m_Z - $j_{\text{had}}^{\text{tot}}$ plane from the S-matrix fits with lepton universality. The dashed curve shows the 68% confidence level contour from the fit to LEP 1 data alone, while the full and dotted curves show the 68% and 39% confidence level contours, respectively, from the fit to LEP 1 and LEP 2 data. The horizontal band indicates the Standard Model value of $j_{\text{had}}^{\text{tot}}$. The vertical band is the 1σ error on the Z mass from the five parameter fit [39] which should be compared with the 39% confidence level contour from the S-matrix fit.

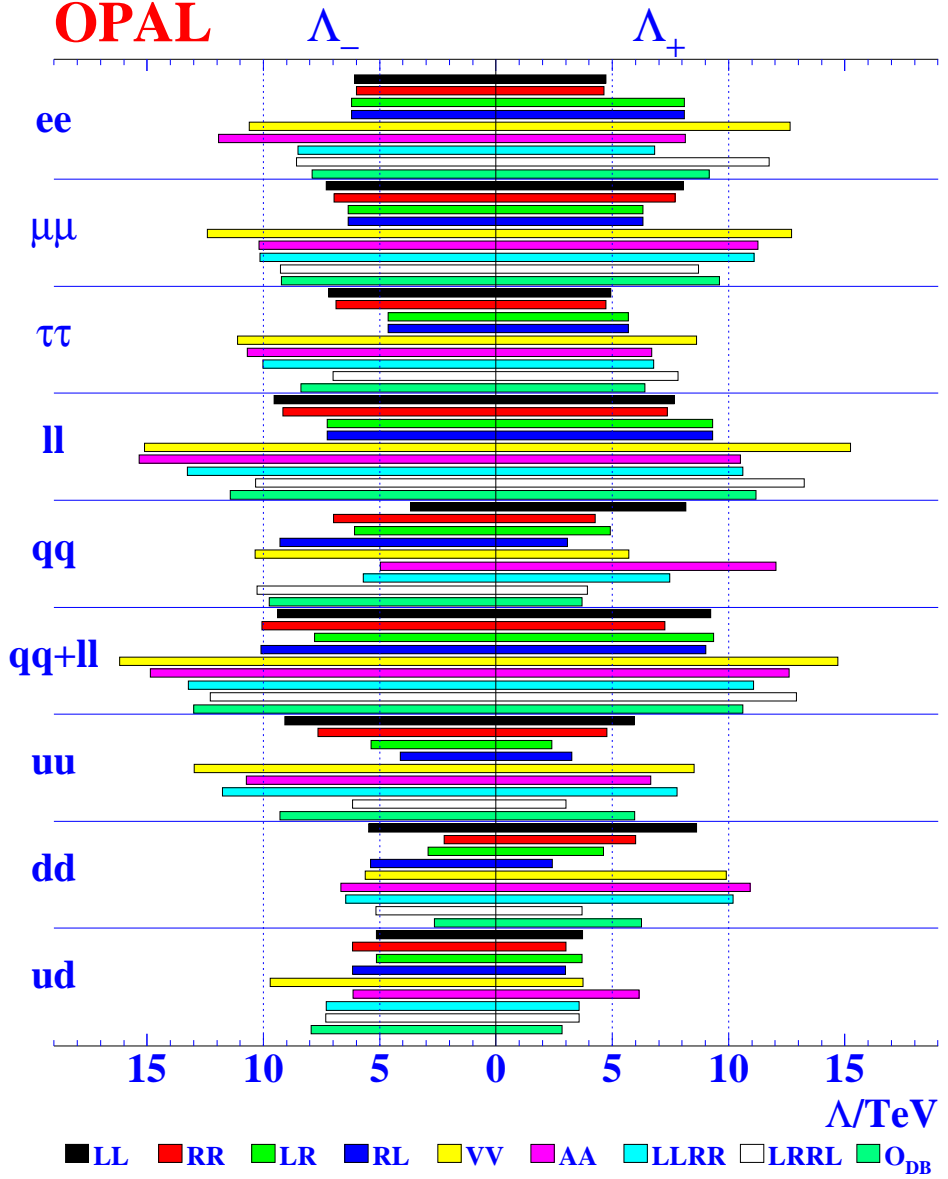


Figure 19: 95% confidence level limits on the energy scale Λ resulting from the contact interaction fits to hadron and lepton-pair data. For each channel, the bars from top to bottom indicate the results for models LL to \overline{O}_{DB} in the order given in the key. The values for Λ_+ and Λ_- correspond to the upper and lower signs, respectively, of the η_{ij} values which define the models as given in Table 21.

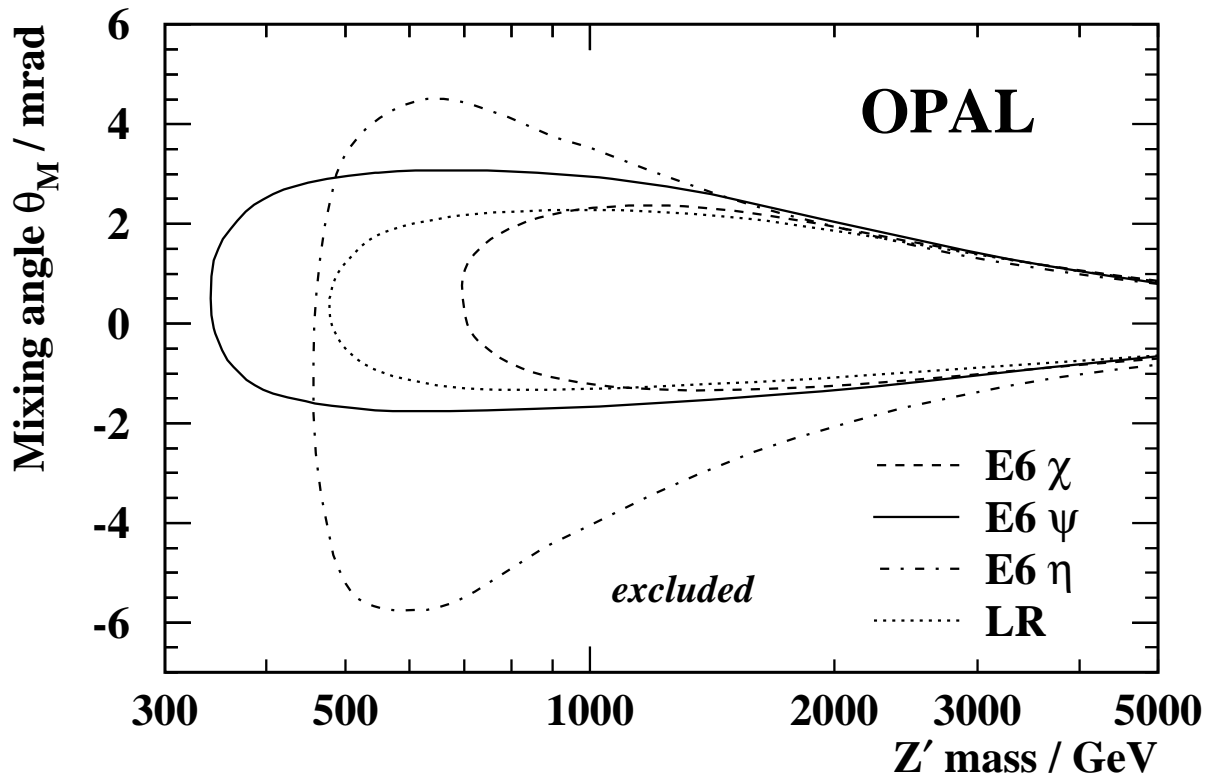


Figure 20: Exclusion contours in the Z' mass – mixing angle plane at 95% confidence level for four Z' models. The Z mass is free during the fit and the other three Standard Model parameters (α_s , m_{top} and m_{Higgs}) are fixed at their default values. Leaving m_{top} and α_s free in the fit would lead to an increase of the width in θ_M by less than 10 %.

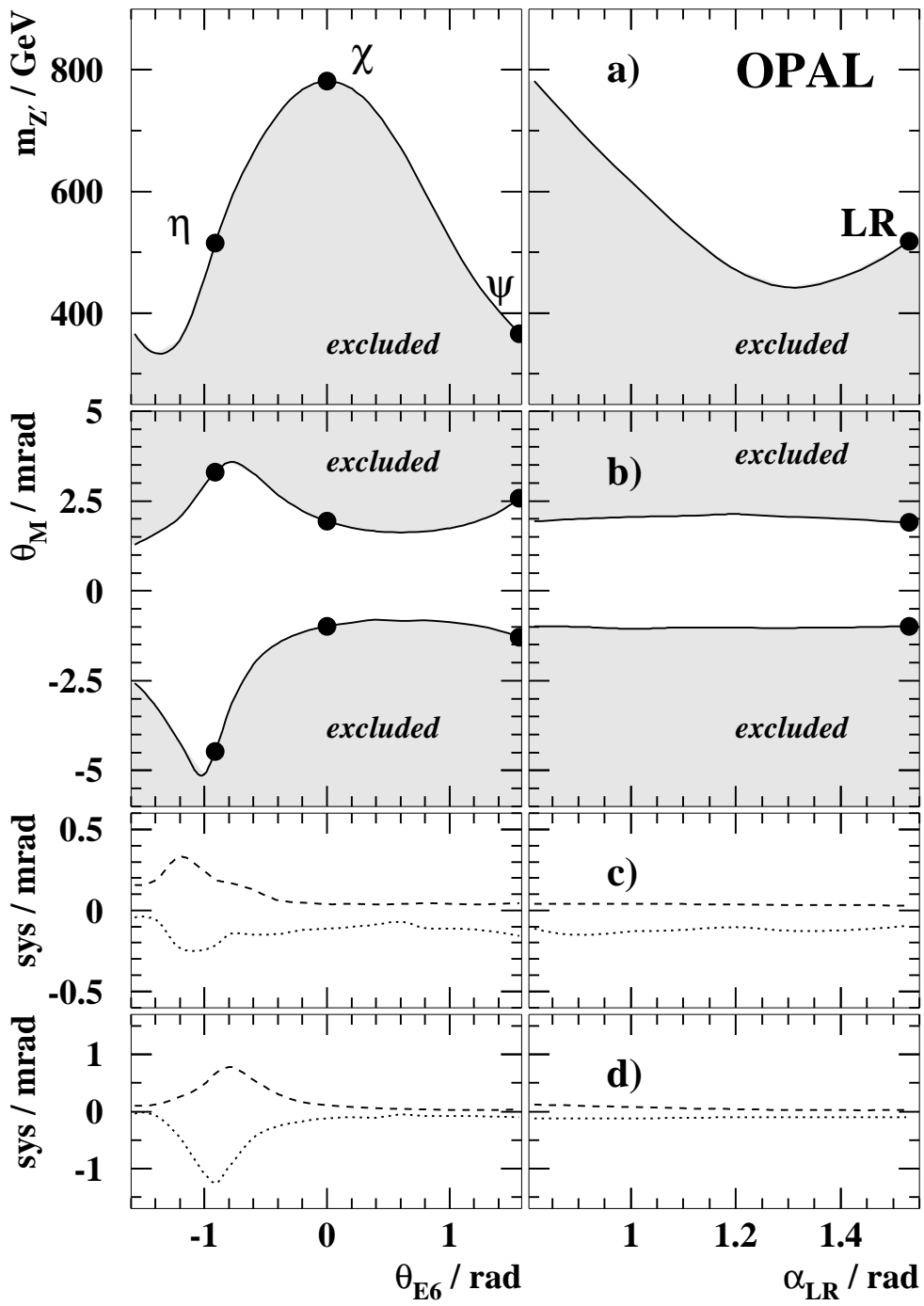


Figure 21: One dimensional limits at 95% confidence level for E6 and LR models as a function of the model angle. The particular cases of the η , χ , ψ and LR symmetric models are indicated by the dots. (a) shows the limits on the Z' mass, and (b) shows the upper and lower limits on the mixing angle. They are obtained from a fit with α_s , m_{top} and m_{Higgs} fixed but m_Z is free. (c) shows the absolute change in the limit on the mixing angle if α_s and m_{top} are free parameters but constrained by their experimental uncertainties. (d) shows the absolute change in the limit on the mixing angle if $m_{\text{Higgs}} = 250 \text{ GeV}$ instead of the default value of 115 GeV. In (c) and (d) the dashed curve denotes the change in the positive limit and the dotted curve denotes the change in the negative limit.

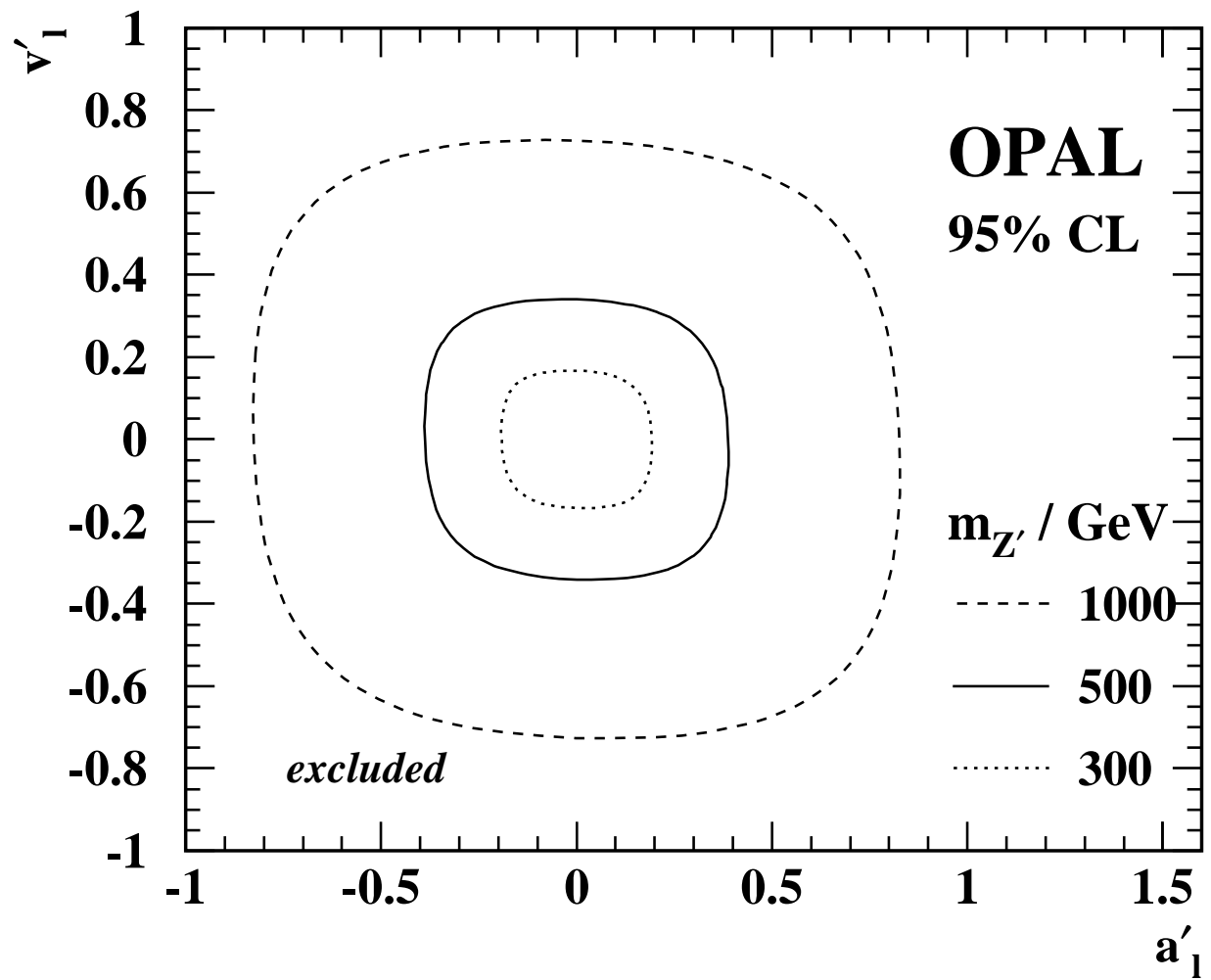


Figure 22: 95% confidence level exclusion contours on the axial and vector couplings of a Z' to leptons, for three values of the Z' mass.